



UNIVERSITÀ DEGLI STUDI DI PADOVA

FACOLTÀ DI SCIENZE MATEMATICHE FISICHE E NATURALI

DIPARTIMENTO DI SCIENZE CHIMICHE

CORSO DI LAUREA MAGISTRALE IN CHIMICA

TESI DI LAUREA

**ELECTRON SPIN ECHO ENVELOPE MODULATION
SPECTROSCOPY OF THE PHOTOPROTECTIVE SITE IN
THE PERIDININ-CHLOROPHYLL-PROTEIN**

RELATORE: DOTT.SSA MARILENA DI VALENTIN

CONTRORELATORE: DOTT. MASSIMO BELLANDA

LAUREANDA: CLAUDIA TAIT

ANNO ACCADEMICO 2010 – 2011

TABLE OF CONTENTS

Abstract

I. INTRODUCTION AND THEORY

Chapter 1	Photosynthesis and Photoprotection	...3
	1.1 Antenna Complexes and Photosynthetic Pigments	...3
	1.2 Energy Transfer in Antenna Complexes	...6
	1.3 Peridinin-Chlorophyll-Protein (PCP)	...8
Chapter 2	EPR Spectroscopy and Triplet States	...13
	2.1 EPR Spectroscopy	...13
	2.2 Spin Hamiltonian	...14
	2.2.1 Electron Zeeman Interaction	...15
	2.2.2 Nuclear Zeeman Interaction	...16
	2.2.3 Hyperfine Interaction (HFI)	...16
	2.2.4 Nuclear Quadrupole Interaction (NQI)	...17
	2.2.5 Zero-Field Splitting	...18
	2.3 EPR Spectroscopy of the Triplet State	...20
	2.3.1 The Triplet State	...20
	2.3.2 The Triplet State in EPR spectroscopy	...21
	2.3.3 Triplet-Triplet Energy Transfer	...25
Chapter 3	Pulse EPR Spectroscopy	...27
	3.1 Semi-Classical Description of Pulse EPR Experiments	...27
	3.2 Echo-Detected Field-Swept EPR	...29
	3.3 ESEEM Spectroscopy	...30
	3.3.1 General Aspects of ESEEM Spectroscopy	...30
	3.3.2 Semi-Classical Description of the ESEEM Experiment	...32
	3.3.3 Two-Pulse ESEEM	...32
	3.3.4 Three-Pulse ESEEM	...33
	3.4 HYSCORE	...34

Chapter 4	Theory of ESEEM	...37
4.1	Quantum Mechanical Description of ESEEM	...37
4.2	ESEEM for a $S=1/2$, $I=1/2$ System	...41
4.2.1	Two-Pulse ESEEM	...43
4.2.2	Three-Pulse ESEEM	...44
4.3	ESEEM for a $S=1/2$, $I=1$ System	...45
4.4	ESEEM for a $S=1$, $I=1/2$ System	...48
4.5	ESEEM for Several Nuclei	...51
4.6	ESEEM in Orientationally Disordered Systems	...51
4.7	HYSCORE	...53
4.7.1	HYSCORE for $S=1/2$, $I=1/2$ and $I=1$ Systems	...53
4.7.2	Correlation Patterns for Disordered Systems	...56

II. EXPERIMENTAL SECTION

Chapter 5	ESEEM Formulae for Triplet State Systems	...61
5.1	Method	...61
5.2	Two- and Three-Pulse ESEEM for $S=1$, $I=1$ Systems	...62
5.3	HYSCORE for Triplet State Systems	...65
5.3.1	HYSCORE for a $S=1$, $I=1/2$ System	...65
5.3.2	HYSCORE for a $S=1$, $I=1$ System	...67
Chapter 6	ESEEM Experiments on the Peridinin Triplet State	...73
6.1	Materials and Methods	...73
6.1.1	Sample Preparation	...73
6.1.2	ESEEM Experiments	...74
6.1.3	Data Analysis	...75
6.2	Results and Discussion	...76
6.2.1	ESEEM Experiments	...76
6.2.1.1	H/D Exchange	...78
6.2.1.2	Two-pulse ESEEM	...78
6.2.1.3	Three-pulse ESEEM	...81
6.2.2	Discussion of the ESEEM data	...84

Chapter 7	Simulation and Interpretation of ESEEM Data	...87
7.1	Methods	...87
7.1.1	Computational Details	...87
7.1.2	Simulation of Echo-detected EPR spectra	...88
7.1.3	Simulation of ESEEM data	...89
7.2	Results	...92
7.2.1	Geometry Optimizations	...92
7.2.1.1	DFT Geometry Optimizations	...92
7.2.1.2	ONIOM Geometry Optimizations	...94
7.2.2	Calculation of Hyperfine Interaction Parameters	...97
7.2.2.1	Spin density	...97
7.2.2.2	Hyperfine Interaction Parameters	...98
7.2.3	ESEEM Simulations	...101
7.2.3.1	Matrix Proton Contributions	...101
7.2.3.2	Exchangeable Protons on the Peridinin Molecule	...104
7.2.3.3	Water Molecule H ₂ O 701	...105
7.3	Discussion	...112
7.3.1	Structure of the Photoprotective Site	...112
7.3.2	Interpretation of ESEEM Results	...114
Chapter 8	HYSCORE Experiments on the Peridinin Triplet State	...121
8.1	Materials and Methods	...122
8.2	Results	...122
8.2.1	Deuterium HYSCORE	...123
8.2.2	Proton HYSCORE	...124
8.3	Discussion	...126
Chapter 9	Conclusions	...129
References		...133
Appendix		...137

ABSTRACT

The present thesis work is part of an extensive study on the energy transfer processes in photosynthetic light-harvesting complexes, in particular of the triplet-triplet energy transfer at the basis of the photoprotection mechanism in these systems.

The light-harvesting complexes of photosynthetic organisms absorb energy from solar radiation and transfer it to the photosynthetic reaction centre, where the light energy is transformed into chemical energy. The presence of excess radiation can lead to photo-oxidative damage by generation of triplet state chlorophyll and subsequently highly oxidant singlet oxygen species. The properties of carotenoid triplet states allow efficient quenching of the triplet state of chlorophyll in what is called the photoprotection mechanism. Photoprotection occurs through triplet-triplet energy transfer from chlorophyll to a carotenoid molecule with a mechanism requiring an overlap of the orbitals of the donor and acceptor molecules and hence imposing a stringent distance- and orientation-dependence. The generated carotenoid triplet state can be detected and characterized by Electron Paramagnetic Resonance (EPR) spectroscopy.

The availability of the X-ray structure of several light-harvesting complexes has allowed the investigation of structure-function relationships with the aid of advanced spectroscopic methodologies. The present work is focused on the Peridinin-Chlorophyll *a*-Protein (PCP), an antenna complex of dinoflagellates containing pigment clusters of one chlorophyll molecule surrounded by four peridinin molecules. Time-resolved EPR experiments have allowed identifying the specific chlorophyll-peridinin pair within this cluster involved in the triplet-triplet energy transfer [1].

Structural requirements for efficient triplet-triplet energy transfer can be deduced from the characteristics of this specific pigment pair. Even though all four peridinin molecules are in Van der Waals contact with the chlorophyll ring, the peridinin molecule responsible for photoprotection in PCP is distinguished by the shortest centre-to-centre distance and more

importantly by the presence of a water molecule, the fifth ligand of the chlorophyll's Mg ion that is placed between the pigments.

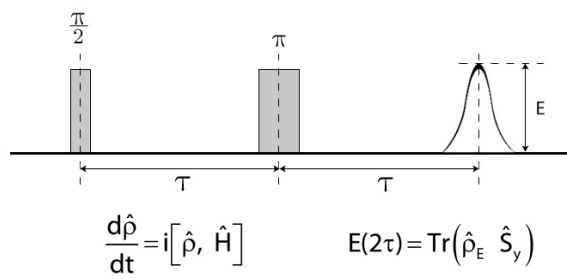
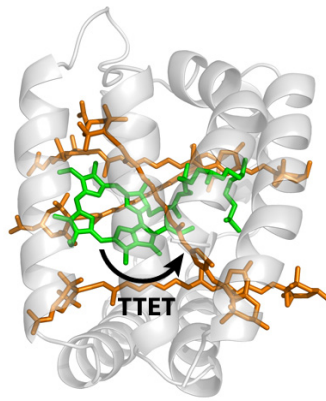
The aim of the present work is to characterize the photoprotection site in PCP and particularly to study the interaction between the interfacial water molecule and the carotenoid triplet state. This is achieved by the pulse EPR technique ESEEM (Electron Spin Echo Envelope Modulation) combined with hydrogen-deuterium exchange aimed at highlighting the exchangeable water protons. The discovery of a strong interaction between the water molecule and the peridinin triplet state will be evidence that this water molecule, next to the chlorophyll and peridinin molecules, is an integral part of the photoprotective system in PCP.

In the past, the ESEEM technique has been only rarely applied to triplet states, hence the ESEEM studies are accompanied by the theoretical derivation of the formulae describing the experimental signal following a density matrix treatment described in the literature. The knowledge of the complete analytical expression for the observed signal is important in aiding the interpretation of the experimental data.

The pulse EPR studies are combined with quantum mechanical calculations in order to identify the exact spatial arrangement and relative orientation of the two pigments and especially of the interfacial water molecule, which is not defined in the X-ray structure. A detailed geometrical and electronic description of the photoprotection site is essential for future studies on the exchange coupling integral determining the energy transfer, which will lead to a better understanding of the requirements for efficient triplet-triplet energy transfer. The water molecule interposed between the pigment pair involved in the triplet-triplet energy transfer in PCP and similar bridging molecules revealed in other antenna complexes have been proposed to increase the energy transfer efficiency by a super-exchange mechanism. Further computational studies based on the results of the present work will shed light on the hypothetical role of the interfacial water molecule as a super-exchange bridge.

I

INTRODUCTION AND THEORY



CHAPTER 1

PHOTOSYNTHESIS AND PHOTOPROTECTION

Photosynthesis is the process upon which all life on earth depends. Photosynthesis occurs in photoautotroph organisms, such as algae, higher plants and some species of bacteria, and is based on the conversion of solar energy into chemical energy.

The photosynthetic organisms harvest the sunlight with pigments contained in protein complexes. The energy is then funnelled to the photosynthetic reaction centre, where the excitation energy is efficiently converted into a charge separation. The charge separation event produces a high energy electron, which is then transferred into an electron transport chain. The final effect is the generation of a trans-membrane electrochemical potential, which is used for the production of adenosine triphosphate (ATP), the reduction of NADP⁺ to NADPH (nicotinamide adenine dinucleotide phosphate) and the oxidation of water to oxygen [2]. Eukaryotic photosynthesis takes place in the thylakoid membranes of chloroplasts, where the protein complexes involved in energy capture, electron transfer and ATP synthesis are embedded.

1.1 ANTENNA COMPLEXES AND PHOTOSYNTHETIC PIGMENTS

Light-harvesting complexes (LHCs) are pigment-protein complexes with the function of light absorption and excitation energy transfer to the photosynthetic reaction centres. The presence of these accessory antenna complexes, next to the inner antennae of the reaction centre in the photosystems, increases the absorption cross section and thus enhances the efficiency of light-harvesting.

There are three main types of photosynthetic pigments contained in light-harvesting complexes: chlorophylls (cyclic tetrapyrroles), carotenoids and peptide-linked phycobilins (linear tetrapyrroles).

Chlorophylls are pigments consisting of a planar porphyrin-type ring with a chelated Mg ion and an attached phytol chain (Fig. 1.1). Several types of chlorophylls exist, differing by the substituents on the porphyrin ring. The electronic structure and spectroscopic properties of chlorophylls are determined by the extended conjugated system of the porphyrin ring. The optical spectra of chlorophylls show the same features common to all porphyrins: two Q bands in the red-near infrared region of the visible spectrum and two B or Soret bands in the blue-violet region (Fig. 1.1). The phytol chain of chlorophylls often has an important structural function, determining the arrangement of the molecule in a protein environment. The chlorophylls are the main light-harvesting pigments in most antenna complexes; their function is essentially the absorption of light and the transfer of excitation energy towards the photosynthetic reaction centre.

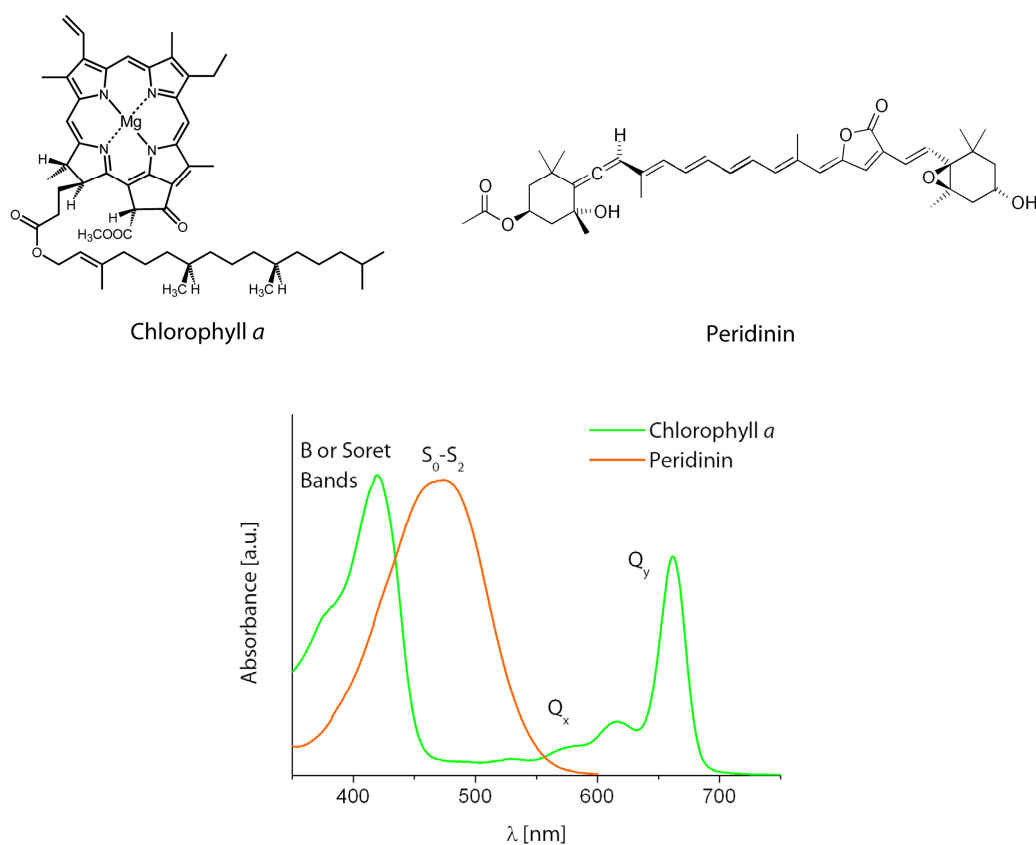


Fig. 1.1 Structures of chlorophyll *a* and peridinin, the main carotenoid in antenna complexes of dinoflagellates, and corresponding visible absorption spectra of the pigments dissolved in ethanol.

Carotenoids are the most widely occurring pigments in nature; they are characterized by a linear polyene chain that accounts for their spectroscopic properties (Fig. 1.1). Many carotenoids with different numbers of conjugated double bonds and with various substitutions in the polyene chain and in the polar head groups exist. The absorption spectra of all carotenoids feature a

major band in the blue-green region of the visible spectrum due to the transition from the ground state S_0 to the second excited singlet state S_2 , as depicted in Fig.1.1 for the carotenoid peridinin. The transition to the first excited state S_1 is forbidden due to symmetry considerations. The principal factor in determining the energy of the excited states of a specific carotenoid is the number of conjugated double bonds; the protein environment can also cause a shift of the energy levels.

The carotenoids in antenna complexes fulfil several important functions. Firstly, they protect against photo-oxidative damage by quenching triplet state chlorophyll and singlet oxygen. This can be regarded as their main function, as it has been shown that carotenoidless mutants of photosynthetic purple bacteria suffer photo-oxidative death if exposed to light and oxygen [2]. Secondly, they act as accessory light-harvesting pigments by extending the spectral range for absorption to the blue-green and yellow regions of the solar emission spectrum not accessible to chlorophyll and thereby increasing the light-harvesting efficiency. This function is essential for organisms in environments where light available for the absorption by chlorophyll is low, such as for marine organisms living in depths where the sunlight in the red and to a lesser extent in the blue spectral regions has been filtered out by the surrounding water layers. Due to the substantial spectral gradient through the leaf cross section, this function of the carotenoids is important in higher plants as well. Thirdly, the carotenoids in higher plants have been shown to be responsible for the non-radiative dissipation of energy that protects against photo-inhibition in conditions of excessive light. Their function is to divert the energy from the reaction centre in order to avoid over-reduction of the photosystem [2]. Finally, carotenoids are thought to assume also a structural stabilization role. The detailed mechanism for this stabilization role is as yet not completely clear, but it has been proposed to be due to π - π stacking interactions with other pigments and amino acid residues of the protein [3].

The photosynthetic pigments are generally non-covalently bound to the protein component of the light-harvesting complexes. The spatial arrangement of the pigment molecules is thus imposed by the protein environment. It further determines the configuration and conformation of the pigments and thereby establishes their spectroscopic properties. The protein component of the light-harvesting systems also mediates the interaction with other protein components in the complex structural organization of the supramolecular antenna systems, allowing excitation energy transfer between different antenna complexes and to the reaction centre of the photosystem. Since the efficiency of the energy transfer between the photosynthetic pigments in the same or in different antenna complexes is highly sensitive to their relative geometric arrangement, the protein structure of light-harvesting complexes plays a fundamental role in the establishment of energy transfer pathways inside the photosynthetic apparatus.

1.2 ENERGY TRANSFER IN ANTENNA COMPLEXES

The carotenoids in antenna complexes perform their role as accessory light-harvesting pigments by absorption of sunlight and by excitation energy transfer to nearby chlorophyll molecules in the complex. The S_1 and S_2 energy levels of carotenoids in photosynthetic proteins are energetically higher and close respectively to the first (Q_Y) and second (Q_X) excited singlet state of chlorophyll and thus excitation energy transfer can occur. After excitation of the carotenoid, the singlet-singlet energy transfer to chlorophyll may proceed through two different pathways, either directly to the Q_X level of chlorophyll or, following internal conversion to the low-lying S_1 state, to the Q_Y level of chlorophyll. The energy levels of the pigments and the two energy transfer pathways are depicted in Fig. 1.2.

The singlet excitation transfer may occur with the Förster mechanism [4] based on the long-range Coulomb interaction between the transition dipole moments of the two pigments or with the Dexter mechanism [5] based on the electron-exchange interaction.

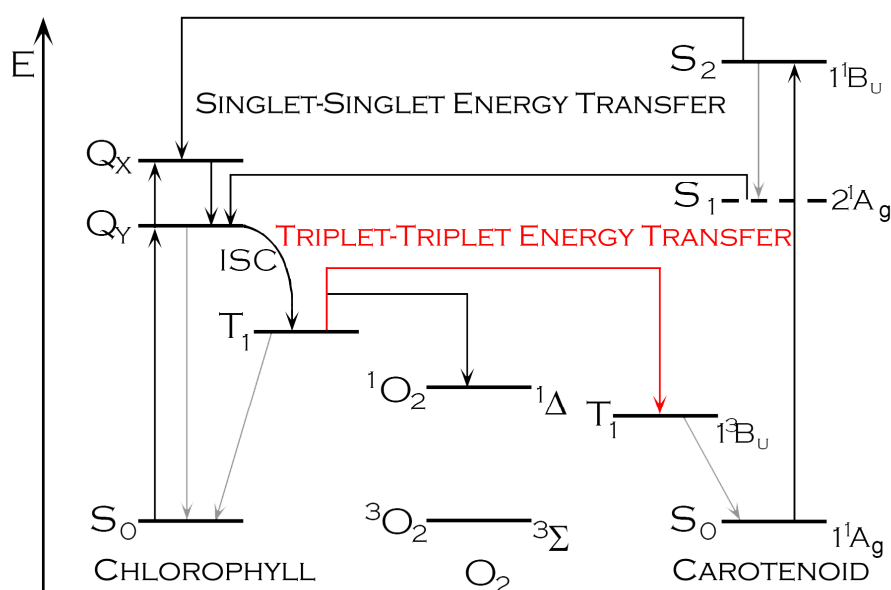
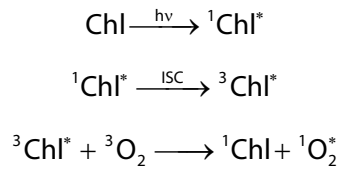


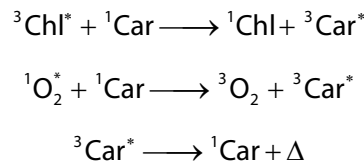
Fig. 1.2 Schematic diagram of the energy levels of a chlorophyll-carotenoid-oxygen system and possible energy transfer pathways.

The excited singlet state of chlorophyll populated either by direct absorption or by singlet-singlet energy transfer from a carotenoid molecule, has a finite probability of evolving to an excited triplet state by Intersystem Crossing (ISC). The relatively long-lived chlorophyll triplet state can react with triplet oxygen to form singlet oxygen. Singlet oxygen is a highly oxidative species that combines rapidly with dienes causing the photo-oxidative death of the photosynthetic organism.

The reactions involved in the process of singlet oxygen formation are:



The triplet state of carotenoids with nine or more conjugated double bonds, as are usually encountered in antenna complexes, lies at a lower energy than the triplet state of chlorophyll. Hence these carotenoids can act as photoprotective agents by quenching the chlorophyll triplet state. Carotenoids of this type can provide further protection against photo-oxidation by directly quenching singlet oxygen, since their triplet state lies also energetically below the ${}^1\text{O}_2^*$ state. The carotenoid triplet state then decays to the ground state by non-radiative processes. The photoprotective action of carotenoids can be described by the following reactions:



The photo-physical mechanism for triplet chlorophyll quenching by carotenoids is the Dexter electron-exchange mechanism [5]. The electron-exchange mechanism can be viewed as a simultaneous double-electron exchange between the HOMO (Highest Occupied Molecular Orbital) of the donor and the LUMO (Lowest Unoccupied Molecular Orbital) of the acceptor and between the HOMO of the acceptor and the LUMO of the donor [6], as represented in Fig. 1.3.

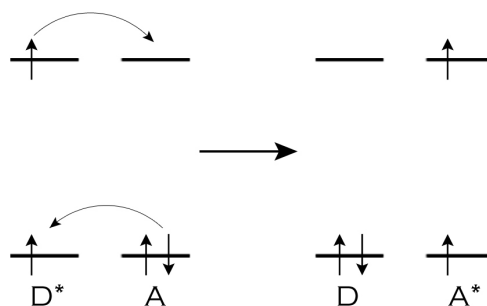


Fig. 1.3 Frontier orbital representation of electron exchange in the triplet-triplet energy transfer by the Dexter mechanism.

The Dexter mechanism requires overlap of the orbitals of the donor and acceptor molecule and therefore poses stringent constraints on the distance between the pigments involved in the photoprotection process.

1.3 PERIDININ - CHLOROPHYLL- PROTEIN (PCP)

Peridinin-Chlorophyll *a*-Protein (PCP) is the peripheral water-soluble light-harvesting complex of most photosynthetic dinoflagellates. Dinoflagellates constitute the main part of oceanic plankton and are the cause of red tides. The PCP complex of the dinoflagellate *Amphidinium carterae* has been the object of extensive spectroscopic studies with the aim to understand the inner workings of the energy transfer processes in antenna complexes, especially after the elucidation of the X-ray structure by Hofmann *et al.* [7].

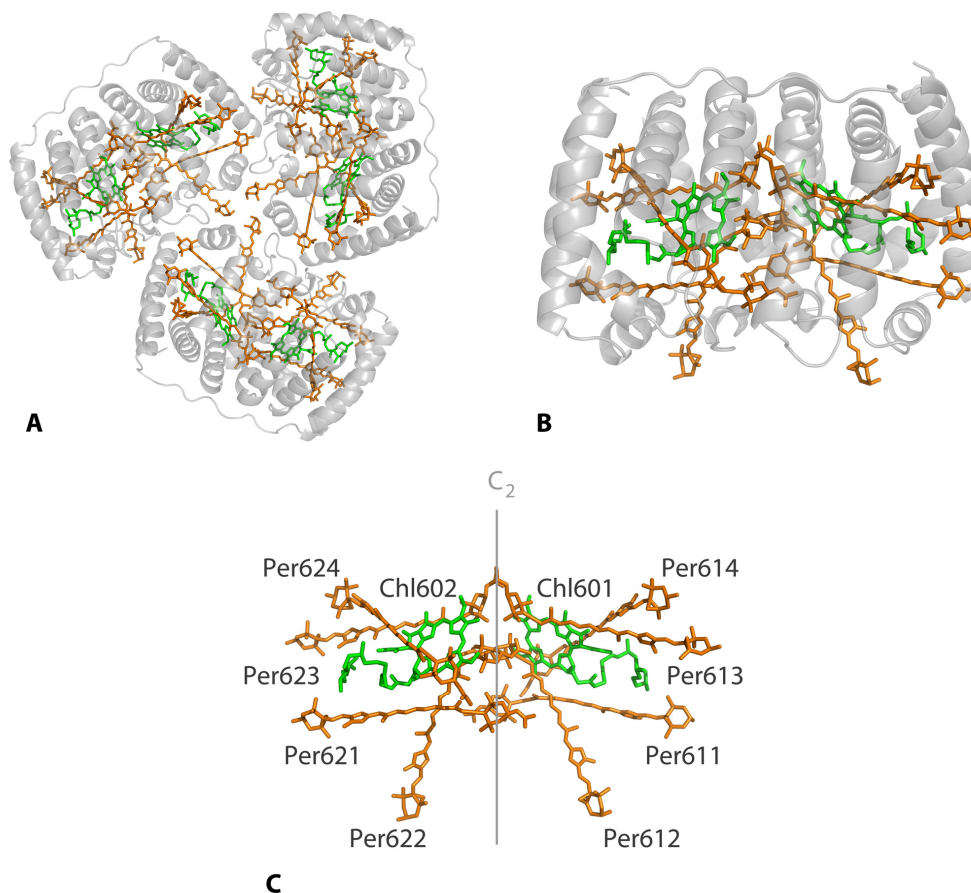


Fig. 1.4 Structure of the PCP trimer (A), the monomer (B) and of the pigments contained in one monomer (C). The pseudo-C₂ axis is shown. The structures are based on the X-ray data from the protein data bank file 1PPR.

The 2.0 Å X-ray structure revealed the presence of a non-crystallographic trimer of identical 32 kD subunits, each of which is constituted by a polypeptide forming a hydrophobic cavity filled by the pigment molecules (Fig. 1.4). The NH₂- and COOH-terminal domains of the monomer are characterized by a 56% sequence homology; each domain forms eight α-helices which bind a cluster of one chlorophyll *a* and four peridinin molecules. The two domains are related by a pseudo-twofold symmetry axis, as depicted in Fig. 1.4 C and therefore the two pigment clusters

can be considered equivalent.

The peridinin-chlorophyll *a*-protein is unique on account of the preponderance of carotenoid molecules, while in other light-harvesting complexes the chlorophyll molecules predominate. The carotenoid in PCP is peridinin, whose structure is represented in Fig. 1.1. The key structural features of this highly substituted carotenoid are a lactone and an allene group conjugated to the polyene chain, which confer special spectroscopic properties [8]. The 4:1 ratio of peridinins to chlorophyll in PCP can be explained by the necessity for efficient absorption of light in the blue-green region, which prevails in the marine habitat of dinoflagellates.

The chlorophyll molecule within each pigment cluster is arranged between two pairs of mutually orthogonal peridinins (Per611-Per612 and Per613-Per614 in the NH₂-terminal domain). Chlorophyll molecules in protein complexes are usually non-covalently bound to the protein by coordination of the central Mg ion to an amino acid, either directly or through an intermediary water molecule. The structure of PCP reveals two highly conserved histidine residues (His66 and His229 according to the X-ray nomenclature), which are hydrogen-bonded to a water molecule acting as the fifth ligand of the chlorophyll's Mg ion (Fig. 1.5).

The conjugated regions of all peridinins are in Van der Waals contact (Table 1.1) with the tetrapyrrole ring of chlorophyll, allowing efficient excitonic energy transfer from each peridinin to chlorophyll. The distance between the centres of the two chlorophylls in one monomer is 17.4 Å, whereas the distance between two chlorophylls belonging to different monomers ranges from 40 to 54 Å.

Table 1.1

Relevant chlorophyll-peridinin distances in PCP

	π - π shortest distance (Å)	centre-to-centre distance (Å)
Chl-Per611/621	4.38/4.50	8.57/8.57
Chl-Per612/622	4.24/3.70	8.97/8.97
Chl-Per613/623	4.24/4.14	9.36/9.49
Chl-Per614/624	5.00/4.71	5.44/5.36

The table reports the significant distances between the peridinin and the chlorophyll molecules obtained from the coordinates of the native PCP complex (PDB entry 1PPR).

In addition to the PCP protein complex isolated from *Amphidinium carterae*, PCP complexes from other species of marine algae and variants of the PCP complex have also been investigated [9]. All these PCP complexes are characterized by the same minimal building block, an α -helical protein

domain containing a pigment cluster, but exhibit different oligomeric arrangements. They share a moderate to high protein sequence similarity and provide highly homologous binding sites for the pigments. After the development of a refolding system, complexes with modified pigment compositions were produced and their X-ray structures were determined, specifically the chlorophyll *a* molecules of the native antenna complex were substituted by chlorophyll *b*, chlorophyll *d* and bacteriochlorophyll *a* [10]. The pigment arrangement in all these reconstituted protein complexes is almost identical, proving the influence of the protein matrix in determining the conformation and the relative orientation of the photosynthetic pigments.

The singlet-singlet energy transfers in the PCP complexes have been extensively studied by optical spectroscopy and the results are reviewed in reference [8]. It has been shown that the peridinin to chlorophyll excitation energy transfer takes place with ~90% efficiency. The study of the various PCP complexes mentioned above has led to the conclusion that the energy transfer pathways and their efficiencies are finely tuned both by the protein structure, ensuring a proper orientation of the donor and acceptor molecules, and by the polarity and hydrogen bonding capability of the protein environment, controlling the spectral properties of the pigments.

The triplet-triplet energy transfer (TTET) in PCP has been studied both by optical [11,12] and magnetic spectroscopies [1,13-15]. The photoprotection through quenching of the chlorophyll's triplet state by peridinin in the PCP antenna complex is characterized by a ~100% efficiency [11].

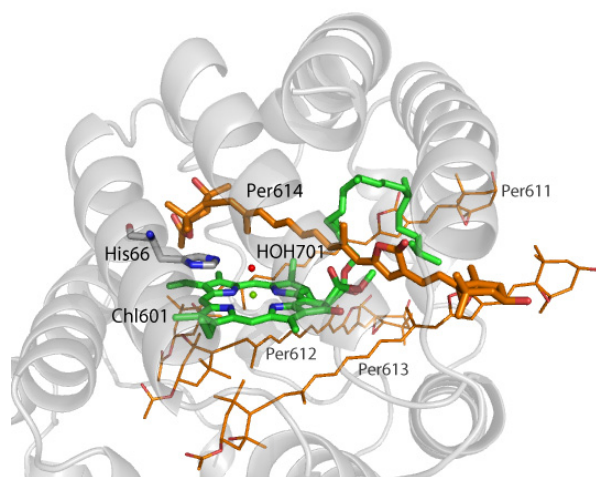


Fig. 1.5 Pigment cluster of the NH₂-terminal domain of PCP with X-ray nomenclature (PDB file 1PPR). The water molecule coordinated to chlorophyll and the hydrogen-bonded histidine residue are highlighted.

Time-resolved Electron Paramagnetic Resonance (EPR) experiments have been exploited in conjunction with spectral simulations based on the theory of TTET in order to identify the specific path for triplet quenching [1]. It has been shown that the pigment pairs Chl601-Per614 and Chl602-Per624 are responsible for photoprotection in the PCP antenna complex. The conclusion

that the triplet state generated by TTET is localized on a single peridinin molecule is further supported by results of ENDOR (Electron Nuclear DOuble Resonance) experiments [13,15]. The identified peridinin molecule is distinguished by a smaller centre-to-centre distance to chlorophyll with respect to the other peridinin molecules of the pigment cluster, however all four peridinin molecules are at Van der Waals distance from the chlorophyll ring (Table 1.1). The unique feature of this chlorophyll-peridinin pair is the presence of a water molecule interposed between the two pigments (Fig. 1.5).

CHAPTER 2

EPR SPECTROSCOPY AND TRIPLET STATES

Electron Paramagnetic Resonance (EPR) or Electron Spin Resonance (ESR) spectroscopy is concerned with the study of the interactions between the magnetic moments of electron spins and an external magnetic field. EPR techniques can be employed in the study of the structure, the dynamics and the spatial distribution of paramagnetic species. EPR can only be applied to paramagnetic systems, i.e. systems with unpaired electron spins such as radicals, triplet states, transition metal complexes, defects in solids, etc.

2.1 EPR SPECTROSCOPY

EPR spectroscopy is applied to paramagnetic species characterized by a spin quantum number $S \neq 0$. The external magnetic field applied during the EPR experiment lifts the degeneracy of the states characterized by different values of the spin magnetic quantum number m_s due to the electron Zeeman interaction (Fig. 2.1). Monochromatic continuous microwave radiation then induces electron spin transitions between these states and a signal is observed.

The steady-state continuous wave EPR (cw-EPR) experiment consists in the measurement of the absorption of microwave radiation by the sample during a slow sweep of the external magnetic field B_0 . A signal is observed if the resonance conditions are fulfilled (Fig. 2.1), the selection rule for EPR spectroscopy is $\Delta m_s = \pm 1$.

In order to apply EPR spectroscopy to meta-stable species, such as photo-induced triplet states, a variant called time-resolved EPR (TR-EPR) has been developed. In photo-excited TR-EPR the irradiation of the sample with a laser pulse prior to the actual cw-EPR experiment produces the paramagnetic species. The time evolution of the EPR signal after the laser pulse is measured at

fixed magnetic field values and by collecting time traces for different field values, a two-dimensional spectrum, reporting the signal intensity as function both of the external magnetic field and the time after the laser pulse, is obtained. The TR-EPR technique allows the detection of the EPR signal of photo-excited species and the study of their evolution in time.

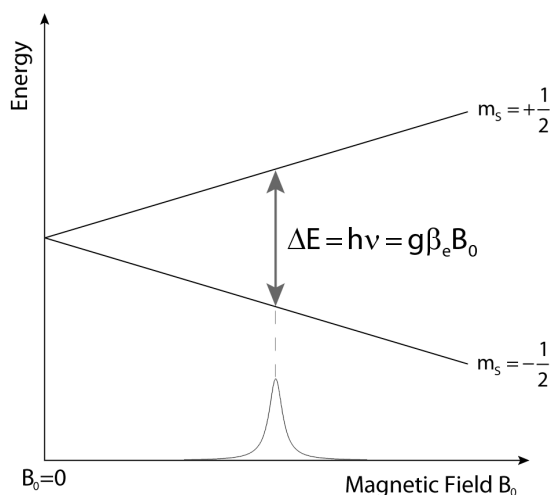


Fig. 2.1 Illustration of the generation of an EPR signal in resonance conditions for a $S = \frac{1}{2}$ system.

In addition to cw-EPR, several pulse EPR experiments have been developed. In pulse EPR spectroscopy the constant microwave radiation is replaced with sequences of short microwave pulses. Pulse EPR allows the design of experiments aimed at determining information on the spin system not accessible by traditional cw-EPR. The characteristics of pulse EPR are described in the following chapter. In the study of photo-excited systems the pulse experiment is preceded by a laser pulse generating the desired species, in an analogous manner to TR-EPR.

2.2 SPIN HAMILTONIAN

The position and the shape of the EPR signal are determined by various interactions in the paramagnetic spin system. A system of electrons and nuclei in a magnetic field is characterized by the interactions of the magnetic moments with the external magnetic field and by their mutual interactions. These interactions can be expressed just in terms of the electron and nuclear spin angular momentum operators and of phenomenological parameters; hence the Hamiltonian describing the system is referred to as spin Hamiltonian. The contributions of the orbital angular moments are approximated and absorbed in the magnetic parameters, which are expressed as tensors. The advantage of a Hamiltonian containing only spin operators and no spatial operators is that the EPR experiments can be described by considering just the spin part of the electronic wavefunction, thus greatly simplifying the theoretical treatment.

In general the spin Hamiltonian can be composed of the following terms:

$$\hat{H}_0 = \hat{H}_{EZ} + \hat{H}_{ZFS} + \hat{H}_{NZ} + \hat{H}_{HFI} + \hat{H}_{NQL} + \hat{H}_{NN}$$

with

$$\hat{H}_{EZ} = \text{electron Zeeman interaction}$$

$$\hat{H}_{ZFS} = \text{zero – field splitting}$$

$$\hat{H}_{NZ} = \text{nuclear Zeeman interaction}$$

$$\hat{H}_{HFI} = \text{hyperfine interaction between electron and nuclear spins}$$

$$\hat{H}_{NQL} = \text{nuclear quadrupole interaction for nuclear spins with } I > \frac{1}{2}$$

$$\hat{H}_{NN} = \text{spin – spin interactions between nuclear spins}$$

In the following the spin Hamiltonian will be expressed in angular frequency units.

Each type of interaction can be described by a second-rank tensor, which is diagonal in an appropriate coordinate system. In this principal axis system the interaction is completely characterized by the three principal components. In general the principal axis systems of the tensor relative to different types of interaction do not coincide.

2.2.1 ELECTRON ZEEMAN INTERACTION

The electron Zeeman interaction describes the interaction between the electron spin and an external magnetic field, the corresponding Hamiltonian is:

$$\hat{H}_{EZ} = \frac{\beta_e B_0 g \hat{S}}{\hbar}$$

where β_e represents the Bohr magneton, B_0 is the static magnetic field vector, g is the g tensor and \hat{S} is the electron spin operator. If contributions of the orbital angular momentum to the interaction with the magnetic field and spin-orbit interactions are absent, g is a scalar and assumes the free electron spin g_e value of 2.0023193043617 [16]. The g -factor is introduced to take into account the quantistic behaviour of the spin angular momentum. In order to define a Hamiltonian depending only on the spin operators, the contributions of the spatial operators are approximated by perturbation theory and included in the g factor, which thus becomes a tensor with values determined by the specific system under investigation.

2.2.2 NUCLEAR ZEEMAN INTERACTION

The nuclear Zeeman interaction describes the interaction between the nuclear spin and the external magnetic field and is expressed by the Hamiltonian:

$$\hat{H}_{\text{NZ}} = -\frac{g_n \beta_n B_0 \hat{I}}{\hbar}$$

where β_n represents the nuclear Bohr magneton, B_0 is the static magnetic field vector and \hat{I} is the nuclear spin operator. The term $g_n \beta_n B_0 \hbar^{-1}$ stands for the nuclear Larmor frequency, the precession frequency of the nuclear spin around the applied magnetic field, and is often written as ω_I .

The spin quantum number I and the nuclear g_n factor are inherent properties of a nucleus. Due to the dependence on the inverse of the mass of the electron and the nucleus, the Bohr magneton is three orders of magnitude greater than the nuclear Bohr magneton. Consequently, the electron Zeeman interaction is larger than the nuclear Zeeman interaction.

2.2.3 HYPERFINE INTERACTION (HFI)

The hyperfine interaction describes the interaction between the magnetic moment of the electron spin and that of the nuclear spins in the paramagnetic sample. In the spin Hamiltonian this interaction is expressed as:

$$\hat{H}_{\text{HFI}} = \hat{S} A \hat{I}$$

where \hat{S} and \hat{I} are the electron and nuclear spin angular moments and A is the hyperfine tensor. The hyperfine tensor is the sum of the isotropic or Fermi contact interaction (a_{iso}) and the anisotropic electron-nuclear dipole-dipole interaction (T):

$$A = a_{\text{iso}} \mathbf{1} + T$$

The Fermi contact interaction arises due to the finite spin density at the nucleus and the corresponding isotropic hyperfine coupling constant is defined as:

$$a_{\text{iso}} = \frac{2}{3} \frac{\mu_0}{\hbar} g_e \beta_e g_n \beta_n |\psi_0(0)|^2$$

where $|\psi_0(0)|^2$ represents the electron spin density at the position of the nucleus.

The anisotropic dipole-dipole interaction is described by substituting the spin operators in the classical expression for the dipole-dipole interaction between two magnetic moments. Since the

electron spin is delocalized, an average over the spatial electron distribution is performed, yielding the dipolar coupling tensor T . T is a symmetric, traceless tensor with elements defined as:

$$T_{ij} = \frac{\mu_0}{4\pi\hbar} g_e \beta_e g_n \beta_n \left\langle \Psi_0 \left| \frac{3 r_i r_j - \delta_{ij} r^2}{r^5} \right| \Psi_0 \right\rangle$$

where r is the distance between the electron and the nuclear spin and Ψ_0 is a molecular orbital expressed as linear combination of atomic orbitals. One- and two-centre contributions can be distinguished, the former arising from the interaction of the electron spin in the atomic orbital of a nucleus N with the nucleus itself and the latter from the interaction of the electron spin in an atomic orbital centred at another nucleus with the nucleus N . In the case of protons the one-centre contribution is absent, as the unpaired electron is in an s orbital.

For distances between a nucleus N and the centre of the k^{th} atomic orbital $R_k \geq 0.25 \text{ nm}$, the point-dipole approximation can be applied. The unpaired electron density is then considered to be concentrated at the nucleus k , and the hyperfine tensor relative to the interaction with the nucleus N can be approximated by:

$$T = \frac{\mu_0}{4\pi\hbar} g_e \beta_e g_n \beta_n \sum_{k \neq N} \rho_k \frac{3 n_k \tilde{n}_k - 1}{R_k^3}$$

where ρ_k is the spin density on the k^{th} atomic orbital and n_k is the unit vector denoting the direction cosines of the electron-nucleus vector in the molecular frame.

The hyperfine interaction can cause a splitting of the EPR line, referred to as hyperfine structure. In many cases the hyperfine structure is unresolved in cw-EPR spectra and advanced EPR techniques have to be employed to study this type of interaction. The hyperfine coupling parameters are generally determined by double resonance techniques, such as ENDOR (Electron Nuclear DOuble Resonance), or pulsed ESEEM (Electron Spin Echo Envelope Modulation) spectroscopy.

2.2.4 NUCLEAR QUADRUPOLE INTERACTION (NQI)

The non-spherical charge distribution in nuclei with spin $I \geq 1$ gives rise to a nuclear electrical quadrupole moment Q . The interaction of this electrical quadrupole moment with the electric field gradient is described by the nuclear quadrupole interaction Hamiltonian:

$$\hat{H}_{\text{NQI}} = \hat{I} P \hat{I}$$

where P is the nuclear quadrupole tensor. The Hamiltonian written in the principal axis system of

the traceless tensor P is:

$$\hat{H}_{\text{NQ}} = P_x \hat{I}_x^2 + P_y \hat{I}_y^2 + P_z \hat{I}_z^2 = \frac{e^2 q Q}{4I(2I-1)\hbar} \left[\left(3\hat{I}_z^2 - I(I+1)^2 \right) + \eta \left(\hat{I}_x^2 - \hat{I}_y^2 \right) \right] \quad \text{with} \quad \eta = \frac{P_x - P_y}{P_z}$$

where eq is the electric field gradient and η is the asymmetry parameter. The nuclear quadrupole interaction is generally referred to by specifying the values of $e^2 q Q \hbar^{-1}$ and η depending on the particular nucleus in consideration and its environment.

2.2.5 ZERO-FIELD SPLITTING

Spin systems with $S > \frac{1}{2}$ are characterized by $(2S+1)$ energy levels, whose degeneracy can be lifted even in the absence of an external magnetic field due to the dipolar interaction between the electron spins. This interaction is referred to as Zero-Field Splitting (ZFS) and is described by the spin Hamiltonian:

$$\hat{H}_{\text{ZFS}} = \hat{S} D \hat{S}$$

where D is the symmetric and traceless zero-field interaction tensor.

The dipole-dipole interaction between two electron spins can be expressed as:

$$\hat{H}_{\text{DD}}(r) = \frac{\mu_0}{4\pi\hbar} g_1 g_2 \beta_e^2 \left[\frac{\hat{S}_1 \cdot \hat{S}_2}{r^3} - \frac{3(\hat{S}_1 \cdot r)(\hat{S}_2 \cdot r)}{r^5} \right]$$

where g_1 and g_2 are the g-factors for the two electron spins, which can be considered equal to the free electron g value, and r is the vector connecting the electron spins. The scalar products in this expression can be expanded and rewritten in terms of the total spin angular momentum \hat{S} , defined as the sum of the spin angular moments of the two electrons \hat{S}_1 and \hat{S}_2 . Since the electron spins are delocalized, an integration over their spatial distribution has to be performed. By writing the expression in matrix form, the explicit form of the zero-field interaction tensor D is obtained:

$$\hat{H}_{\text{ZFS}} = \frac{\mu_0}{8\pi\hbar} g_e^2 \beta_e^2 \begin{bmatrix} \hat{S}_x & \hat{S}_y & \hat{S}_z \end{bmatrix} \begin{bmatrix} \left\langle \frac{r^2 - 3x^2}{r^5} \right\rangle & \left\langle \frac{-3xy}{r^5} \right\rangle & \left\langle \frac{-3xz}{r^5} \right\rangle \\ \left\langle \frac{-3xy}{r^5} \right\rangle & \left\langle \frac{r^2 - 3y^2}{r^5} \right\rangle & \left\langle \frac{-3yz}{r^5} \right\rangle \\ \left\langle \frac{-3xz}{r^5} \right\rangle & \left\langle \frac{-3yz}{r^5} \right\rangle & \left\langle \frac{r^2 - 3z^2}{r^5} \right\rangle \end{bmatrix} \begin{bmatrix} \hat{S}_x \\ \hat{S}_y \\ \hat{S}_z \end{bmatrix}$$

In the principal axis system of the ZFS-tensor the spin Hamiltonian becomes:

$$\hat{H}_{\text{ZFS}} = D_x S_x^2 + D_y S_y^2 + D_z S_z^2$$

Since the D tensor is traceless, its diagonal elements can be expressed in terms of two independent parameters, the ZFS parameters D and E , defined as:

$$D = \frac{3}{2} D_z = 3 \frac{\mu_0 g_e^2 \beta_e^2}{16\pi\hbar} \left\langle \frac{r^2 - 3z^2}{r^5} \right\rangle$$

$$E = \frac{1}{2} (D_x - D_y) = 3 \frac{\mu_0 g_e^2 \beta_e^2}{16\pi\hbar} \left\langle \frac{x^2 - y^2}{r^5} \right\rangle$$

The spin Hamiltonian in terms of these ZFS parameters is:

$$\hat{H}_{\text{ZFS}} = D \left[S_z^2 - \frac{1}{3} S(S+1) \right] + E (S_x^2 - S_y^2)$$

The principal axes of the ZFS tensor are chosen in order to satisfy the condition $|D| > |3E|$, accordingly $|D_z| > |D_x|, |D_y|$.

The direction of the ZFS axes with respect to the molecular structure depends on the spin density distribution of the system. In general, for oblate spin distributions D is positive and the ZFS axis Z is directed perpendicular to the molecular plane, while for prolate spin distributions D is negative and Z is directed along the principal symmetry axis. For example, for chlorophyll the ZFS Z axis is perpendicular to the plane of the porphyrin ring, while for the carotenoid peridinin contained in PCP, the Z axis is directed along the conjugated chain (Fig. 2.2).

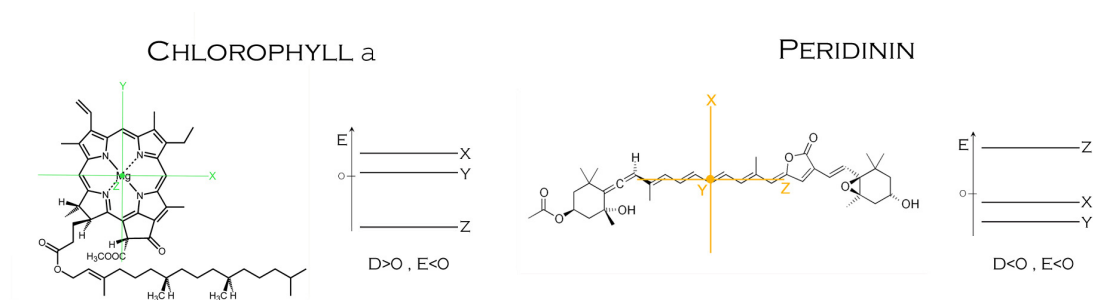


Fig. 2.2 ZFS axes and ordering of the ZFS energy levels for the pigments occurring in the PCP antenna complex ($X = -D_x$, $Y = -D_y$, $Z = -D_z$).

2.3 EPR SPECTROSCOPY OF THE TRIPLET STATE

2.3.1 THE TRIPLET STATE

The triplet state is characterized by a total spin quantum number $S=1$, this is achieved by the presence of two unpaired parallel electron spins.

The electronic ground state of a molecule is usually the singlet state S_0 , characterized by a spin quantum number $S=0$. The excitation of an electronic transition by electromagnetic radiation generates an excited singlet state S_1 of the molecule, as the selection rules forbid a change of the spin multiplicity. The lower lying triplet state T_1 of the molecule can be populated from this excited singlet state by a mechanism called Intersystem Crossing (ISC), in which the selection rules are relaxed due to a state mixing caused by the spin-orbit interaction. The processes involved in the triplet state generation are illustrated in Fig. 2.3.

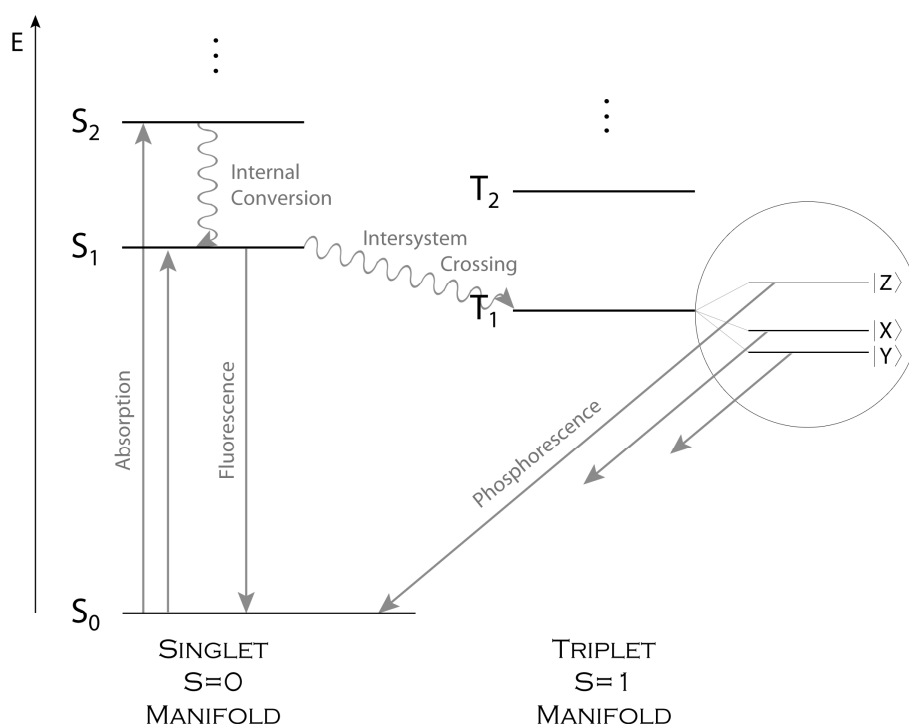


Fig. 2.3 The lowest electronic singlet and triplet energy levels showing the possible transitions. The zero-field splitting of the triplet state sublevels is shown on the right.

An additional process for the population of the triplet state of a molecule is the triplet-triplet energy transfer from the triplet state of another molecule in close proximity.

The wavefunctions describing a singlet and a triplet state, expressed as product of a spatial and a spin wavefunction are:

SINGLET STATE ($S=0, m_s=0$)TRIPLET STATE ($S=1, m_s=+1, 0, -1$)

$${}^1\Psi_0(1,2) = \frac{1}{\sqrt{2}}(\Psi_A\Psi_B + \Psi_B\Psi_A)(\alpha\beta - \beta\alpha)$$

$${}^3\Psi_1(1,2) = | +1 \rangle = \frac{1}{\sqrt{2}}(\Psi_A\Psi_B - \Psi_B\Psi_A)\alpha\alpha$$

$${}^3\Psi_0(1,2) = | 0 \rangle = \frac{1}{\sqrt{2}}(\Psi_A\Psi_B - \Psi_B\Psi_A)(\alpha\beta + \beta\alpha)$$

$${}^3\Psi_{-1}(1,2) = | -1 \rangle = \frac{1}{\sqrt{2}}(\Psi_A\Psi_B - \Psi_B\Psi_A)\beta\beta$$

The singlet state has a symmetric spatial and an antisymmetric spin part, while the triplet state has an antisymmetric spatial part and three sub-states, each characterized by a different m_s value, with a symmetric spin part. Due to the difference of the spatial wavefunction, the electron-exchange contribution to the total energy of the states is different and the triplet state is usually at a lower energy than the corresponding singlet state.

2.3.2 THE TRIPLET STATE IN EPR SPECTROSCOPY

Molecules in a triplet state are paramagnetic and can thus be studied by EPR spectroscopy. The dominating terms of the spin Hamiltonian for a triplet state in the presence of an external magnetic field, as in an EPR experiment, are the electron Zeeman and the zero-field interaction terms:

$$\hat{H}_0 = \frac{\beta_e B_0 g \hat{S}}{\hbar} + \hat{S} D \hat{S}$$

At zero-field ($B_0=0$) only the ZFS term contributes to the spin Hamiltonian, which in the principal axis system of the D tensor may be written as:

$$\hat{H}_{ZFS} = D \left[S_z^2 - \frac{1}{3} S(S+1) \right] + E (S_x^2 - S_y^2)$$

This spin Hamiltonian can be diagonalized to give the following zero-field eigenfunctions, expressed as functions of the basis $| +1 \rangle$, $| 0 \rangle$, $| -1 \rangle$, and eigenvalues:

$$|X\rangle = \frac{1}{\sqrt{2}}(|-1\rangle - |+1\rangle)$$

$$E_X = -D_X = \frac{1}{3}D - E$$

$$|Y\rangle = \frac{i}{\sqrt{2}}(|-1\rangle + |+1\rangle)$$

$$E_Y = -D_Y = \frac{1}{3}D + E$$

$$|Z\rangle = |0\rangle$$

$$E_Z = -D_Z = -\frac{2}{3}D$$

Due to the dipolar interaction of the electron spins the degeneracy of the triplet state sublevels is lifted even in the absence of an external magnetic field, hence this interaction is also called zero-field splitting.

In the presence of the external magnetic field B_0 both the electron Zeeman and the ZFS interaction contribute to the spin Hamiltonian, which may be written as:

$$\hat{H}_0 = \frac{g\beta_e}{\hbar} (B_x \hat{S}_x + B_y \hat{S}_y + B_z \hat{S}_z) + D \left[S_z^2 - \frac{1}{3} S(S+1) \right] + E (S_x^2 - S_y^2)$$

This spin Hamiltonian is most conveniently expressed in the basis $|+1\rangle$, $|0\rangle$, $|-1\rangle$, which corresponds to the eigenfunctions of the Hamiltonian in the limit $B \rightarrow \infty$ (high-field limit):

$$\hat{H}_0 = \begin{matrix} & \begin{matrix} |+1\rangle & |0\rangle & |-1\rangle \end{matrix} \\ \begin{matrix} \langle +1| \\ \langle 0| \\ \langle -1| \end{matrix} & \begin{bmatrix} \frac{g\beta_e B_z}{\hbar} + \frac{1}{3}D & \frac{1}{\sqrt{2}} \frac{g\beta_e}{\hbar} (B_x - iB_y) & E \\ \frac{1}{\sqrt{2}} \frac{g\beta_e}{\hbar} (B_x + iB_y) & -\frac{2}{3}D & \frac{1}{\sqrt{2}} \frac{g\beta_e}{\hbar} (B_x - iB_y) \\ E & \frac{1}{\sqrt{2}} \frac{g\beta_e}{\hbar} (B_x + iB_y) & -\frac{g\beta_e B_z}{\hbar} + \frac{1}{3}D \end{bmatrix} \end{matrix}$$

The eigenfunctions of the complete Hamiltonian can be derived by diagonalization, which is particularly simple when the external magnetic field is directed along one of the principal axes of the ZFS tensor. For an external magnetic field directed along Z ($B_x=B_y=0$) the eigenfunctions, expressed as linear combinations of the eigenfunctions in the high-field limit, and the corresponding eigenvalues are:

$$\begin{aligned} |T_{+1}\rangle &= \cos\theta |+1\rangle - \sin\theta |-1\rangle & E_+ &= \frac{1}{3}D + \left(\frac{g^2\beta_e^2 B^2}{\hbar^2} + E^2 \right)^{\frac{1}{2}} \\ |T_0\rangle &= |0\rangle & E_0 &= -\frac{2}{3}D \\ |T_{-1}\rangle &= \sin\theta |+1\rangle + \cos\theta |-1\rangle & E_- &= \frac{1}{3}D - \left(\frac{g^2\beta_e^2 B^2}{\hbar^2} + E^2 \right)^{\frac{1}{2}} \end{aligned}$$

where the angle θ is defined by:

$$\tan 2\theta = \frac{E}{g\beta_e B}$$

Hence the eigenfunctions and eigenvalues depend on the relative magnitude of the electron Zeeman and the ZFS interaction. In the high-field limit $g\beta_e B \gg D, E$ the eigenfunctions reduce to $|+1\rangle$, $|0\rangle$, $|-1\rangle$ and the eigenvalues are given by the energy in the presence of only the electron Zeeman interaction with a first-order correction due to the ZFS interaction. Analogous solutions are found for an external magnetic field directed along the X or Y axis of the ZFS tensor.

Due to the selection rule $\Delta m_s = \pm 1$, only two transitions are allowed for each orientation of the magnetic field with respect to the principal axes of the ZFS tensor: a lower field $|T_{-1}\rangle \leftrightarrow |T_0\rangle$ (B_i^-) and higher field $|T_0\rangle \leftrightarrow |T_{+1}\rangle$ (B_i^+) transition. In Fig. 2.4 the energies of the triplet state sublevels in a magnetic field directed along the principal axes of the ZFS tensor and the allowed $\Delta M_s = \pm 1$ transitions are depicted for a triplet state system with $D, E < 0$, as for the carotenoid peridinin of the PCP complex.

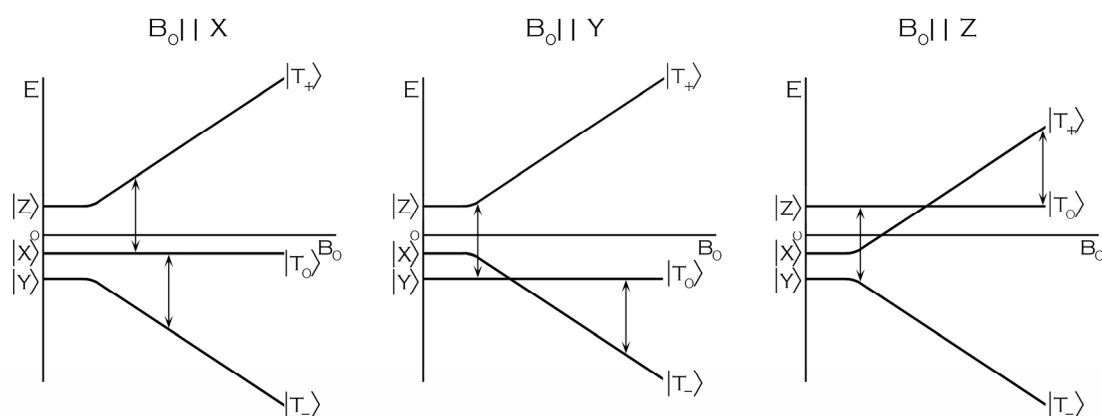


Fig. 2.4 Diagrams of the energies of the triplet state sublevels in a magnetic field parallel to each of the principal axes of the ZFS tensor for a triplet state system with $D, E < 0$.

The EPR spectrum of a single crystal, corresponding to a single orientation of the spin system with respect to the external magnetic field, would therefore consist of two lines at the magnetic field values corresponding to the lower- and higher-field transitions. In disordered samples, such as powders, glasses, frozen solutions etc., the spin system is randomly oriented with respect to the applied field and the EPR spectrum is the sum of all the single crystal spectra for each orientation. The line-shape of such a powder EPR spectrum is characterized by turning points at the canonical orientations, thus the magnetic fields corresponding to the transitions X^- , X^+ , Y^- , Y^+ , Z^- and Z^+ can easily be determined. The ZFS parameters D and E can be determined from the distance between the turning points corresponding to a particular orientation as represented in Fig. 2.5.

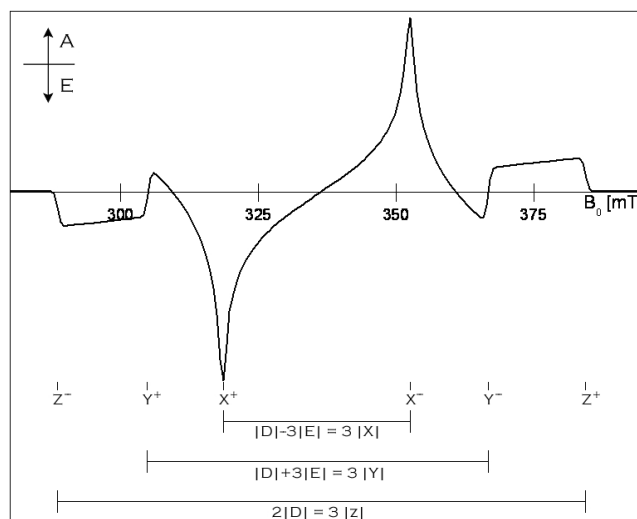


Fig. 2.5 Calculated EPR powder spectrum for a triplet state with $D, E < 0$ and $P_y > P_x > P_z$ with $ea\bar{e}ae\bar{a}$ polarization. The canonical transitions and the determination of the ZFS parameters from their position are illustrated. (A=Absorption, E=Emission).

The intensity of the spectrum at the canonical positions depends on the difference in population between the two levels connected by the corresponding transition. The populations of the triplet state sublevels in an external magnetic field can be expressed as linear combinations of the zero-field sublevel populations:

$$P_i = \sum_k |c_{ik}|^2 P_k \quad i = +1, 0, -1 \quad k = X, Y, Z$$

where c_{ik} are the coefficients expressing the high-field eigenfunctions as linear combinations of the zero-field eigenfunctions. In the high-field approximation assuming $B_0 \parallel Z$ the sublevel populations may be written as:

$$P_0 = P_z \quad P_{\pm 1} = \frac{1}{2}(P_x + P_y)$$

with analogous expressions if the magnetic field is directed along another principal axis of the ZFS tensor. The intensity of a transition may then be written as:

$$I_{0 \rightarrow +1} \propto P_z - \frac{1}{2}(P_x + P_y)$$

Hence the line corresponding to the $0 \rightarrow +1$ transition will be absorptive if $P_z > \frac{1}{2}(P_x + P_y)$ and emissive otherwise.

For a sample at thermal equilibrium, the populations of the triplet state sublevels are given by the Boltzmann distribution and all the transitions are absorptive.

Optically excited triplet states can be studied with TR-EPR or pulse EPR by exciting the sample with a laser prior to the EPR measurement. Each triplet state sublevel is populated with a different rate by the anisotropic Intersystem Crossing (ISC) mechanism, hence the triplet state is formed in a non Boltzmann equilibrium state and the spin populations differ from the thermal equilibrium ones. This effect is called electron spin polarization and causes the EPR lines to be part in enhanced absorption and part in emission, depending on the population difference between the sublevels connected by the corresponding transition. An example of a polarized triplet spectrum with *eaeaea* polarization (*e* = emission, *a* = absorption) is represented in Fig. 2.5. After the formation of a spin-polarized triplet state, spin-lattice relaxation processes tend to restore the equilibrium populations of the sublevels. Accordingly the spin-polarized triplet state spectrum can be observed only at short times after the generation of the triplet state.

2.3.3 TRIPLET-TRIPLET ENERGY TRANSFER

Triplet-Triplet Energy Transfer (TTET) is another mechanism for triplet state generation next to ISC and also produces a spin polarization, which is characteristic of the studied system. TTET is based on the energy transfer from the triplet state of one molecule to the lower-lying triplet state of another molecule. As already mentioned, the photoprotection in photosynthetic antenna complexes is based on this type of energy transfer, which occurs therein between chlorophyll and carotenoid molecules.

The triplet-triplet energy transfer occurs with an electron-exchange mechanism first described by Dexter [5]. The exchange operator does not act on the spin part of the wavefunction and therefore the total spin angular momentum is conserved. The probability of energy transfer between a triplet state sublevel of the donor and a triplet state sublevel of the acceptor can be expressed as a two-centre two-electron exchange integral [17]:

$$p_{h \rightarrow k} \propto \left| \sum_{1,2} \left\langle \varphi^{D^*}(\mathbf{r}_1) T_h^{D^*}(\sigma_1) \varphi^A(\mathbf{r}_2) S_0^A(\sigma_2) \left| \frac{e^2}{|\mathbf{r}_{12}|} \right| \varphi^{A^*}(\mathbf{r}_1) T_k^{A^*}(\sigma_1) \varphi^D(\mathbf{r}_2) S_0^D(\sigma_2) \right\rangle \right|^2$$

$$= \left| \left\langle S_0^A(\sigma_2) \left| S_0^D(\sigma_2) \right\rangle \right|^2 \left| \left\langle T_h^{D^*}(\sigma_1) \left| T_k^{A^*}(\sigma_1) \right\rangle \right|^2 \left| \sum_{1,2} \left\langle \varphi^{D^*}(\mathbf{r}_1) \varphi^A(\mathbf{r}_2) \left| \frac{e^2}{|\mathbf{r}_{12}|} \right| \varphi^{A^*}(\mathbf{r}_1) \varphi^D(\mathbf{r}_2) \right\rangle \right|^2$$

where φ are the spatial wavefunctions, S_0 the singlet ground state spin functions, T the excited triplet state functions at zero field with $h, k = X, Y$ or Z , r_1 and r_2 are the spatial coordinates of the two electrons and σ_1 and σ_2 are the spin coordinates of the two electrons.

The spin angular momentum conservation is based on the assumptions that the spin-orbit coupling is negligible in both the donor and the acceptor molecule and that the energy transfer

occurs with an electrostatic exchange mechanism without contributions of magnetic-type interactions [17]. The present description of the TTET mechanism cannot be applied to systems in which the above assumptions fail. The conservation of the spin direction during TTET has been demonstrated for a number of donor-acceptor systems [18-20] and recently also specifically for the system under investigation, the PCP antenna complex [21].

The TTET mechanism has been investigated with a full density matrix treatment and it has been concluded that the spin population in a given sublevel of the donor is transferred to the different sublevels of the acceptor with a probability proportional to the squared direction cosines relating the ZFS axes of the two molecules in the considered system [22]. Hence the acceptor populations may be written as [18-20,22]:

$$P_k^A = \sum_h \cos^2 \theta_{hk} P_h^D$$

where θ_{hk} is the angle between the ZFS axis h of the donor and the ZFS axis k of the acceptor and P^A and P^D are the zero-field sublevel populations of the acceptor and the donor respectively.

By expressing the sublevel populations in the presence of an external magnetic field as linear combinations of the zero-field sublevel populations, the following final expression for the acceptor's sublevel populations is obtained:

$$P_i^A = \sum_h \sum_k \cos^2 \theta_{hk} |c_{ik}|^2 P_h^D$$

where the term $\cos^2 \theta_{hk}$ defines the relative orientation of the donor and acceptor molecules.

The triplet-triplet energy transfer process can conveniently be studied by EPR spectroscopy. The dependence of the acceptor's sublevel populations on the direction cosines contains structural information on the donor-acceptor pair that can be extracted from the initial spin polarization of the acceptor molecule as measured by TR- or pulse EPR. This method has been exploited for the study of structure-function relationships in antenna complexes [1,14,23,24].

CHAPTER 3

PULSE EPR SPECTROSCOPY

Pulse EPR techniques have been developed in order to overcome the limitations in spectral and time resolution of the continuous wave experiment. Pulse EPR is based on the irradiation of the paramagnetic sample with high-intensity microwave pulses, typically in the order of 16-32 ns.

Pulse EPR experiments with different pulse sequences allow the determination of specific properties of the spin system. In particular the ENDOR (Electron Nuclear Double Resonance) and ESEEM (Electron Spin Echo Envelope Modulation Spectroscopy) techniques are employed to obtain information regarding the interaction of the electron spin with the surrounding nuclei. ENDOR and ESEEM are complementary techniques; generally ENDOR is applied to the study of strong hyperfine interactions, while ESEEM is employed in the study of small hyperfine interactions [25].

Cw-EPR powder spectra are generally characterized by inhomogeneously broadened lines due to the different contributions of different spin packets; hence the hyperfine structure is mostly unresolved. The advantage of pulse EPR techniques is the possibility of exciting specific spin packets and extracting information on the interactions which remain unresolved in cw-EPR spectra.

3.1 SEMI-CLASSICAL DESCRIPTION OF PULSE EPR EXPERIMENTS

A rigorous description of a spin system in a pulse EPR experiment requires a quantum mechanical treatment; however a classical description can give insights into the basic aspects of the experiment. The effect of the microwave pulses on the spin system can be described by the vector model.

A paramagnetic sample in thermal equilibrium in the presence of an external magnetic field B_0 is characterized by a macroscopic magnetization M , given by the sum of the magnetic moments of the paramagnetic particles. This magnetization can be represented by a vector parallel to the external field, considered as directed along the z-axis of the laboratory reference frame. An external magnetic field has no effect on magnetization vectors directed along its axis, but induces a precession around its axis for non-parallel magnetization vectors.

The evolution of the equilibrium magnetization vector during a pulse is most conveniently described by considering a coordinate system rotating around the z axis with an angular frequency ω_0 . The magnetic field B_1 acting on the magnetization during the microwave pulses is directed along one in-plane axis, for example the x-axis, in this rotating coordinate system. During the microwave pulse the magnetization M , initially directed along z, is rotated around the x-axis by an angle $\omega_1 t_p$, depending on the pulse length t_p .

The simplest pulse EPR experiment consists of a single $\frac{\pi}{2}$ pulse applied to a sample at thermal equilibrium. The motion of the magnetization in this experiment is illustrated in Fig. 3.1. The effect of the $\frac{\pi}{2}$ pulse is a rotation of the magnetization from the equilibrium position along the z-axis to its new position along the -y-axis of the rotating frame. After the microwave pulse the magnetization is no more aligned with the external magnetic field B_0 , hence a precession of the magnetization around the z-axis is induced. The magnetization also tends to return to its equilibrium position with two different relaxation mechanisms: the spin-lattice or longitudinal relaxation, which restores the magnetization along the z-axis with a characteristic time T_1 , and the spin-spin or transverse relaxation, which defocuses the transverse magnetization with a characteristic time T_2 . Therefore the transverse magnetization generated by the pulse precesses around the z-axis and decays exponentially with a time constant T_2 . The components of this transverse magnetization, M_x and M_y , are determined and the measured signal is called Free Induction Decay (FID).

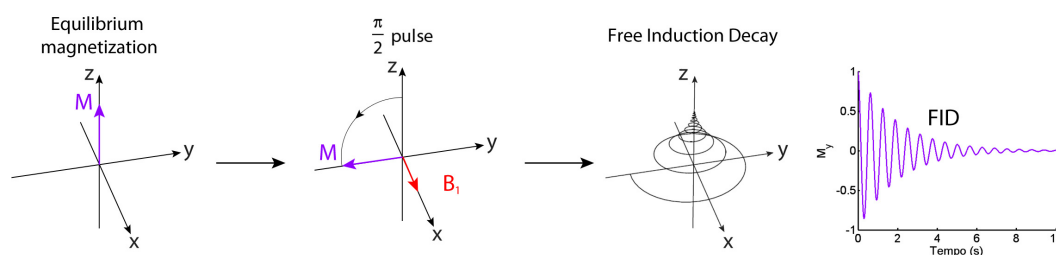


Fig. 3.1 Motion of the magnetization vector M in the rotating frame and generation of the free induction decay signal (FID) for an experiment consisting of a single $\frac{\pi}{2}$ pulse.

Most pulse EPR experiments are based on the detection of a spin echo, the basic pulse sequence for the generation of a spin echo is the two-pulse sequence represented in Fig. 3.2. The first pulse transforms the longitudinal magnetization into transverse magnetization, as described above. During the first free evolution time interval τ the different spin packets constituting the magnetization precess around the z-axis at different characteristic frequencies, causing the magnetization to defocus. The microwave field acting during the π pulse induces a rotation of all the magnetization vectors around the x-axis by 180° . After the pulse the spin packets continue to precess around z at their characteristic frequency, refocusing after another time interval τ along the y-axis (Fig. 3.2). The resulting net magnetization directed along y is called an electron spin echo.

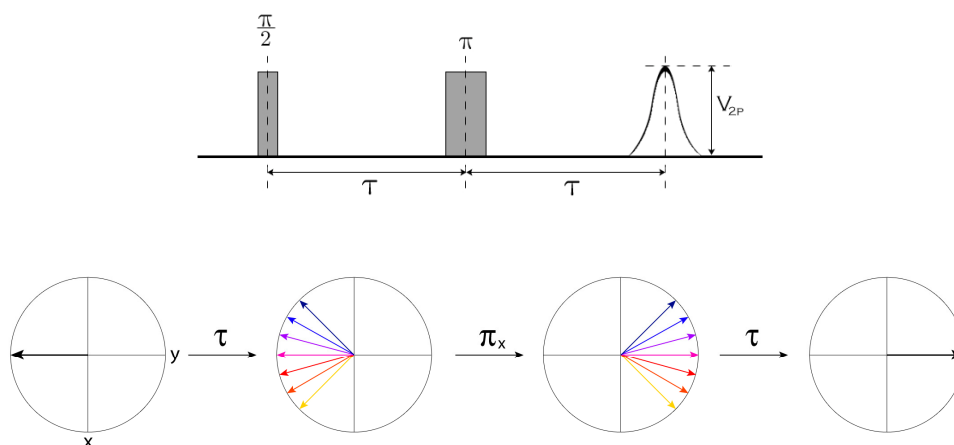


Fig. 3.2 Pulse sequence and diagrams describing the motion of the magnetization vectors in the rotating frame in a two-pulse echo experiment.

An electron spin echo can be obtained with other pulse sequences as well; the most common next to the two-pulse or primary echo sequence is the three-pulse or stimulated echo sequence consisting of three $\frac{\pi}{2}$ pulses.

3.2 ECHO-DETECTED FIELD-SWEPT EPR

Echo-detected field-swept EPR is based on the detection of the electron spin echo. The two-pulse and three-pulse echo sequences are the most commonly employed pulse schemes for the generation of the electron spin echo. The echo signal is measured at different values of the external magnetic field and the integrated intensity is computed at each value leading to a spectrum analogous to the cw-EPR spectrum.

Field-swept pulse techniques are of particular importance in the study of short-lived species

generated for example by a laser pulse. In the study of photo-excited triplet states the pulse sequence is preceded by a laser pulse generating the paramagnetic species (Fig. 3.3). Echo-detected EPR spectra recorded at variable delay-after-flash (DAF) periods between the laser pulse and the microwave sequence allow the study of the time evolution of the spin system.

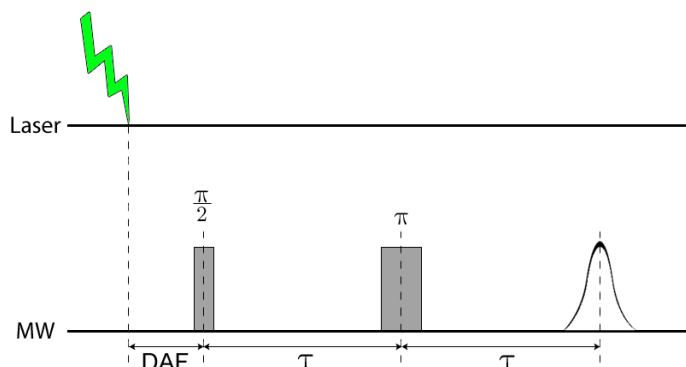


Fig 3.3 Pulse sequence of the two-pulse echo-detected field-swept EPR experiment.

The excitation of the sample by a laser pulse prior to the pulse sequence is a common characteristic of all pulse EPR experiments applied to photo-induced paramagnetic species.

3.3 ESEEM SPECTROSCOPY

3.3.1 GENERAL ASPECTS OF ESEEM SPECTROSCOPY

Electron Spin Echo Envelope Modulation (ESEEM) Spectroscopy is a pulse EPR technique employed for the study of small hyperfine interactions in paramagnetic systems in solid samples. The sample is subjected to a series of microwave pulses producing a spin echo, whose intensity is modulated by the interaction with the surrounding nuclei for increasing inter-pulse delays. The analysis of the obtained modulated spin echo envelope allows the determination of the hyperfine and nuclear quadrupole interaction parameters of these nuclei and thus to gain information on the local geometry and electronic structure of the considered system.

The modulation of spin echo envelopes with nuclear frequencies was first observed and described by Rowan, Hahn and Mims in 1965 [26]. A theoretical description of the echo modulation was given in this first article and was later generalized by Mims [27], allowing the use of this technique in the study of a variety of paramagnetic systems [28].

Nuclear modulation effects can be observed with a number of different pulse schemes, the most important experiments are the two-pulse ESEEM, the three-pulse ESEEM and the HYSORE experiment. The corresponding pulse sequences are shown in Fig. 3.4.

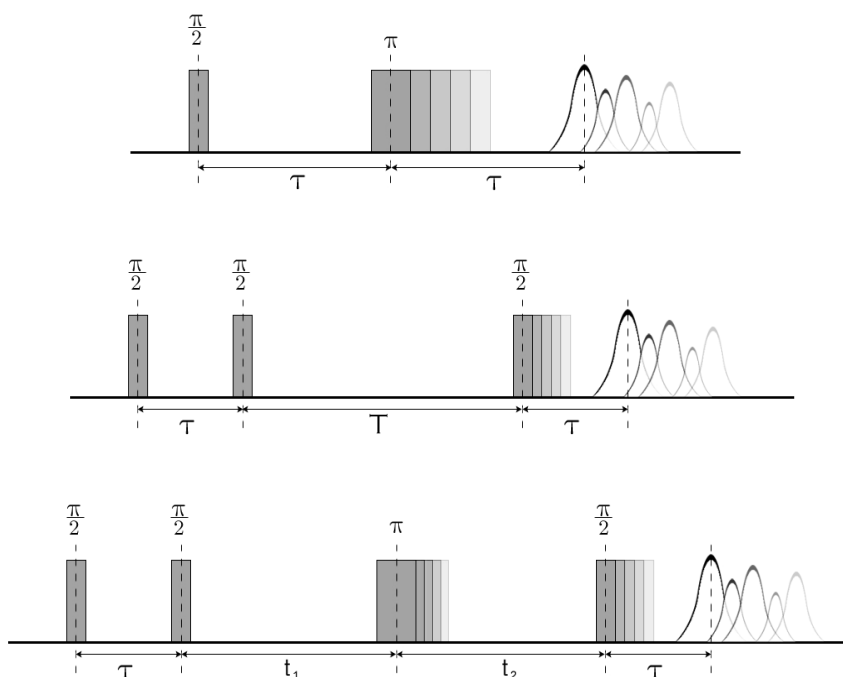


Fig. 3.4 Modulation of the spin echo-envelope in the two-pulse ESEEM, three-pulse ESEEM and HYSCORE experiment.

The amplitude of the spin echo varies in time due to two different effects: modulation effects and relaxation processes. The modulation effects cause a periodic variation of the spin echo amplitude and are at the basis of the ESEEM experiment. During the inter-pulse delays the transverse magnetization also tends to its equilibrium position by longitudinal (T_1) and transverse (T_2) relaxation processes that cause a monotonous decay of the intensity of the spin echo with time. The detected spin echo intensity can thus be written as a product of two distinct terms:

$$I_{\text{echo}} = E_{\text{mod}} E_{\text{decay}}$$

E_{mod} describes the modulation of the spin echo amplitude due to the coupling of the paramagnetic system to surrounding nuclei and can be derived with the density matrix formalism, as explained in detail in the next chapter. The relaxation effect E_{decay} can be approximated by an exponential decay depending on the phase memory time of the electron and nuclear spins.

Experimentally the echo intensity is measured as a function of the inter-pulse delays and the obtained time domain data are Fourier transformed to the frequency domain to identify the nuclear frequencies contributing its modulation. The experimental data are interpreted by simulation of either the time trace or the spectrum, or both, and the hyperfine and nuclear quadrupole interaction parameters are determined.

3.3.2 SEMI-CLASSICAL DESCRIPTION OF THE ESEEM EXPERIMENT

The origin of the modulation of the spin echo envelope can be described qualitatively by considering a nuclear spin I at a distance r from an electron spin S in the presence of an external magnetic field B_0 [26,28,29] (Fig. 3.1). Each spin produces a dipolar magnetic field in the position of the other spin. The field produced by the nuclear spin at the position of the electron spin ($B_n \propto \beta_n r^{-3}$) is typically so small with respect to B_0 that it can be neglected and the electron spin can be considered aligned with the external magnetic field. The field produced by the electron spin at the position of the nuclear spin ($B_e \propto \beta_e r^{-3}$) on the other hand is of comparable magnitude with the external magnetic field B_0 and combines vectorially with it to produce an effective field along which the nuclear spin is aligned at equilibrium. If the electron spins are reoriented by a microwave pulse, which is short compared to the Larmor period of the nuclear spin, the effective magnetic field at the nucleus changes too fast for the nuclear spins to adiabatically follow it. Thus the nuclear spins begin to precess around the new effective field and induce local variable fields at the position of the electron spin (Fig.3.5). As a result the electron precession frequency becomes modulated at the precession frequency of the neighbouring nucleus.

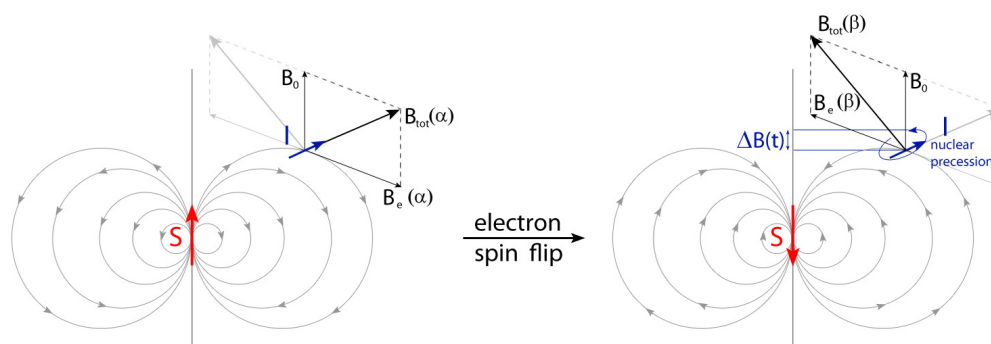


Fig. 3.5 Diagram showing the origin of the echo modulation: Magnetic fields acting on the nuclear spin and effect of the reversion of the quantization direction of the electron spin by a microwave pulse.

It is clear from this description, that a modulation can only be observed if the electron and nuclear spins have different quantization axes in an external magnetic field. This condition is fulfilled in the intermediate coupling regime, where the magnitudes of the nuclear Zeeman interaction and of the hyperfine interaction are comparable.

3.3.3 TWO-PULSE ESEEM

The two-pulse ESEEM pulse sequence is the primary echo pulse sequence represented in Fig. 3.6. The time interval τ between the pulses is successively incremented and the signal intensity at

the maximum of the echo is measured as a function of τ . The initial value of τ is determined by the dead time of the instrument. The instrumental dead time arises because the spin echo signal can be detected only after the dissipation of the high power microwave pulses.

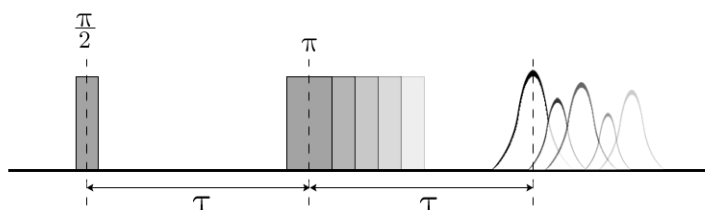


Fig. 3.6 Illustration of the modulation of the spin echo envelope in a two-pulse ESEEM experiment.

In this experiment the time-decay of the echo intensity depends on the phase memory time T_m of the electron spins. The echo intensity expressed as a function of the time τ can be approximated to:

$$I_{\text{echo}}(\tau, 2p) = E_{\text{mod}}(\tau, 2p) \exp\left[-\frac{2\tau}{T_m}\right]$$

In the two-pulse spin echo experiment, the phase memory time is defined as the time between the first pulse and the echo needed to obtain an attenuation of e^{-1} of the echo signal [30]. The phase memory time can often be identified as spin-spin relaxation time T_2 , but local differences in the magnetic field may contribute as well, as they also lead to the dephasing of the magnetization vectors relative to different spin packets.

3.3.4 THREE-PULSE ESEEM

The three-pulse ESEEM pulse sequence is the stimulated echo pulse sequence represented in Fig. 3.7. In the three-pulse ESEEM experiment the first two pulses are separated by a fixed time interval τ and the time interval T between the second and third pulse is incremented in successive experiments.

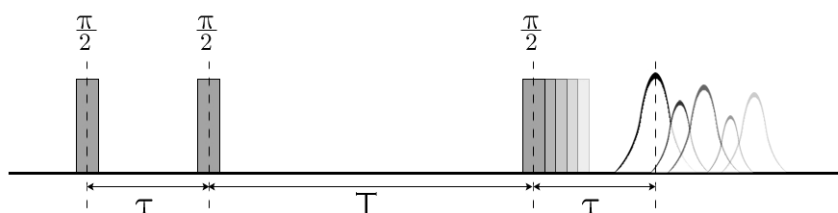


Fig. 3.7 Illustration of the modulation of the spin echo envelope in a three-pulse ESEEM experiment.

The complete expression for the echo intensity, taking into account also the relaxation effects by considering a common phase memory time T_m for all the electron transitions and $T_m^{(n)}$ for all the nuclear transitions, may be written as:

$$I_{\text{echo}}(\tau, T, 3p) = E_{\text{mod}}(\tau, T, 3p) \exp\left[-\frac{2\tau}{T_m}\right] \exp\left[-\frac{T}{T_m^{(n)}}\right]$$

The phase memory time $T_m^{(n)}$ of the nuclear spins is usually much longer than the phase memory time of the electron spins. An important consequence of this is that generally the decay of the three-pulse ESEEM time traces is much slower than that of two-pulse ESEEM time traces. Furthermore, while in the two-pulse experiment the line-widths in the ESEEM spectra are determined by the electron spin phase memory time, the line-widths in the three-pulse experiment are determined by the longer nuclear spin phase memory time, leading to an important increase in resolution.

3.4 HYSORE

HYSORE (Hyperfine Sublevel Correlation Spectroscopy) is the most important two-dimensional variant of the ESEEM experiment. In this experiment, the nuclear frequencies of different electron spin manifolds are correlated, improving the resolution and providing additional information on the spin system.

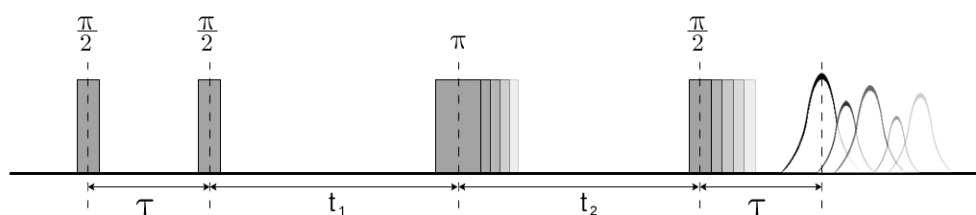


Fig. 3.8 Illustration of modulation of the spin echo envelope in a HYSORE experiment.

The HYSORE experiment was derived from the three-pulse experiment by Höfer *et al.* [31]. An additional π pulse acts as the mixing pulse and creates correlations between nuclear spin transitions associated to different electron spin manifolds [32]. The pulse sequence of the HYSORE experiment is depicted in Fig. 3.8. The time intervals t_1 and t_2 are independently incremented in consecutive experiments.

The effect of the mixing pulse is pictorially described in Fig. 3.9 for a $S = \frac{1}{2}$, $I = \frac{1}{2}$ system: after the π pulse, the nuclear spins, which have evolved with frequency ω_a during t_1 , evolve with the

frequency ω_β during t_2 . The 2D Fourier transform of the time domain data yields a spectrum with cross peaks at $(\omega_\alpha, \omega_\beta)$ and $(\omega_\beta, \omega_\alpha)$.

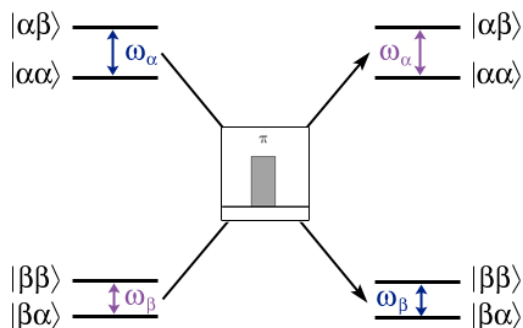


Fig. 3.9 Illustration of the effect of the mixing π pulse in the HSCORE experiment on a $S = \frac{1}{2}$, $I = \frac{1}{2}$ spin system.

The general modulation formula, assuming common phase memory times for all electron and nuclear transitions, is given by:

$$I_{\text{echo}}(\tau, t_1, t_2, 4p) = E_{\text{mod}}(\tau, t_1, t_2, 4p) \exp\left[-\frac{2\tau}{T_m}\right] \exp\left[-\frac{t_1 + t_2}{T_m^{(n)}}\right]$$

The HSCORE experiment is thus characterized by the same advantages as the three-pulse ESEEM experiment as regards the line-width of the signals in the spectrum obtained by Fourier transform.

CHAPTER 4

THEORY OF ESEEM

The modulation of the spin echo envelope due to the interaction of an electron spin with a nuclear spin can be described quantitatively by quantum mechanical calculations. A density matrix formalism for obtaining explicit analytical expressions for the modulation of the spin echo was first introduced by Rowan, Hahn and Mims [26] and later generalized and described in detail by Mims [27].

4.1 QUANTUM MECHANICAL DESCRIPTION OF ESEEM

The evolution of the spin states during the pulses and during the periods of free evolution of a specific pulse sequence is described by the density matrix formalism. In general the time-evolution of a density matrix $\hat{\rho}$ under the effect of a certain Hamiltonian \hat{H} is described by the Liouville-von Neumann equation:

$$\frac{d\hat{\rho}}{dt} = i[\hat{\rho}, \hat{H}]$$

where $[\hat{\rho}, \hat{H}]$ is the commutator between the density matrix ρ and the Hamiltonian H . For a time-independent Hamiltonian this equation of motion is readily solved and the density matrix at the end of a time interval t_f is obtained by similarity transform of the density matrix at the beginning of the time interval t_i :

$$\hat{\rho}(t_f) = \hat{R}_t^{-1} \hat{\rho}(t_i) \hat{R}_t \quad \text{with} \quad \hat{R}_t = \exp[i(t_f - t_i)\hat{H}]$$

The density matrix at the time of the spin echo ($\hat{\rho}_E$) generated by a specific pulse sequence is calculated by dividing the pulse sequence into periods of nutation during the pulses and periods

of free precession in the inter-pulse delays, during which a time-independent Hamiltonian acts on the system, and by applying the Liouville-von Neumann equation for each period.

In the periods of free precession the spin Hamiltonian H_0 acts on the system. The spin Hamiltonian for an arbitrary electron spin S interacting with a nuclear spin I can be written in angular frequency units as:

$$\begin{aligned}\hat{H}_0 &= \hat{H}_S + \hat{H}_{NZ} + \hat{H}_{HFI} + \hat{H}_{NQI} \\ &= \hat{H}_S - \omega_I \hat{I} + \hat{S} A \hat{I} + \hat{I} P \hat{I}\end{aligned}$$

where \hat{H}_S is the part of the Hamiltonian relative to the electron spin, the second term describes the nuclear Zeeman interaction of the nuclear spin, the third the hyperfine interaction of the electron spin with the nuclear spin and the last term the nuclear quadrupole interaction for nuclei with $I > \frac{1}{2}$. In ESEEM spectroscopy cases for which the relation $\hat{H}_S \gg \hat{H}_{NZ} + \hat{H}_{HFI} + \hat{H}_{NQI}$ is valid are considered. Depending on the type of spin system, \hat{H}_S may contain electron Zeeman and ZFS terms, and in some cases also large electron nuclear couplings.

During the microwave pulses the Hamiltonian acting on the system is the sum of the time-independent spin Hamiltonian \hat{H}_0 and the time-dependent Hamiltonian \hat{H}_1 , describing the interaction with the microwave field B_1 :

$$\hat{H}_1 = \omega_N S_x \cos \omega_{mw} t$$

The time-dependence is removed by transformation into the rotating frame.

The exponential operators acting on the density matrix during the periods of nutation, R_N , and of free precession, R_t , in the rotating frame are respectively:

$$\begin{aligned}R_N &= \exp \left[i(\hat{H}_0 + \hat{H}_1) t_p \right] \approx \exp \left[i\hat{H}_1 t_p \right] \\ R_t &= \exp \left[i\hat{H}_0 t \right]\end{aligned}$$

In the eigenbasis of the spin Hamiltonian the free precession operators are diagonal, while the nutation operators are not. The calculations can be simplified by assuming $\hat{H}_0 < \hat{H}_1$, i.e. that the pulses are short and strong compared to the interactions in the spin Hamiltonian. In this case of ideal pulses the nutation operator can be derived explicitly.

The final density matrix is obtained by applying nutation and free precession operators to the initial density matrix according to the considered pulse sequence. In the eigenbasis of the spin Hamiltonian, the initial density matrix $\hat{\rho}_0$ is diagonal and its elements represent the initial

populations of the energy levels, which can correspond to the Boltzmann equilibrium or to polarized populations.

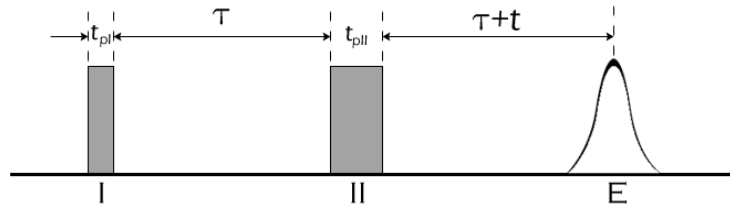


Fig. 4.1 Periods of nutation and free precession in the two-pulse ESEEM pulse sequence

In the case of the two-pulse ESEEM experiment (Fig. 4.1), the final density matrix is given by:

$$\hat{\rho}_E = R_{\tau+t}^{-1} R_{NII}^{-1} R_{\tau}^{-1} R_{NI}^{-1} \rho_0 R_{NI} R_{\tau} R_{NII} R_{\tau+t}$$

The echo amplitude is proportional to the magnetization of the y-component at the time of the echo and is expressed as:

$$E(t) = \text{Tr}(\hat{\rho}_E \hat{S}_y)$$

The echo signal is normalized to unity at $t=0$ by division with the echo signal calculated for the initial density matrix. The signal is readily calculated given the density matrix at the time of the echo.

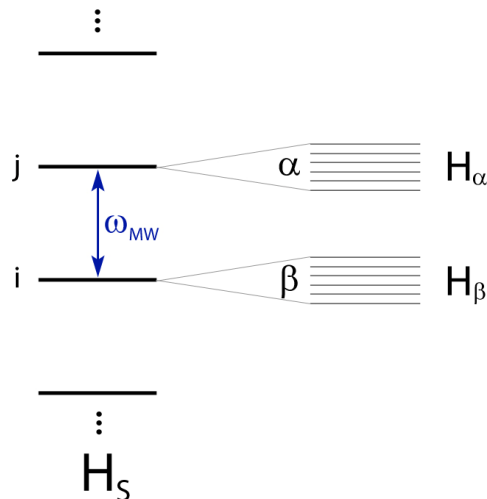


Fig. 4.2 Energy level diagram for a generic spin system. Each level of H_S is split into a manifold of nuclear sublevels due to nuclei with small hyperfine couplings that are observed in the pulse EPR experiment.

The calculation of the echo signal for a generic spin system (Fig. 4.2) following the procedure described above is simplified by introducing a partitioning of the Hamiltonian matrix into four sub-matrices of dimensions $(2I+1)$ [27]:

$$H = \begin{array}{cc} & \begin{array}{c} \alpha \text{ states} \\ \beta \text{ states} \end{array} \\ \begin{array}{c} \alpha \text{ states} \\ \beta \text{ states} \end{array} & \begin{bmatrix} \text{submatrix } \alpha_i \alpha_i & \text{submatrix } \alpha_i \beta_j \\ \text{submatrix } \beta_j \alpha_i & \text{submatrix } \beta_j \beta_j \end{bmatrix} \end{array}$$

The rationale for this partitioning procedure lies in the fact that the much faster precession of the electron spin with respect to the nuclear spin leads to a time-averaged effect of the electron spin on the nucleus, which is different for each electron spin eigenstate. Hence the operator \hat{S} in the hyperfine interaction term of the spin Hamiltonian can be substituted by its eigenvalue in a particular eigenstate and the spin Hamiltonian can be partitioned into separate nuclear sub-Hamiltonians, each corresponding to a particular electron spin manifold:

$$\hat{H}_i = -\omega \hat{I} + \langle i | \hat{S} | i \rangle A \hat{I} + \hat{I} \hat{P}$$

The nuclear sub-Hamiltonians H_i are diagonalized separately yielding eigenfrequencies ω_i and eigenvector matrices M_i . The eigenvector matrices describe the state mixing caused by the hyperfine interaction in the electron spin manifolds. The product of the two eigenvector matrices gives the unitary overlap matrix between the nuclear eigenstates of the two considered electron spin manifolds:

$$M = M_j^\dagger M_i$$

The Hamiltonian acting on the spin system during the microwave pulses is transformed into the eigenbasis of the spin Hamiltonian by effect of the eigenvector matrices M_i and M_j :

$$\hat{H}_1 = \omega_N \begin{bmatrix} M_j^\dagger & 0 \\ 0 & M_i^\dagger \end{bmatrix} \hat{S}_x \begin{bmatrix} M_j & 0 \\ 0 & M_i \end{bmatrix}$$

Once the Hamiltonians acting on the spin system during the periods of free precession and of nutation have been defined in the eigenbasis of the spin Hamiltonian, the elements of the general expression of the echo modulation can be calculated and the explicit expression for the echo modulation for a specific spin system and a specific pulse sequence can be obtained by substitution and algebraic simplification.

4.2 ESEEM FOR A $S = 1/2$, $I = 1/2$ SYSTEM

In the simple case of a $S = 1/2$, $I = 1/2$ system with an isotropic g tensor the static spin Hamiltonian in the rotating frame may be approximated to [25]:

$$\hat{H}_0 = \Omega_S S_z - \omega_I I_z + A S_z I_z + B S_z I_x$$

where $A = A_{zz}$ and $B = \sqrt{A_{zx}^2 + A_{zy}^2}$ take into account the secular and pseudo-secular hyperfine couplings, ω_I is the nuclear Larmor frequency and $\Omega_S = \omega_S - \omega_0$ is the resonance offset. The non-secular terms with S_x and S_y can be neglected, assuming that the electron spin is quantized along the direction of the magnetic field B_0 (high-field approximation).

For an axially symmetric hyperfine tensor the coefficients A and B can be expressed in terms of the isotropic and dipolar coupling constants a_{iso} and T:

$$A = a_{iso} + T(3 \cos^2 \theta - 1)$$

$$B = 3 T \sin \theta \cos \theta$$

where θ is the angle between the magnetic field B_0 and the molecular frame.

The energy level diagram for this spin system is reported in Fig. 4.3. The spin Hamiltonian can be partitioned into two nuclear sub-Hamiltonians relative to the α and β manifolds:

$$\hat{H}_\alpha = -\omega_I I_z + \frac{1}{2} A I_z + \frac{1}{2} B I_x$$

$$\hat{H}_\beta = -\omega_I I_z - \frac{1}{2} A I_z - \frac{1}{2} B I_x$$

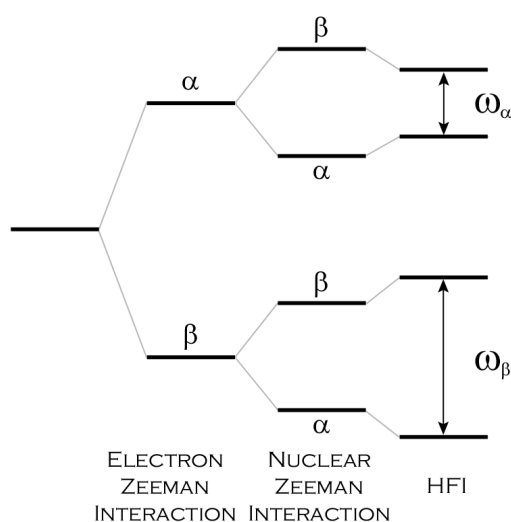


Fig. 4.3 Energy levels and nuclear transition frequencies for a $S = 1/2$, $I = 1/2$ spin system.

The free precession operator can thus be written as:

$$R_t = \begin{bmatrix} \exp[i\hat{H}_\alpha t] & 0 \\ 0 & \exp[i\hat{H}_\beta t] \end{bmatrix}$$

The eigenfrequencies of the nuclear sub-Hamiltonians are:

$$\omega_\alpha = \sqrt{\left(\frac{A}{2} - \omega_l\right)^2 + \frac{B^2}{4}} \quad \omega_\beta = \sqrt{\left(\frac{A}{2} + \omega_l\right)^2 + \frac{B^2}{4}}$$

The diagonalization is effected by means of the rotation operators $\exp[-il_y \xi]$ and $\exp[-il_y \eta]$, where:

$$\tan \xi = \frac{B}{(A - 2\omega_l)} \quad \tan \eta = \frac{B}{(A + 2\omega_l)}$$

The overlap matrix M is defined as the product of the eigenvector matrices obtained for the two electron spin manifolds and is in this case equal to:

$$M = \begin{bmatrix} \cos \frac{1}{2}(\eta - \xi) & \sin \frac{1}{2}(\eta - \xi) \\ -\sin \frac{1}{2}(\eta - \xi) & \cos \frac{1}{2}(\eta - \xi) \end{bmatrix}$$

The angle $(\eta - \xi)$ is the angle between the two nuclear quantization axes, one corresponding to the electron spin α , the other to the electron spin β (Fig. 4.4).

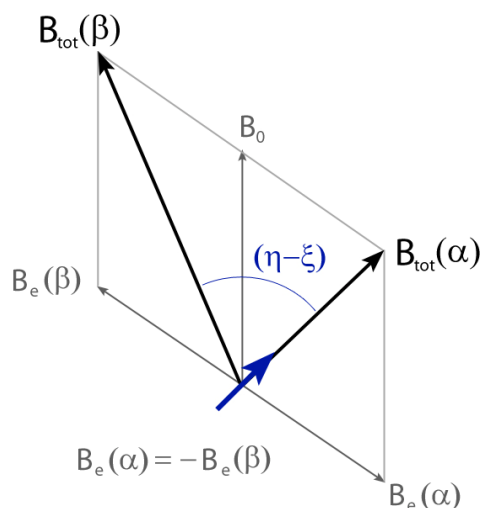


Fig. 4.4 Magnetic fields acting in the position of the nucleus and quantization axes of the nuclear spin coupled to an electron spin in the α or β state.

In the assumption of ideal pulses the Hamiltonian H_1 is proportional to S_x , which for $S = \frac{1}{2}$ is:

$$S_x = \begin{matrix} & |\alpha\rangle & |\beta\rangle \\ \langle\alpha| & \begin{bmatrix} 0 & \frac{1}{2} \end{bmatrix} \\ \langle\beta| & \begin{bmatrix} \frac{1}{2} & 0 \end{bmatrix} \end{matrix}$$

Hence the Hamiltonian acting during the microwave pulses and the corresponding nutation operator are:

$$\hat{H}_1 = \frac{1}{2} \omega_N \begin{bmatrix} 0 & M \\ M^\dagger & 0 \end{bmatrix} \quad R_N = \begin{bmatrix} \cos\left(\frac{\omega_N t_p}{2}\right) & iM \sin\left(\frac{\omega_N t_p}{2}\right) \\ iM^\dagger \sin\left(\frac{\omega_N t_p}{2}\right) & \cos\left(\frac{\omega_N t_p}{2}\right) \end{bmatrix}$$

After having thus defined the free precession and nutation operators, the expression for the spin echo envelope modulation can be obtained for a specific pulse sequence.

4.2.1 TWO-PULSE ESEEM

The echo modulation in a two-pulse ESEEM experiment for a $S = \frac{1}{2}$, $I = \frac{1}{2}$ system is [27]:

$$E_{\text{mod}}(\tau) = 1 - 2k \sin^2\left(\frac{\omega_\alpha \tau}{2}\right) \sin^2\left(\frac{\omega_\beta \tau}{2}\right)$$

which, in order to emphasize the dependence on the nuclear frequencies and their sums and differences, can be rewritten as [29]:

$$E_{\text{mod}}(\tau) = 1 - \frac{k}{4} \left[2 - 2 \cos \omega_\alpha \tau - 2 \cos \omega_\beta \tau + \cos(\omega_\alpha - \omega_\beta) \tau + \cos(\omega_\alpha + \omega_\beta) \tau \right]$$

with the modulation depth k defined as:

$$k = \sin^2(\eta - \xi) = \left(\frac{\omega_B}{\omega_\alpha \omega_\beta} \right)^2$$

The echo envelope is modulated by the nuclear frequencies of the two electron spin manifolds, as well as by their sum and difference frequencies. The amplitude of the modulations is defined by the modulation depth parameter k . The presence of the parameter B , depending on the anisotropic hyperfine interaction, in the expression of the modulation depth parameter indicates that modulation is only observed if there is an anisotropic hyperfine interaction, as is generally the case in solids, while in liquids the anisotropic interactions are averaged out by the fast

thermal motion. Additionally, as B is function of the non-diagonal elements of the hyperfine tensor, the echo modulation vanishes at the canonical orientations, where the external magnetic field B_0 is parallel to one of the principal axes of the hyperfine tensor.

The main characteristic of the two-pulse experiment is the modulation of the echo envelope both by the nuclear frequencies and by their sum and difference frequencies. The time domain data are transformed into frequency domain data by Fourier transform in order to detect the frequencies the spin echo envelope is modulated with. In the two-pulse ESEEM spectrum the nuclear frequencies appear as peaks with positive amplitude, while the combination frequencies give peaks with negative amplitude.

4.2.2 THREE-PULSE ESEEM

The expression for the spin echo envelope modulation in a three-pulse ESEEM experiment on a $S = \frac{1}{2}$, $I = \frac{1}{2}$ system is [27]:

$$\begin{aligned} E_{\text{mod}}(\tau, T) &= 1 - \frac{k}{2} + \frac{k}{4} \left[\cos \omega_\alpha \tau + \cos \omega_\beta \tau + (1 - \cos \omega_\beta \tau) \cos \omega_\alpha (\tau + T) + (1 - \cos \omega_\alpha \tau) \cos \omega_\beta (\tau + T) \right] \\ &= 1 - k \left[\sin^2 \frac{\omega_\alpha \tau}{2} \sin^2 \frac{\omega_\beta (\tau + T)}{2} + \sin^2 \frac{\omega_\beta \tau}{2} \sin^2 \frac{\omega_\alpha (\tau + T)}{2} \right] \end{aligned}$$

where the modulation depth parameter k and the nuclear frequencies are defined as in the two-pulse ESEEM experiment.

An inspection of the echo modulation functions shows the absence of the sum and difference frequencies, which were present in the two-pulse experiment. This is usually an advantage, as the reduced number of peaks simplifies the spectrum obtained by Fourier transform of the time domain data.

The three-pulse echo modulation depends both on τ and T . A significant difference with respect to the two-pulse experiment is that the modulation amplitudes are a function of τ . The $(1 - \cos \omega_i \tau)$ terms in the above expression describe the dependence of the amplitude of the modulation at a nuclear frequency of one electron spin manifold on τ and on a nuclear frequency of the other manifold. Due to the τ -dependence of the modulation amplitudes in the three-pulse ESEEM experiment, blind spots may appear in the spectrum, i.e. for particular values of τ some frequencies may be suppressed. The resulting suppression holes in the ESEEM spectrum can lead to misinterpretation, thus it is common practice to repeat the three-pulse experiment for different values of τ . The frequencies suppressed for a particular value of τ are given by:

$$\omega = \frac{2\pi n}{\tau} \quad (n = 0, 1, 2 \dots)$$

The suppression effect can also be an advantage, as it can be exploited to suppress unwanted frequencies. The most convenient τ value may be chosen based on the above equation. Analogously the modulation at a particular frequency can be maximized by choosing certain values of τ according to:

$$\tau = \frac{2\pi(n + \frac{1}{2})}{\omega}$$

The modulation due to a particular type of nucleus can thus be maximized by adjusting τ .

4.3 ESEEM FOR A $S = 1/2, I = 1$ SYSTEM

The nuclear modulation effects of nuclei with $I > 1$ are due not only to the nuclear Zeeman and hyperfine interaction, but also to the nuclear quadrupole interaction. The energy levels of a $S = 1/2$ system coupled to a nucleus with spin $I = 1$ are depicted in Fig. 4.5.

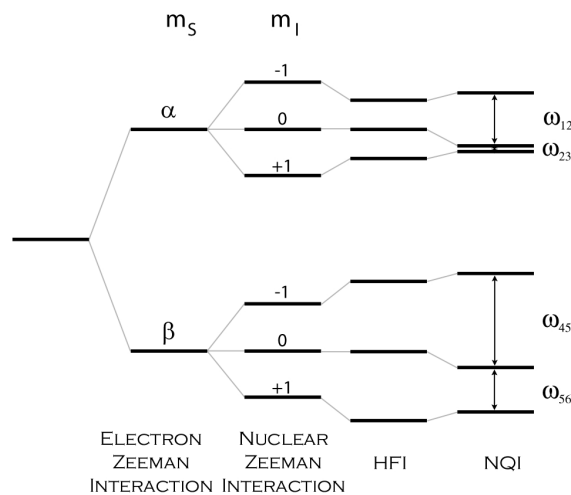


Fig. 4.5 Energy levels and nuclear transition frequencies for a $S = 1/2, I = 1$ spin system in the limit of nuclear Zeeman interaction > hyperfine interaction > nuclear quadrupole interaction.

An analytical diagonalization of the nuclear sub-Hamiltonians for $I=1$, comprising nuclear Zeeman, hyperfine and nuclear quadrupole interaction, is of considerable difficulty. If the nuclear quadrupole interaction can be assumed small with respect to the nuclear Zeeman and hyperfine interaction, as is generally legitimate for deuterium nuclei, a simplified treatment can be used, in which the effect of the nuclear quadrupole interaction is taken into account in the nuclear frequencies, but neglected in the computation of the eigenvector matrices M [27]. The nuclear

frequencies are calculated by diagonalization of the nuclear sub-Hamiltonians, neglecting the nuclear quadrupole interaction, and are corrected by applying first-order perturbation theory:

$$S = \frac{1}{2}, I = 1$$

$$\omega_\alpha = \sqrt{\left(\frac{A}{2} - \omega_1\right)^2 + \frac{B^2}{4}} \quad \omega_\beta = \sqrt{\left(\frac{A}{2} + \omega_1\right)^2 + \frac{B^2}{4}}$$

$$\omega_{12} = \omega_\alpha + \Delta_\alpha \quad \omega_{23} = \omega_\alpha - \Delta_\alpha \quad \omega_{45} = \omega_\beta + \Delta_\beta \quad \omega_{56} = \omega_\beta - \Delta_\beta$$

where the correction terms Δ_α and Δ_β are defined as follows for an axially symmetric nuclear quadrupole interaction [33,34]:

$$\Delta = \frac{e^2 q Q}{4I(2I-1)} \left(\frac{3 \cos^2 \theta - 1}{2} \right) [3m_l^2 - I(I+1)]$$

with θ is the angle between the nuclear quadrupole tensor and the effective magnetic field interacting with the nucleus.

The overlap matrix M for the $S = \frac{1}{2}, I = 1$ system, calculated neglecting the nuclear quadrupole interaction, is:

$$M = \begin{bmatrix} \frac{1}{2}[1 + \cos(\eta - \xi)] & -\frac{1}{\sqrt{2}}\sin(\eta - \xi) & \frac{1}{2}[1 - \cos(\eta - \xi)] \\ \frac{1}{\sqrt{2}}\sin(\eta - \xi) & \cos(\eta - \xi) & -\frac{1}{\sqrt{2}}\sin(\eta - \xi) \\ \frac{1}{2}[1 - \cos(\eta - \xi)] & \frac{1}{\sqrt{2}}\sin(\eta - \xi) & \frac{1}{2}[1 + \cos(\eta - \xi)] \end{bmatrix}$$

where the angle $(\eta - \xi)$ is again the angle between the two quantization axes of the nuclear spin corresponding to different electron spin states.

The normalized envelope modulation functions for the two- and three-pulse ESEEM experiment are [27]:

$$\begin{aligned} \text{Two-pulse ESEEM} \quad S = \frac{1}{2}, I = 1 \\ E_{\text{mod}}(\tau) = \left(1 - \frac{4}{3}k + \frac{3}{4}k^2\right) + \left(\frac{2}{3}k - \frac{1}{2}k^2\right) [\cos \omega_{12}\tau + \cos \omega_{23}\tau + \cos \omega_{45}\tau + \cos \omega_{56}\tau] \\ - \left(\frac{1}{6}k + \frac{1}{6}k\sqrt{1-k} - \frac{1}{6}k^2\right) [\cos(\omega_{12} + \omega_{45})\tau + \cos(\omega_{12} - \omega_{45})\tau + \cos(\omega_{23} + \omega_{56})\tau + \cos(\omega_{23} - \omega_{56})\tau] \\ - \left(\frac{1}{6}k - \frac{1}{6}k\sqrt{1-k} - \frac{1}{6}k^2\right) [\cos(\omega_{23} + \omega_{45})\tau + \cos(\omega_{23} - \omega_{45})\tau + \cos(\omega_{12} + \omega_{56})\tau + \cos(\omega_{12} - \omega_{56})\tau] \\ + \frac{1}{4}k^2 [\cos \omega_{13}\tau + \cos \omega_{46}\tau] + \frac{1}{24}k^2 [\cos(\omega_{13} + \omega_{46})\tau + \cos(\omega_{13} - \omega_{46})\tau] \\ - \frac{1}{12}k^2 [\cos(\omega_{13} + \omega_{45})\tau + \cos(\omega_{13} - \omega_{45})\tau + \cos(\omega_{12} + \omega_{46})\tau + \cos(\omega_{12} - \omega_{46})\tau \\ + \cos(\omega_{23} + \omega_{46})\tau + \cos(\omega_{23} - \omega_{46})\tau + \cos(\omega_{13} + \omega_{56})\tau + \cos(\omega_{13} - \omega_{56})\tau] \end{aligned}$$

Three – pulse ESEEM $S = \frac{1}{2}, I = 1$

$$\begin{aligned}
E_{\text{mod}}(\tau, T) = & \left(1 - \frac{4}{3}k + \frac{3}{4}k^2\right) + \left(\frac{1}{3}k - \frac{1}{4}k^2\right) \left[\cos\omega_{12}\tau + \cos\omega_{23}\tau + \cos\omega_{45}\tau + \cos\omega_{56}\tau + \cos\omega_{12}(\tau + T) \right. \\
& \left. + \cos\omega_{23}(\tau + T) + \cos\omega_{45}(\tau + T) + \cos\omega_{56}(\tau + T) \right] \\
& - \frac{1}{6} \left(k + k\sqrt{1-k} - k^2\right) \left[\cos\omega_{12}\tau \cos\omega_{45}(\tau + T) + \cos\omega_{23}\tau \cos\omega_{56}(\tau + T) \right. \\
& \left. + \cos\omega_{45}\tau \cos\omega_{12}(\tau + T) + \cos\omega_{56}\tau \cos\omega_{23}(\tau + T) \right] \\
& - \frac{1}{6} \left(k - k\sqrt{1-k} - k^2\right) \left[\cos\omega_{12}\tau \cos\omega_{56}(\tau + T) + \cos\omega_{23}\tau \cos\omega_{45}(\tau + T) \right. \\
& \left. + \cos\omega_{45}\tau \cos\omega_{23}(\tau + T) + \cos\omega_{56}\tau \cos\omega_{12}(\tau + T) \right] \\
& + \frac{1}{8}k^2 \left[\cos\omega_{13}\tau + \cos\omega_{46}\tau + \cos\omega_{13}(\tau + T) + \cos\omega_{46}(\tau + T) \right] \\
& + \frac{1}{24}k^2 \left[\cos\omega_{13}\tau \cos\omega_{46}(\tau + T) + \cos\omega_{46}\tau \cos\omega_{13}(\tau + T) \right] \\
& - \frac{1}{12}k^2 \left[\cos\omega_{12}\tau \cos\omega_{46}(\tau + T) + \cos\omega_{46}\tau \cos\omega_{12}(\tau + T) + \cos\omega_{23}\tau \cos\omega_{46}(\tau + T) \right. \\
& \left. + \cos\omega_{46}\tau \cos\omega_{23}(\tau + T) + \cos\omega_{45}\tau \cos\omega_{13}(\tau + T) + \cos\omega_{13}\tau \cos\omega_{45}(\tau + T) \right. \\
& \left. + \cos\omega_{56}\tau \cos\omega_{13}(\tau + T) + \cos\omega_{13}\tau \cos\omega_{56}(\tau + T) \right]
\end{aligned}$$

The modulation functions reported for the $S = \frac{1}{2}, I = 1$ system are the ones derived by Mims (equations 53 and 54 of reference [27]) with some minor corrections determined by repeating the calculation as described in chapter 5.

In the case of the two-pulse ESEEM experiment, the expression of the echo modulation derived for $I=1$ still contains the nuclear frequencies as well as their sums and differences. This expression is complicated by the appearance of terms multiplied by higher order powers of the modulation depth parameter k . If the quadrupole interaction is not taken into account and if all terms with powers of k higher than one are neglected the expression reduces to:

$$E_{\text{mod}}(\tau) = 1 - \frac{16}{3}k \sin^2\left(\frac{\omega_{\alpha}\tau}{2}\right) \sin^2\left(\frac{\omega_{\beta}\tau}{2}\right)$$

The second approximation is reasonable since k is typically small, as can be inferred from its definition. This simplified expression is similar to the one obtained for the $S = \frac{1}{2}, I = \frac{1}{2}$ spin system, but the modulation depth is $\frac{8}{3}$ times greater. This is in line with the demonstration that, in the assumption of weak electron-nuclear coupling and of negligible quadrupole interactions, the modulation depth is proportional to $I(I+1)$ [35]. In consequence exchanging protons with

deuterons leads to an increase in the modulation depth for the basic nuclear frequencies by a factor of $\frac{8}{3}$.

The three-pulse ESEEM formula shows only modulation at the nuclear frequencies, as already observed previously. The dependence of the modulation amplitudes on τ again leads to the suppression effect.

4.4 ESEEM FOR A $S = 1, I = 1/2$ SYSTEM

In triplet state systems the ZFS interaction has to be included in the spin Hamiltonian. Hence the spin Hamiltonian describing a $S = 1, I = \frac{1}{2}$ system is [36]:

$$\hat{H}_0 = \omega_S S_z + D \left(\hat{S}_z^2 - \frac{1}{3} \hat{S}^2 \right) + E \left(\hat{S}_x^2 - \hat{S}_y^2 \right) - \omega_I I_z + \hat{S} A \hat{I}$$

The Hamiltonian can be partitioned into three sub-Hamiltonians, each corresponding to a different value of the electron spin quantum number m_S , which can then be diagonalized separately following the same procedure as in the $S = \frac{1}{2}, I = \frac{1}{2}$ system described above. The energy level diagram for a $S = 1, I = \frac{1}{2}$ system is reported in Fig. 4.6.

The eigenfrequencies corresponding to the $|T_{+1}\rangle$ and $|T_{-1}\rangle$ states are:

$$\omega_{+1} = \sqrt{(\omega_I - A)^2 + B^2} \qquad \omega_{-1} = \sqrt{(\omega_I + A)^2 + B^2}$$

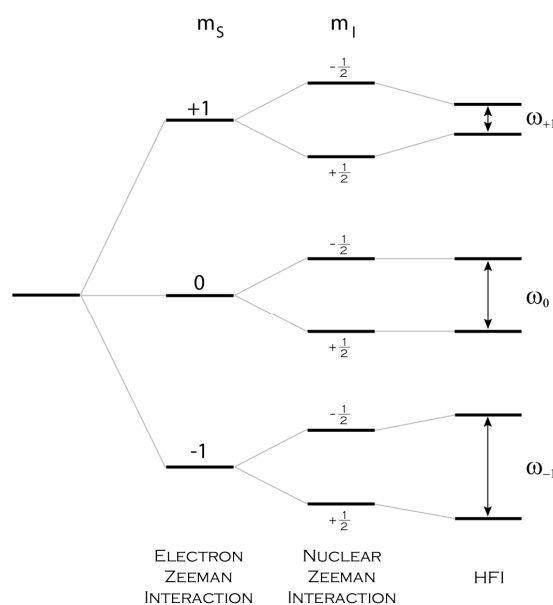


Fig. 4.6 Energy levels and nuclear transition frequencies for a $S = 1, I = \frac{1}{2}$ spin system.

In the $|T_0\rangle$ state there is no contribution of the hyperfine coupling ($S_z=0$) and thus the eigenfrequency is equal to the Larmor frequency of the nucleus.

The overlap matrix M for two electron spin sublevels of the triplet state obtained from the eigenvectors of the nuclear sub-Hamiltonians is:

$$M = \begin{bmatrix} -\sqrt{\frac{1}{2}(1-\sqrt{1-k})} & \sqrt{\frac{1}{2}(1+\sqrt{1-k})} \\ \sqrt{\frac{1}{2}(1+\sqrt{1-k})} & \sqrt{\frac{1}{2}(1-\sqrt{1-k})} \end{bmatrix}$$

where k is equal to k_{+1} for the $|T_{+1}\rangle \leftrightarrow |T_0\rangle$ transition and to k_{-1} for the $|T_{-1}\rangle \leftrightarrow |T_0\rangle$ transition. The modulation depth parameters k_{+1} and k_{-1} are defined below.

In a triplet state system the microwave pulses are usually transition-selective, i.e. only one electron spin transition is excited at a time. The spacing of the triplet state sublevels due to zero-field splitting is generally such that the microwave frequency cannot simultaneously excite transitions that share a common sublevel. The triplet system can be well approximated to a fictitious spin $\frac{1}{2}$ system under the conditions that $g\beta B_1 \ll D$ and that B_0 is aligned along a principal molecular axis [36].

Assuming again that $\hat{H}_0 < \hat{H}_1$, the Hamiltonian \hat{H}_1 is proportional to S_x , which in this case corresponds to:

$$S_x = \begin{matrix} & |T_{+1}\rangle & |T_0\rangle & |T_{-1}\rangle \\ \begin{matrix} |T_{+1}\rangle \\ |T_0\rangle \\ |T_{-1}\rangle \end{matrix} & \begin{bmatrix} 0 & \frac{1}{\sqrt{2}} & 0 \\ \frac{1}{\sqrt{2}} & 0 & \frac{1}{\sqrt{2}} \\ 0 & \frac{1}{\sqrt{2}} & 0 \end{bmatrix} \end{matrix}$$

By comparison with the S_x matrix in the $S = \frac{1}{2}$ state, it can be noted that an effective rotation for an $S=1$ system is $\sqrt{2}$ times that for an $S = \frac{1}{2}$ system [36].

The selective excitation of a single electron transition is expressed mathematically by considering only those elements of the S_x matrix which connect the electron spin states involved in the transition and by setting all other terms equal to zero. The nutation matrix for the $|T_{+1}\rangle \leftrightarrow |T_0\rangle$ transition, obtained after transforming the modified S_x matrix into the eigenbasis of the complete spin Hamiltonian, is:

$$R_N = \begin{bmatrix} \cos\left(\frac{\omega_N t_p}{\sqrt{2}}\right) & iM_{+1}^{\dagger} \sin\left(\frac{\omega_N t_p}{\sqrt{2}}\right) \\ iM_{+1} \sin\left(\frac{\omega_N t_p}{\sqrt{2}}\right) & \cos\left(\frac{\omega_N t_p}{\sqrt{2}}\right) \end{bmatrix}$$

Having thus defined the terms in the general expression for the modulation, the explicit analytical expression for the echo envelope modulation in a two-pulse ESEEM experiment for a $S = 1$, $I = \frac{1}{2}$ system can be calculated and, for the $|T_{+1}\rangle \leftrightarrow |T_0\rangle$ transition, is given by [36]:

$$E_{\text{mod}}(\tau) = 1 - 2k_{+1} \sin^2\left(\frac{\omega_{+1}\tau}{2}\right) \sin^2\left(\frac{\omega_1\tau}{2}\right)$$

where the modulation depth in this case is defined as:

$$k_{+1} = \left(\frac{B}{\omega_{+1}}\right)^2$$

Again the modulation depth depends on the hyperfine parameter B and the same considerations stated above for the $S = \frac{1}{2}$ case also apply here.

An analogous expression, with ω_{+1} substituted by ω_{-1} both in the modulation expression and in the definition of k , is obtained for the $|T_{-1}\rangle \leftrightarrow |T_0\rangle$ transition.

The expression for the echo modulation in a triplet state is the same as the expression derived by Mims for $S = \frac{1}{2}$, except for the different definitions of the nuclear frequencies and of the modulation depth parameter k .

The expression for the echo envelope modulation in a three-pulse ESEEM experiment for the $|T_{+1}\rangle \leftrightarrow |T_0\rangle$ transition in a $S = 1$, $I = \frac{1}{2}$ system is:

$$\begin{aligned} E_{\text{mod}}(\tau, T) &= 1 - \frac{k_{+1}}{2} + \frac{k_{+1}}{4} \left[\cos \omega_{+1}\tau + \cos \omega_0\tau + (1 - \cos \omega_0\tau) \cos \omega_{+1}(\tau + T) + (1 - \cos \omega_{+1}\tau) \cos \omega_0(\tau + T) \right] \\ &= 1 - k_{+1} \left[\sin^2 \frac{\omega_{+1}\tau}{2} \sin^2 \frac{\omega_0(\tau + T)}{2} + \sin^2 \frac{\omega_0\tau}{2} \sin^2 \frac{\omega_{+1}(\tau + T)}{2} \right] \end{aligned}$$

This expression is equal, except for the definition of the frequencies and the modulation depth parameter, to the expression obtained by Mims in the $S = \frac{1}{2}$ case [27] and an analogous expression holds for the other triplet state electron transition.

4.5 ESEEM FOR SEVERAL NUCLEI

In general the electron spins are coupled to more than one nuclear spin and in that case the nuclear Zeeman interaction, the hyperfine interaction and the interaction between nuclear spins in the spin Hamiltonian are summed over all coupled nuclei. The mutual interaction of the nuclear spins is small compared to the interactions between nuclear and electron spins and can thus be neglected. The nuclear sub-Hamiltonians relative to different nuclei can then be diagonalized separately and the density operator can be expressed as a product of operators relative to a particular electron spin–nuclear spin pair. In the two-pulse ESEEM experiment the echo envelope modulation may thus be expressed as [27]:

$$E_{\text{mod}}^N(\tau) = \prod_{k=1}^N E_{\text{mod}}^k(\tau)$$

where E_{mod}^k is the modulation function for a single nuclear spin k . This so-called product rule holds both for identical and non-identical nuclei.

In the three-pulse ESEEM experiment the product rule is slightly different and has the following form [37]:

$$E_{\text{mod}}^N(\tau, T) = \frac{1}{2} \left[\prod_{k=1}^N E_{\text{mod}}^{k,\alpha}(\tau, T) + \prod_{k=1}^N E_{\text{mod}}^{k,\beta}(\tau, T) \right]$$

where $E_{\text{mod}}^{k,\alpha}$ and $E_{\text{mod}}^{k,\beta}$ contain only terms of the type $\cos\omega_\alpha(\tau+T)$ and $\cos\omega_\beta(\tau+T)$ respectively. In the limit of very weak hyperfine interaction the two terms are almost equal and the product rule assumes a similar form as in the two-pulse experiment.

In consequence of the product rule, the echo envelope is modulated also by combinations of frequencies relative to different nuclei. Due to the different form of the product rule for three-pulse ESEEM, in that experiment only combinations of nuclear frequencies belonging to the same electron spin manifold are present.

4.6 ESEEM IN ORIENTATIONALY DISORDERED SYSTEMS

The preceding treatment was referred to spin systems with a single definite orientation with respect to the applied magnetic field, as is the case in single crystals. In disordered samples, such as powders, frozen solutions and glasses, the spin system can assume several different orientations with respect to the external magnetic field. The echo envelope modulation pattern is then computed by averaging over all orientations of the spin system with respect to the external

field. This is achieved by integrating the echo modulation, which depends on the orientation of the spin system with respect to the magnetic field B_0 , over a sphere [28]:

$$\langle E_{\text{mod}} \rangle_{\theta, \varphi} = \frac{1}{4\pi} \int_0^\pi \int_0^{2\pi} E_{\text{mod}}(\theta, \varphi) \sin \theta \, d\theta \, d\varphi$$

where the angles θ and φ define the orientation of the hyperfine tensor with respect to the external magnetic field.

The powder average leads to an attenuation of the modulation frequencies along the time scale. The damping of the modulation is different for different frequency contributions and depends on the strength of the hyperfine interaction and, where present, on the nuclear quadrupole interaction [28]. The stronger is the hyperfine interaction, the faster is the damping of the corresponding nuclear frequencies. Thus at longer times the modulation frequencies of weakly coupled nuclei prevail, as the contribution of the stronger coupled nuclei has decayed.

So far it has been assumed that all the possible orientations in a disordered sample contribute equally to the modulation of the echo envelope. While this is true in general, there are cases in which only some orientations of the spin system contribute to the signal and this is referred to as orientation selection [25]. Orientation selection occurs in systems with an anisotropic contribution to the electron spin Hamiltonian \hat{H}_s , which can be an anisotropic g tensor, a ZFS interaction or a strong hyperfine interaction. The microwave frequency is then resonant with transitions between electron spin states only for certain orientations of the spin system with respect to the external field and only these orientations contribute to the signal. In Fig. 4.7 the different orientations contributing to a triplet state powder spectrum at the canonical values of the magnetic field are represented as shades on a unit sphere. In a triplet state the orientation selection is due to the ZFS interaction.

The ESEEM collected at a particular magnetic field, usually at the canonical orientations of the electron Zeeman or ZFS interaction, is representative of a certain subset of orientations of the spin system with respect to the external field. The selected orientations can be computed from the exact form of the electron spin Hamiltonian \hat{H}_s , and only the corresponding ESEEM signals are considered in performing the powder average. For example for the system in Fig. 4.7, the ESEEM signal at one of the reported field positions would be calculated by computing the echo modulation only for the selected orientations, represented as darker shades on the sphere, and by performing a weighted sum.

The ESEEM at a particular value of the magnetic field is sensitive to the relative orientation between the interaction tensors of the spin system. Thus orientation selection is a useful tool for

determining for example the orientation of the hyperfine tensor with respect to the tensor producing the orientation distribution.

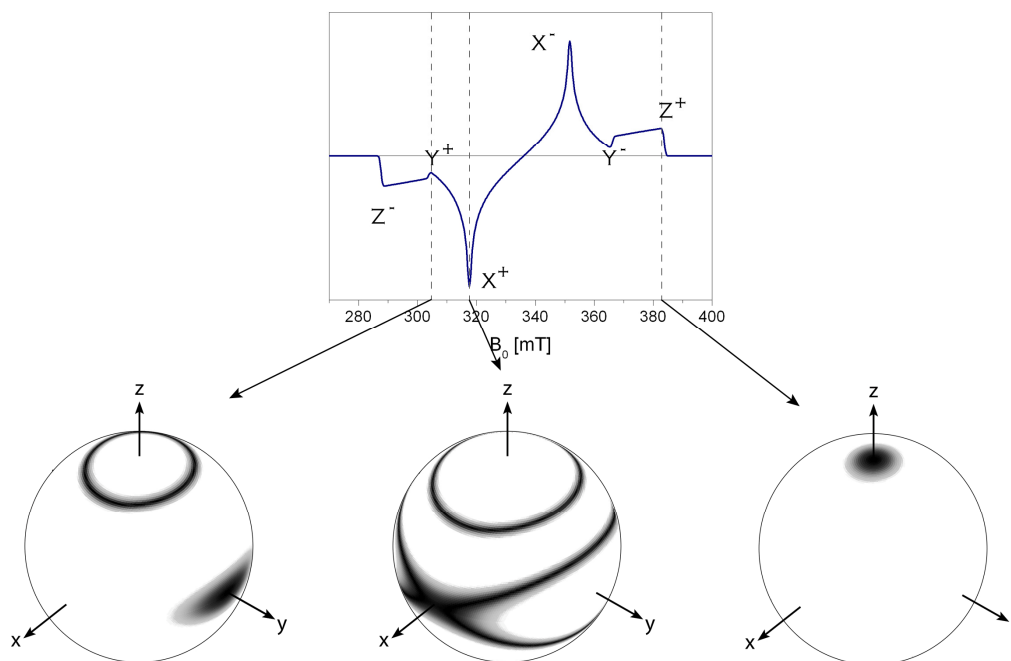


Fig. 4.7 Calculated powder EPR spectrum for a triplet state with $D, E < 0$ and $P_y > P_x > P_z$. The weights of the orientations contributing to the spectrum at the canonical positions Y^+ , X^+ and Z^+ are plotted on a unit sphere, darker shades correspond to higher weights, the white areas indicate the orientations not contributing at that field position.

4.7 HYSORE

4.7.1 HYSORE FOR $S = 1/2$, $I = 1/2$ AND $I = 1$ SYSTEMS

The expression for the modulation of the echo intensity as a function of τ , t_1 and t_2 in the HYSORE experiment can be derived using the density matrix treatment described above. The modulation formula for the $S = 1/2$, $I = 1/2$ system has been first derived by Gemperle *et al.* [38] and has later been revised and corrected by Tyryshkin *et al.* [39]. It is usually written as a sum of two contributions to emphasize the different evolution pathways of the nuclear spins: $E_{\text{mod}}^{\alpha\beta}$ describes the nuclear spins precessing with the frequencies of the α manifold during t_1 and of the β manifold during t_2 ; $E_{\text{mod}}^{\beta\alpha}$ describes the nuclear spins precessing with the frequencies of the β manifold during t_1 and of the α manifold during t_2 .

The modulation formula for a $S = \frac{1}{2}$, $I = \frac{1}{2}$ system is:

$$E_{\text{mod}}(\tau, t_1, t_2) = \frac{1}{2} \left[E_{\text{mod}}^{\alpha\beta}(\tau, t_1, t_2) + E_{\text{mod}}^{\beta\alpha}(\tau, t_1, t_2) \right]$$

$$E_{\text{mod}}^{\alpha\beta}(\tau, t_1, t_2) = 1 - k \left[\frac{C_0}{4} + \frac{C_\alpha}{2} \cos\left(\omega_\alpha t_1 + \frac{\omega_\alpha \tau}{2}\right) + \frac{C_\beta}{2} \cos\left(\omega_\beta t_2 + \frac{\omega_\beta \tau}{2}\right) + \frac{C_c}{2} \left\{ c^2 \cos\left(\omega_\alpha t_1 + \omega_\beta t_2 + \frac{\omega_+ \tau}{2}\right) - s^2 \cos\left(\omega_\alpha t_1 - \omega_\beta t_2 + \frac{\omega_- \tau}{2}\right) \right\} \right]$$

$$E_{\text{mod}}^{\beta\alpha}(\tau, t_1, t_2) = 1 - k \left[\frac{C_0}{4} + \frac{C_\alpha}{2} \cos\left(\omega_\alpha t_2 + \frac{\omega_\alpha \tau}{2}\right) + \frac{C_\beta}{2} \cos\left(\omega_\beta t_1 + \frac{\omega_\beta \tau}{2}\right) + \frac{C_c}{2} \left\{ c^2 \cos\left(\omega_\alpha t_2 + \omega_\beta t_1 + \frac{\omega_+ \tau}{2}\right) - s^2 \cos\left(\omega_\alpha t_2 - \omega_\beta t_1 + \frac{\omega_- \tau}{2}\right) \right\} \right]$$

$$C_0 = 3 - \cos\omega_\alpha \tau - \cos\omega_\beta \tau - s^2 \cos\omega_+ \tau - c^2 \cos\omega_- \tau$$

$$C_\alpha = c^2 \cos\left(\omega_\beta \tau - \frac{\omega_\alpha \tau}{2}\right) + s^2 \cos\left(\omega_\beta \tau + \frac{\omega_\alpha \tau}{2}\right) - \cos\left(\frac{\omega_\alpha \tau}{2}\right)$$

$$C_\beta = c^2 \cos\left(\omega_\alpha \tau - \frac{\omega_\beta \tau}{2}\right) + s^2 \cos\left(\omega_\alpha \tau + \frac{\omega_\beta \tau}{2}\right) - \cos\left(\frac{\omega_\beta \tau}{2}\right)$$

$$C_c = -2 \sin\left(\frac{\omega_\alpha \tau}{2}\right) \sin\left(\frac{\omega_\beta \tau}{2}\right)$$

$$c^2 = \frac{1}{2}(1 + \sqrt{1-k}) \quad s^2 = \frac{1}{2}(1 - \sqrt{1-k})$$

The different terms of the echo envelope modulation expression represent different contributions to the signal and thus to the HYSORE spectrum obtained after 2D Fourier transform along the time dimensions t_1 and t_2 :

- C_0 denotes the un-modulated part of the signal, as it does not depend on t_1 and t_2 .
- The terms proportional to C_α and C_β depend on either t_1 or t_2 and after Fourier transform give rise to axial peaks at $(\omega_\alpha, 0)$, $(\omega_\beta, 0)$, $(0, \omega_\alpha)$ and $(0, \omega_\beta)$.
- The terms proportional to C_c depend on both t_1 and t_2 and give rise to cross peaks in the HYSORE spectrum at $(\omega_\alpha, \omega_\beta)$, $(\omega_\beta, \omega_\alpha)$, $(\omega_\alpha, -\omega_\beta)$ and $(\omega_\beta, -\omega_\alpha)$.

In the last contribution two types of terms with different weighting factors, c^2 and s^2 , can be distinguished, which give rise to cross peaks in different quadrants of the HYSORE spectrum. The weighting factors c^2 and s^2 depend on the strength of the hyperfine interaction and it can be demonstrated that in the limit of weak hyperfine coupling $c^2 \approx 1$ and $s^2 \approx 0$, while in the limit of strong coupling $c^2 \approx 0$ and $s^2 \approx 1$ [32]. Thus strongly and weakly coupled nuclei can be discriminated easily because the cross peaks relative to nuclei with large hyperfine interaction

appear in the upper left quadrant, while the cross peaks relative to nuclei with small hyperfine interaction appear in the upper right quadrant. In Fig. 4.8 the possible peaks in the HYSORE spectrum along with the terms which originate them are represented.

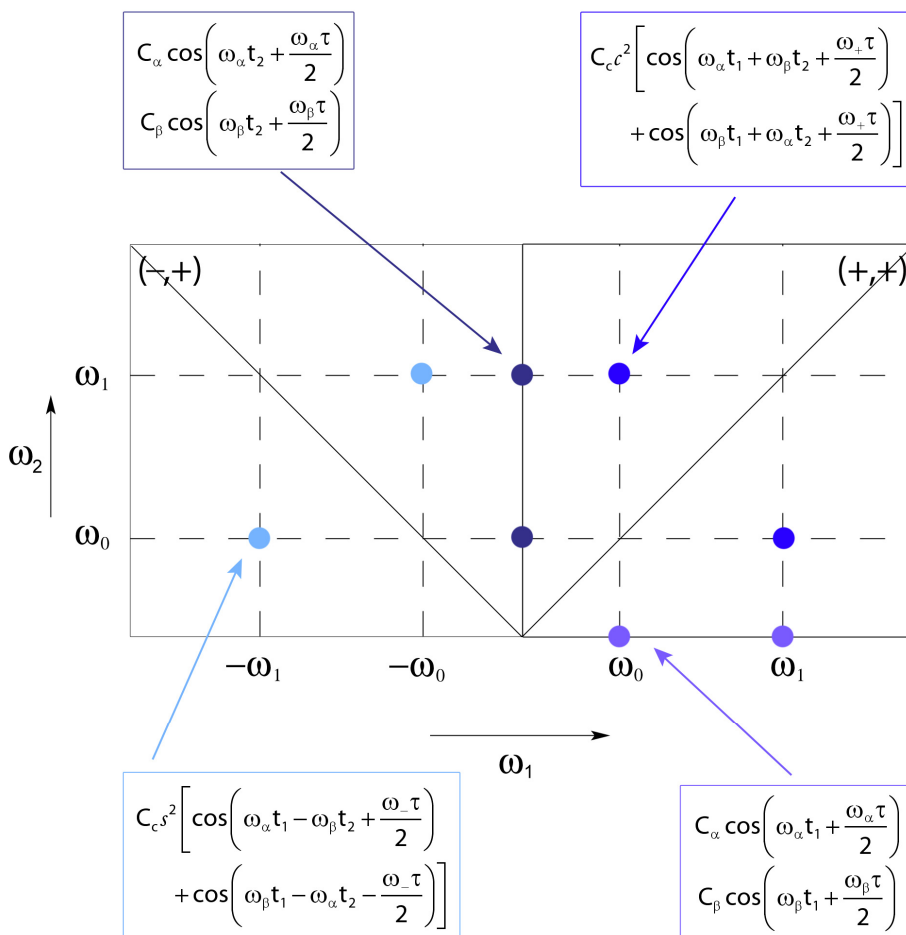


Fig. 4.8 Schematic plot of the different types of peaks in the upper quadrants of a HYSORE spectrum and terms in the modulation formula that describe them.

In systems with $I > \frac{1}{2}$ cross peaks arise between any nuclear frequencies in different electron manifolds. The HYSORE spectra for these systems are further complicated by the influence of the nuclear quadrupole interaction, present for this type of nuclei.

For the $S = \frac{1}{2}$, $I = 1$ system the complete normalized analytical expression for the spin echo envelope modulation in the HYSORE experiment is not reported in the literature, however Tyryshkin *et al.* [39] published the expression for the 1D four-pulse ESEEM sequence (HYSORE with $t_1 = t_2 = T$) and, based on that formula, Pöpl *et al.* [40] derived the expression for the 2D experiment, however retaining only the terms giving rise to cross peaks.

The product rule for the HYSORE experiment is analogous to the one for the three-pulse ESEEM experiment, the modulation formula in the presence of N nuclei may be expressed as:

$$E_{\text{mod}}^N(\tau, t_1, t_2) = \frac{1}{2} \left[\prod_{k=1}^N E_{\text{mod}}^{k,\alpha\beta}(\tau, t_1, t_2) + \prod_{k=1}^N E_{\text{mod}}^{k,\beta\alpha}(\tau, t_1, t_2) \right]$$

In the presence of more than one nucleus, combinations of nuclear frequencies of different nuclei can occur, but like in the three-pulse experiment only between nuclear frequencies of the same electron spin manifold.

The dependence of the modulation amplitudes on τ leads to blind spots in the HYSORE spectrum. In order to avoid suppression holes in the frequency region of interest the parameter τ needs to be adjusted [41].

4.7.2 CORRELATION PATTERNS FOR DISORDERED SYSTEMS

In disordered systems the anisotropy of the interactions results in a spread of nuclear frequencies, which leads to the appearance of correlation patterns in the HYSORE spectrum. In the contour plot of the HYSORE spectrum so called cross peak ridges appear, whose position and shape depend on the interactions within the studied spin system. The correlation patterns relative to different nuclei are centred on the corresponding nuclear Larmor frequency.

In proton HYSORE spectra ($I = \frac{1}{2}$) the shape of the correlation ridges is determined solely by the hyperfine interaction. The anisotropic hyperfine interaction leads to arc-shaped ridges, that are perpendicular to the diagonal ($\omega_1 = \omega_2$) in the weak coupling limit, as illustrated in the simulation in Fig. 4.9. The strength of the isotropic hyperfine coupling determines the distance between the centres of the two ridges and the strength of the dipolar hyperfine interaction determines their curvature. The correlation patterns for an axial hyperfine tensor can be calculated and the hyperfine interaction parameters a_{iso} and T can be directly determined from the spectrum [42]. In more general cases the hyperfine interaction parameters are determined through simulation of the experimentally observed correlation patterns.

In deuterium HYSORE spectra ($I=1$), both the hyperfine and the nuclear quadrupole interaction contribute to the appearance of the correlation patterns. In addition to the cross peak ridges perpendicular to the frequency diagonal due to the hyperfine interaction, the nuclear quadrupole interaction causes a splitting of the cross peaks parallel to the diagonal, as depicted in the calculated HYSORE spectra in Fig. 4.9. The hyperfine and nuclear quadrupole interactions are thus partially separated in the HYSORE spectrum, allowing the determination of the magnitude of the HFI and NQI tensors and their relative orientation [40].

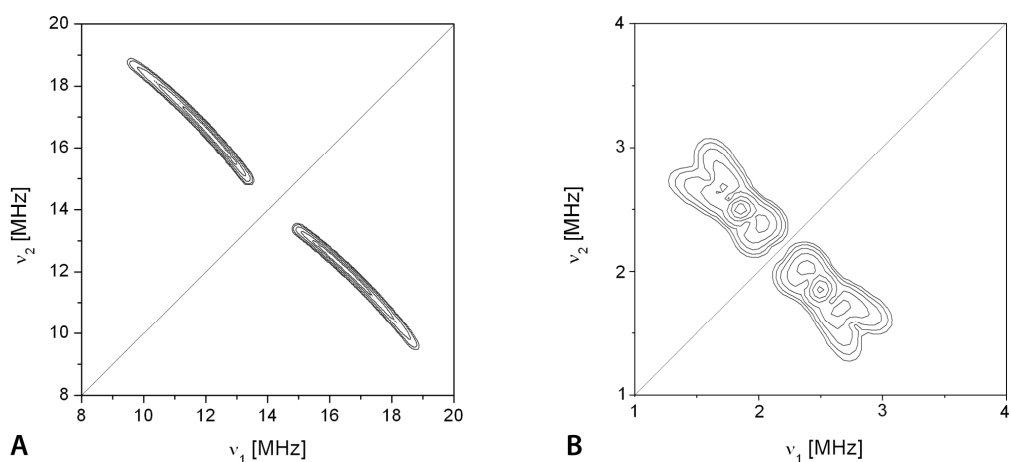
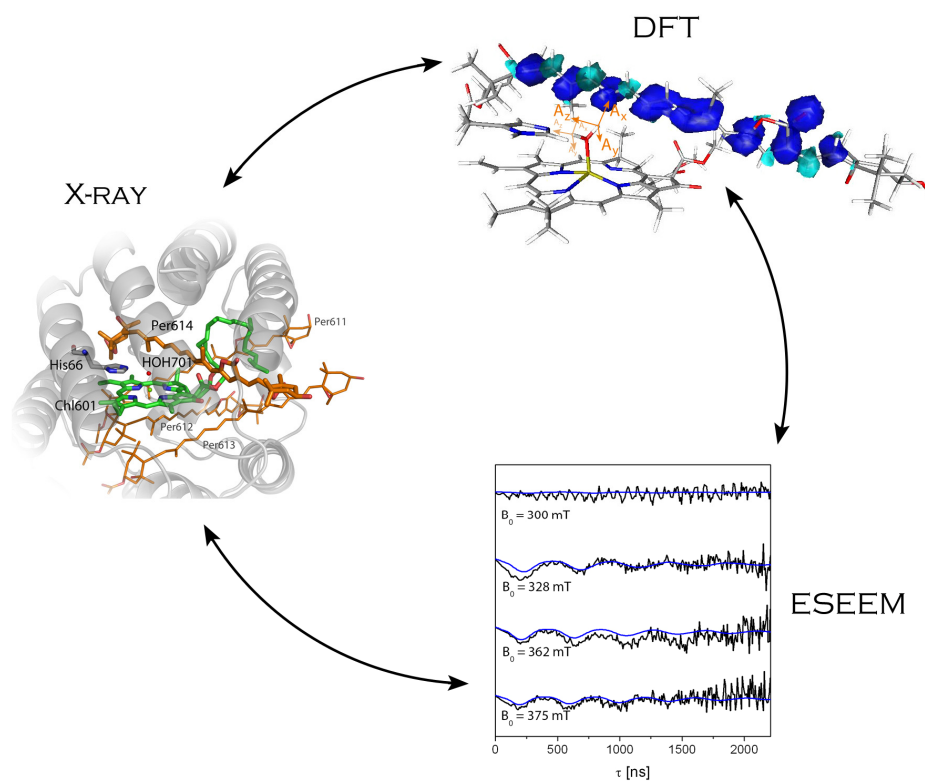


Fig. 4.9 Calculated proton (A) and deuterium (B) powder HYSORE spectra for weak hyperfine interactions and a nuclear quadrupole interaction in the case of deuterium.

The HYSORE correlation patterns can differ for different magnetic field positions in systems with strong anisotropic interactions involving the electron spin, such as for example an anisotropic g tensor or a ZFS tensor in a triplet state. In this case, orientation selective HYSORE experiments can be performed and additional information on the relative orientation of the hyperfine and nuclear quadrupole tensor with respect to the g or ZFS tensor can be obtained [43].

II

EXPERIMENTAL SECTION



CHAPTER 5

ESEEM FORMULAE FOR TRIPLET STATE SYSTEMS

The system under investigation in the present work is a triplet state ($S=1$) coupled to hydrogen ($I = \frac{1}{2}$) or to deuterium ($I=1$) nuclei and the explicit analytical expressions for the echo modulation of these systems in the two-pulse, three-pulse and HYSORE experiment were derived in the course of the present work.

The explicit analytical expressions for the echo modulation in a number of systems and for different pulse sequences have been derived with the density matrix formalism of Mims [27] and published in the literature. Specifically, analytical expressions for two-pulse and three-pulse ESEEM and HYSORE have been derived for $S = \frac{1}{2}$, $I = \frac{1}{2}$ and $I=1$ systems [27,38,40]. A method for deriving the explicit analytical expressions for the echo modulation of a $S = \frac{1}{2}$ system coupled to an arbitrary nuclear spin, in cases of negligible nuclear quadrupole interaction, has also been proposed [35,44].

As far as $S > \frac{1}{2}$ spin systems are concerned, expressions for the echo modulation in the two-pulse ESEEM experiment have been derived for $S = 1$, $I = \frac{1}{2}$ systems [36] and the $S = \frac{5}{2}$ case (Mn^{2+} complexes) has been analyzed in some detail [45-47].

Although numerical simulation of ESEEM time and frequency domain data for any system is possible using the *Easyspin* routine in Matlab® [48], the explicit analytical expressions are useful for an analysis of the effect of various parameters on the echo modulation.

5.1 METHOD

The explicit analytical expressions for the ESEEM signal in the time domain were derived

following the density matrix treatment proposed by Mims. The derivation procedure, as reported in reference [27] and outlined in chapter 4, was implemented in Mathematica® for the $S=1, I=1$ system under study and for the different pulse sequences. The output was simplified through algebraic transformations in order to obtain the final expressions.

5.2 TWO- AND THREE-PULSE ESEEM FOR $S=1, I=1$ SYSTEMS

ESEEM spectroscopy on triplet states is transition selective, i.e. the microwave pulse cannot simultaneously excite different transitions sharing a common level. The $|T_{+1}\rangle \leftrightarrow |T_0\rangle$ and the $|T_{-1}\rangle \leftrightarrow |T_0\rangle$ transitions can thus be considered separately and the triplet state can be treated as a fictitious $S = \frac{1}{2}$ system.

As already explained in chapter 4, in the case of $I=1$ nuclei the nuclear quadrupole interaction contributes to the nuclear modulation effects next to the nuclear Zeeman and the hyperfine interaction. The energy levels of a $S=1$ system coupled to a nucleus with spin $I=1$ are depicted in Fig. 5.1.

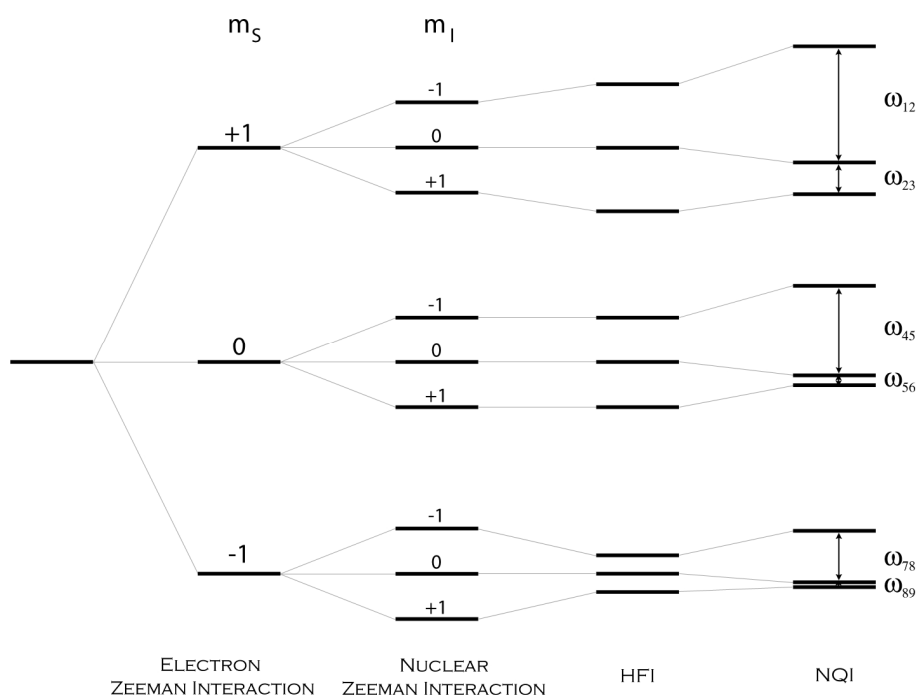


Fig. 5.1 Energy levels and nuclear transition frequencies for a $S=1, I=1$ spin system in the limit of nuclear Zeeman interaction > hyperfine interaction > nuclear quadrupole interaction.

The nuclear quadrupole interaction is taken into account as a first-order correction of the nuclear frequencies, which are determined by diagonalization of the nuclear spin Hamiltonian comprising only the nuclear Zeeman and the hyperfine interaction:

$$\begin{aligned}
 & S = 1, \quad I = 1 \\
 \omega_{+1} &= \sqrt{(\omega_1 - A)^2 + B^2} & \omega_0 &= \omega_1 & \omega_{-1} &= \sqrt{(\omega_1 + A)^2 + B^2} \\
 \omega_{12} &= \omega_{+1} + \Delta_{+1} & \omega_{23} &= \omega_{+1} - \Delta_{+1} \\
 \omega_{45} &= \omega_0 + \Delta_0 & \omega_{56} &= \omega_0 - \Delta_0 \\
 \omega_{78} &= \omega_{-1} + \Delta_{-1} & \omega_{89} &= \omega_{-1} - \Delta_{-1}
 \end{aligned}$$

where the first-order correction is the same as defined in chapter 5.

The overlap matrix calculated neglecting the nuclear quadrupole interaction is:

$$M = \begin{bmatrix} -\frac{1}{2}(\sqrt{1-k} + 1) & \frac{1}{\sqrt{2}}\sqrt{k} & \frac{1}{2}(\sqrt{1-k} - 1) \\ \frac{1}{\sqrt{2}}\sqrt{k} & \sqrt{1-k} & -\frac{1}{\sqrt{2}}\sqrt{k} \\ \frac{1}{2}(\sqrt{1-k} - 1) & -\frac{1}{\sqrt{2}}\sqrt{k} & -\frac{1}{2}(\sqrt{1-k} + 1) \end{bmatrix}$$

where k is the modulation depth parameter corresponding to the considered electron spin transition of the triplet state.

Based on the first-order corrected eigenfrequencies and on the overlap matrix defined above, the expression of the echo modulation can be derived. The normalized envelope modulation functions for a specific electron spin transition of the triplet state in the two- and three-pulse ESEEM experiments are:

$$\text{Two-pulse ESEEM} \quad S = 1, \quad I = 1 \quad |T_{+1}\rangle \leftrightarrow |T_0\rangle$$

$$\begin{aligned}
 E_{\text{mod}}(\tau) &= \left(1 - \frac{4}{3}k_{+1} + \frac{3}{4}k_{+1}^2\right) + \left(\frac{2}{3}k_{+1} - \frac{1}{2}k_{+1}^2\right) [\cos\omega_{12}\tau + \cos\omega_{23}\tau + \cos\omega_{45}\tau + \cos\omega_{56}\tau] \\
 &\quad - \left(\frac{1}{6}k_{+1} + \frac{1}{6}k_{+1}\sqrt{1-k_{+1}} - \frac{1}{6}k_{+1}^2\right) [\cos(\omega_{12} + \omega_{45})\tau + \cos(\omega_{12} - \omega_{45})\tau + \cos(\omega_{23} + \omega_{56})\tau + \cos(\omega_{23} - \omega_{56})\tau] \\
 &\quad - \left(\frac{1}{6}k_{+1} - \frac{1}{6}k_{+1}\sqrt{1-k_{+1}} - \frac{1}{6}k_{+1}^2\right) [\cos(\omega_{23} + \omega_{45})\tau + \cos(\omega_{23} - \omega_{45})\tau + \cos(\omega_{12} + \omega_{56})\tau + \cos(\omega_{12} - \omega_{56})\tau] \\
 &\quad + \frac{1}{4}k_{+1}^2 [\cos\omega_{13}\tau + \cos\omega_{46}\tau] + \frac{1}{24}k_{+1}^2 [\cos(\omega_{13} + \omega_{46})\tau + \cos(\omega_{13} - \omega_{46})\tau] \\
 &\quad - \frac{1}{12}k_{+1}^2 [\cos(\omega_{13} + \omega_{45})\tau + \cos(\omega_{13} - \omega_{45})\tau + \cos(\omega_{12} + \omega_{46})\tau + \cos(\omega_{12} - \omega_{46})\tau \\
 &\quad \quad + \cos(\omega_{23} + \omega_{46})\tau + \cos(\omega_{23} - \omega_{46})\tau + \cos(\omega_{13} + \omega_{56})\tau + \cos(\omega_{13} - \omega_{56})\tau]
 \end{aligned}$$

Three – pulse ESEEM $S = 1, I = 1$ $|T_{+1}\rangle \leftrightarrow |T_0\rangle$

$$\begin{aligned}
 E_{\text{mod}}(\tau, T) = & \left(1 - \frac{4}{3}k_{+1} + \frac{3}{4}k_{+1}^2\right) \\
 & + \left(\frac{1}{3}k_{+1} - \frac{1}{4}k_{+1}^2\right) \left[\cos \omega_{12}\tau + \cos \omega_{23}\tau + \cos \omega_{45}\tau + \cos \omega_{56}\tau + \cos \omega_{12}(\tau + T) \right. \\
 & \quad \left. + \cos \omega_{23}(\tau + T) + \cos \omega_{45}(\tau + T) + \cos \omega_{56}(\tau + T) \right] \\
 & - \frac{1}{6}(k_{+1} + k_{+1}\sqrt{1-k_{+1}} - k_{+1}^2) \left[\cos \omega_{12}\tau \cos \omega_{45}(\tau + T) + \cos \omega_{23}\tau \cos \omega_{56}(\tau + T) \right. \\
 & \quad \left. + \cos \omega_{45}\tau \cos \omega_{12}(\tau + T) + \cos \omega_{56}\tau \cos \omega_{23}(\tau + T) \right] \\
 & - \frac{1}{6}(k_{+1} - k_{+1}\sqrt{1-k_{+1}} - k_{+1}^2) \left[\cos \omega_{12}\tau \cos \omega_{56}(\tau + T) + \cos \omega_{23}\tau \cos \omega_{45}(\tau + T) \right. \\
 & \quad \left. + \cos \omega_{45}\tau \cos \omega_{23}(\tau + T) + \cos \omega_{56}\tau \cos \omega_{12}(\tau + T) \right] \\
 & + \frac{1}{8}k_{+1}^2 \left[\cos \omega_{13}\tau + \cos \omega_{46}\tau + \cos \omega_{13}(\tau + T) + \cos \omega_{46}(\tau + T) \right] \\
 & + \frac{1}{24}k_{+1}^2 \left[\cos \omega_{13}\tau \cos \omega_{46}(\tau + T) + \cos \omega_{46}\tau \cos \omega_{13}(\tau + T) \right] \\
 & - \frac{1}{12}k_{+1}^2 \left[\cos \omega_{12}\tau \cos \omega_{46}(\tau + T) + \cos \omega_{46}\tau \cos \omega_{12}(\tau + T) + \cos \omega_{23}\tau \cos \omega_{46}(\tau + T) \right. \\
 & \quad \left. + \cos \omega_{46}\tau \cos \omega_{23}(\tau + T) + \cos \omega_{45}\tau \cos \omega_{13}(\tau + T) + \cos \omega_{13}\tau \cos \omega_{45}(\tau + T) \right. \\
 & \quad \left. + \cos \omega_{56}\tau \cos \omega_{13}(\tau + T) + \cos \omega_{13}\tau \cos \omega_{56}(\tau + T) \right]
 \end{aligned}$$

The modulation depth parameter k_{+1} for the $|T_{+1}\rangle \leftrightarrow |T_0\rangle$ transition is defined as:

$$k_{+1} = \left(\frac{B}{\omega_{+1}} \right)^2$$

The obtained expressions are of the same form as the ones for the $S = \frac{1}{2}, I = 1$ system, the difference lies in the definition of the nuclear frequencies, obtained by diagonalization of the spin Hamiltonian for the $S = 1, I = 1$ system, and of the modulation depth parameter.

Analogous expressions are obtained for the other electron spin transition of the triplet state. The modulation depth parameter differs for the two different transitions, since it depends on the nuclear frequencies of the manifolds connected by the transitions.

The same considerations mentioned in the preceding chapter also apply to the two- and three-pulse ESEEM of the triplet state coupled to a nucleus with $I = 1$. It is evident from the expression of the two-pulse ESEEM experiment, that the spin echo envelope is modulated by the nuclear frequencies themselves as well as by their sums and differences. The three-pulse ESEEM expression however contains just the nuclear frequencies. The dependence on τ leads to the

same type of blind-spot behaviour as in the simpler spin systems described in the previous chapter.

5.3 HYSORE FOR TRIPLET STATE SYSTEMS

The HYSORE experiment has not been theoretically described for a triplet state system before; hence the explicit analytical expressions were derived for both the $S = 1, I = \frac{1}{2}$ and the $S = 1, I = 1$ case by using the density matrix formalism proposed by Mims [27].

In the application of the HYSORE pulse sequence to a $S > \frac{1}{2}$ centre, complications arise due to the different nominal pulse angle with respect to the simpler $S = \frac{1}{2}$ case. In a $S > \frac{1}{2}$ system the nominal pulse angle depends on the m_s quantum numbers of the manifolds connected by the selected EPR transition and may in general be different for different electron transitions. In the case of a triplet state system both allowed EPR transitions require the same nominal pulse angle, which differs however from the one of a $S = \frac{1}{2}$ system.

5.3.1 HYSORE FOR A $S = 1, I = 1/2$ SYSTEM

Again the two electron transitions of the triplet state can be treated separately, as they are not simultaneously excited by the microwave pulse. The formula obtained for the $|T_{+1}\rangle \leftrightarrow |T_0\rangle$ transition in a $S = 1, I = \frac{1}{2}$ system is:

$$E_{\text{mod}}(\tau, t_1, t_2) = \frac{1}{2} [E_{\text{mod}}^{\alpha\beta}(\tau, t_1, t_2) + E_{\text{mod}}^{\beta\alpha}(\tau, t_1, t_2)]$$

$$E_{\text{mod}}^{\alpha\beta}(\tau, t_1, t_2) = 1 - \frac{k}{16} \left[C_0 + 4\gamma_+ \cos[\omega_1(t_1 + t_2 + \tau)](\cos \omega_0\tau - 1) + 2\gamma_- \left(C_\alpha \cos\left(\omega_1 t_1 + \frac{\omega_1 \tau}{2}\right) + C_\beta \cos\left(\omega_0 t_2 + \frac{\omega_0 \tau}{2}\right) \right. \right. \\ \left. \left. + C_\epsilon \left\{ (\sqrt{1-k} - 1) \cos\left(\omega_1 t_1 + \omega_0 t_2 + \frac{\omega_+ \tau}{2}\right) + (\sqrt{1-k} + 1) \cos\left(\omega_1 t_1 - \omega_0 t_2 + \frac{\omega_- \tau}{2}\right) \right\} \right) \right]$$

$$E_{\text{mod}}^{\beta\alpha}(\tau, t_1, t_2) = 1 - \frac{k}{16} \left[C_0 + 4\gamma_+ \cos[\omega_0(t_1 + t_2 + \tau)](\cos \omega_1\tau - 1) + 2\gamma_- \left(C_\alpha \cos\left(\omega_1 t_2 + \frac{\omega_1 \tau}{2}\right) + C_\beta \cos\left(\omega_0 t_1 + \frac{\omega_0 \tau}{2}\right) \right. \right. \\ \left. \left. + C_\epsilon \left\{ (\sqrt{1-k} - 1) \cos\left(\omega_1 t_2 + \omega_0 t_1 + \frac{\omega_+ \tau}{2}\right) + (\sqrt{1-k} + 1) \cos\left(\omega_1 t_2 - \omega_0 t_1 + \frac{\omega_- \tau}{2}\right) \right\} \right) \right]$$

$$C_0 = 8 + 2\gamma_- - 4 \cos \omega_1 \tau - 4 \cos \omega_0 \tau - \gamma_- \left[(\sqrt{1-k} + 1) \cos \omega_+ \tau - (\sqrt{1-k} - 1) \cos \omega_- \tau \right]$$

$$C_\alpha = (\sqrt{1-k} + 1) \cos\left(\omega_0 \tau + \frac{\omega_1 \tau}{2}\right) - (\sqrt{1-k} - 1) \cos\left(\omega_0 \tau - \frac{\omega_1 \tau}{2}\right) - 2 \cos\left(\frac{\omega_1 \tau}{2}\right)$$

$$C_{\beta} = (\sqrt{1-k} + 1) \cos\left(\omega_1\tau + \frac{\omega_0\tau}{2}\right) - (\sqrt{1-k} - 1) \cos\left(\omega_1\tau - \frac{\omega_0\tau}{2}\right) - 2 \cos\left(\frac{\omega_0\tau}{2}\right)$$

$$C_c = 2 \sin\left(\frac{\omega_1\tau}{2}\right) \sin\left(\frac{\omega_0\tau}{2}\right)$$

An analogous expression is obtained for the other electron spin transition of the triplet state.

This expression is similar to the one reported for $S = \frac{1}{2}$, $I = \frac{1}{2}$, the main difference is the presence of additional terms of the form $\cos[\omega_1(t_1 + t_2 + \tau)]$, modulated at the same frequency in both dimensions and thus leading to diagonal peaks, and of multiplicative factors γ_+ and γ_- depending on the length of the third pulse t_{pIII} (mixing pulse):

$$\gamma_+ = \left(1 + \frac{1}{\cos\sqrt{2}\omega_N t_{pIII}}\right) \quad \gamma_- = \left(1 - \frac{1}{\cos\sqrt{2}\omega_N t_{pIII}}\right)$$

These differences are due to the different flip angles in an $S=1$ with respect to a $S = \frac{1}{2}$ system. As already mentioned in chapter 4, the effective rotation for an $S=1$ system corresponds to $\sqrt{2}$ times the rotation for a $S = \frac{1}{2}$ system, hence a pulse of the same length as in the $S = \frac{1}{2}$ system does not cause complete inversion with the effect that the intensity of the cross peaks in the spectrum is reduced and that peaks along the diagonal appear (Fig. 5.2).

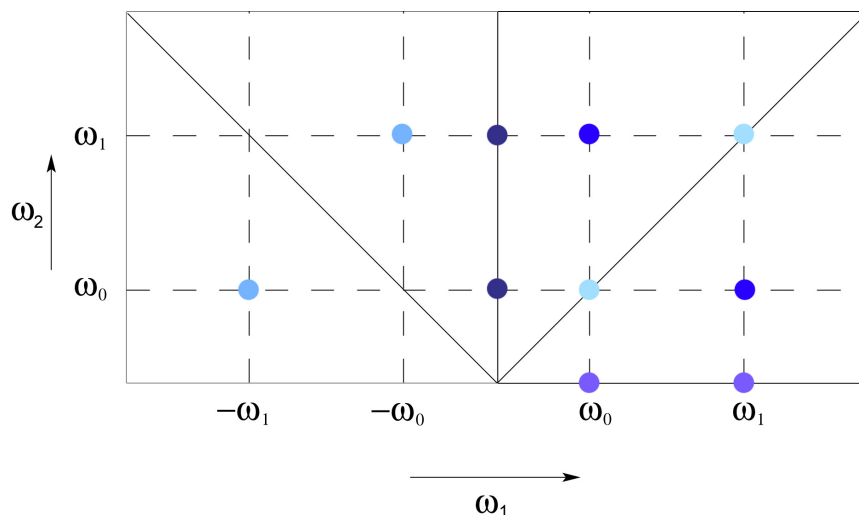


Fig. 5.2 Theoretically possible peaks in the Hyscore spectrum of an $S=1$, $I = \frac{1}{2}$ system. In addition to the axial and cross peaks, diagonal peaks may appear in the case of incomplete inversion by the π pulse.

The application of the density matrix treatment to the Hyscore experiment in an analogous way as for the two- and three-pulse ESEEM experiments leads to the introduction of a dependence of the modulation expression on the length of the inversion π pulse. Experimentally the length of

this pulse can be chosen in order to achieve complete inversion for a particular electron transition. If this is taken into account in the echo modulation expression, the terms giving rise to diagonal peaks vanish and the formula becomes equivalent to the one for the $S = \frac{1}{2}$, $I = \frac{1}{2}$ case reported in chapter 4.

5.3.2 HYSORE FOR A $S=1$, $I=1$ SYSTEM

The HYSORE formula for the $|T_{+1}\rangle \leftrightarrow |T_0\rangle$ transition of a $S=1$, $I=1$ system, derived by taking into account the nuclear quadrupole interaction as a first-order correction to the nuclear frequencies is:

$$E_{\text{mod}}(\tau, t_1, t_2) = \frac{1}{2} \left[E_{\text{mod}}^{\alpha\beta}(\tau, t_1, t_2) + E_{\text{mod}}^{\beta\alpha}(\tau, t_1, t_2) \right]$$

$$E_{\text{mod}}^{\alpha\beta}(\tau, t_1, t_2) = \chi_0 + \chi_d + \gamma_- \left[\chi_{12} \cos\left(\omega_{12}t_1 + \frac{\omega_{12}\tau}{2}\right) + \chi_{23} \cos\left(\omega_{23}t_1 + \frac{\omega_{23}\tau}{2}\right) + \chi_{13} \cos\left(\omega_{13}t_1 + \frac{\omega_{13}\tau}{2}\right) \right. \\ + \chi_{45} \left(\cos\omega_{45}t_2 + \frac{\omega_{45}\tau}{2} \right) + \chi_{56} \left(\cos\omega_{56}t_2 + \frac{\omega_{56}\tau}{2} \right) + \chi_{46} \left(\cos\omega_{46}t_2 + \frac{\omega_{46}\tau}{2} \right) \\ + \chi_{12,45}^+ \left(\cos\omega_{12}t_1 + \omega_{45}t_2 + \frac{(\omega_{12} + \omega_{45})\tau}{2} \right) + \chi_{12,45}^- \left(\cos\omega_{12}t_1 - \omega_{45}t_2 + \frac{(\omega_{12} - \omega_{45})\tau}{2} \right) \\ + \chi_{12,56}^+ \left(\cos\omega_{12}t_1 + \omega_{56}t_2 + \frac{(\omega_{12} + \omega_{56})\tau}{2} \right) + \chi_{12,56}^- \left(\cos\omega_{12}t_1 - \omega_{56}t_2 + \frac{(\omega_{12} - \omega_{56})\tau}{2} \right) \\ + \chi_{12,46}^+ \left(\cos\omega_{12}t_1 + \omega_{46}t_2 + \frac{(\omega_{12} + \omega_{46})\tau}{2} \right) + \chi_{12,46}^- \left(\cos\omega_{12}t_1 - \omega_{46}t_2 + \frac{(\omega_{12} - \omega_{46})\tau}{2} \right) \\ + \chi_{23,45}^+ \left(\cos\omega_{23}t_1 + \omega_{45}t_2 + \frac{(\omega_{23} + \omega_{45})\tau}{2} \right) + \chi_{23,45}^- \left(\cos\omega_{23}t_1 - \omega_{45}t_2 + \frac{(\omega_{23} - \omega_{45})\tau}{2} \right) \\ + \chi_{23,56}^+ \left(\cos\omega_{23}t_1 + \omega_{56}t_2 + \frac{(\omega_{23} + \omega_{56})\tau}{2} \right) + \chi_{23,56}^- \left(\cos\omega_{23}t_1 - \omega_{56}t_2 + \frac{(\omega_{23} - \omega_{56})\tau}{2} \right) \\ + \chi_{23,46}^+ \left(\cos\omega_{23}t_1 + \omega_{46}t_2 + \frac{(\omega_{23} + \omega_{46})\tau}{2} \right) + \chi_{23,46}^- \left(\cos\omega_{23}t_1 - \omega_{46}t_2 + \frac{(\omega_{23} - \omega_{46})\tau}{2} \right) \\ + \chi_{13,45}^+ \left(\cos\omega_{13}t_1 + \omega_{45}t_2 + \frac{(\omega_{13} + \omega_{45})\tau}{2} \right) + \chi_{13,45}^- \left(\cos\omega_{13}t_1 - \omega_{45}t_2 + \frac{(\omega_{13} - \omega_{45})\tau}{2} \right) \\ + \chi_{13,56}^+ \left(\cos\omega_{13}t_1 + \omega_{56}t_2 + \frac{(\omega_{13} + \omega_{56})\tau}{2} \right) + \chi_{13,56}^- \left(\cos\omega_{13}t_1 - \omega_{56}t_2 + \frac{(\omega_{13} - \omega_{56})\tau}{2} \right) \\ \left. + \chi_{13,46}^+ \left(\cos\omega_{13}t_1 + \omega_{46}t_2 + \frac{(\omega_{13} + \omega_{46})\tau}{2} \right) + \chi_{13,46}^- \left(\cos\omega_{13}t_1 - \omega_{46}t_2 + \frac{(\omega_{13} - \omega_{46})\tau}{2} \right) \right]$$

where $E_{\text{mod}}^{\beta\alpha}$ is obtained by exchanging t_1 and t_2 in the expression for $E_{\text{mod}}^{\alpha\beta}$:

$$E_{\text{mod}}^{\beta\alpha}(\tau, t_2, t_1) = E_{\text{mod}}^{\alpha\beta}(\tau, t_1, t_2)$$

The coefficients χ are defined as:

$$\begin{aligned}
 \chi_0 &= 1 - \gamma_+ C_0 - \gamma_- C_1 \\
 &+ (\gamma_+ C_2 + \gamma_- C_3) [\cos \omega_{12} \tau + \cos \omega_{23} \tau + \cos \omega_{45} \tau + \cos \omega_{56} \tau] + (3\gamma_+ C_4 + \gamma_- C_5) [\cos \omega_{13} \tau + \cos \omega_{46} \tau] \\
 &+ \gamma_- [C_6 [\cos(\omega_{12} + \omega_{45}) \tau + \cos(\omega_{23} + \omega_{56}) \tau] + C_7 [\cos(\omega_{12} - \omega_{45}) \tau + \cos(\omega_{23} - \omega_{56}) \tau] \\
 &+ C_8 [\cos(\omega_{12} + \omega_{56}) \tau + \cos(\omega_{23} + \omega_{45}) \tau] + C_9 [\cos(\omega_{12} - \omega_{56}) \tau + \cos(\omega_{23} - \omega_{45}) \tau] \\
 &+ C_{10} [\cos(\omega_{13} + \omega_{45}) \tau + \cos(\omega_{13} + \omega_{56}) \tau + \cos(\omega_{12} + \omega_{46}) \tau + \cos(\omega_{23} + \omega_{46}) \tau] \\
 &+ C_{11} [\cos(\omega_{13} - \omega_{45}) \tau + \cos(\omega_{13} - \omega_{56}) \tau + \cos(\omega_{12} - \omega_{46}) \tau + \cos(\omega_{23} - \omega_{46}) \tau] \\
 &+ C_{12} \cos(\omega_{13} + \omega_{46}) \tau + C_{13} \cos(\omega_{13} - \omega_{46}) \tau] \\
 \chi_d &= \gamma_+ [\cos [\omega_{12} (t_1 + t_2 + \tau)] [C_2 - C_{23} \cos \omega_{45} \tau - C_{24} \cos \omega_{56} \tau - 2C_4 \cos \omega_{46} \tau] \\
 &+ \cos [\omega_{23} (t_1 + t_2 + \tau)] [C_2 - C_{24} \cos \omega_{45} \tau - C_{23} \cos \omega_{56} \tau - 2C_4 \cos \omega_{46} \tau] \\
 &+ \cos [\omega_{13} (t_1 + t_2 + \tau)] [3C_4 - 2C_4 \cos \omega_{45} \tau - 2C_4 \cos \omega_{56} \tau + C_4 \cos \omega_{46} \tau] \\
 &+ \cos [\omega_{45} (t_1 + t_2 + \tau)] [C_2 - C_{23} \cos \omega_{12} \tau - C_{24} \cos \omega_{23} \tau - 2C_4 \cos \omega_{13} \tau] \\
 &+ \cos [\omega_{56} (t_1 + t_2 + \tau)] [C_2 - C_{24} \cos \omega_{12} \tau - C_{23} \cos \omega_{23} \tau - 2C_4 \cos \omega_{13} \tau] \\
 &+ \cos [\omega_{46} (t_1 + t_2 + \tau)] [3C_4 - 2C_4 \cos \omega_{12} \tau - 2C_4 \cos \omega_{23} \tau + C_4 \cos \omega_{13} \tau]] \\
 \chi_{12} &= 2C_3 \cos \frac{\omega_{12} \tau}{2} + C_{14} \cos \left(\frac{\omega_{12} \tau}{2} + \omega_{23} \tau \right) - 4C_{15} \cos \left(\frac{\omega_{12} \tau}{2} + \omega_{45} \tau \right) - C_{16} \cos \left(\frac{\omega_{12} \tau}{2} - \omega_{45} \tau \right) \\
 &- C_{17} \cos \left(\frac{\omega_{12} \tau}{2} + \omega_{56} \tau \right) - 4C_{18} \cos \left(\frac{\omega_{12} \tau}{2} - \omega_{56} \tau \right) - C_{19} \cos \left(\frac{\omega_{12} \tau}{2} + \omega_{46} \tau \right) - C_{20} \cos \left(\frac{\omega_{12} \tau}{2} - \omega_{46} \tau \right) \\
 &+ C_{18} \cos \left(\frac{(\omega_{13} + \omega_{23}) \tau}{2} + \omega_{45} \tau \right) - 2C_{15} \cos \left(\frac{(\omega_{13} + \omega_{23}) \tau}{2} - \omega_{45} \tau \right) - 2C_{18} \cos \left(\frac{(\omega_{13} + \omega_{23}) \tau}{2} + \omega_{56} \tau \right) \\
 &+ C_{15} \cos \left(\frac{(\omega_{13} + \omega_{23}) \tau}{2} - \omega_{56} \tau \right) - 2C_{12} \cos \left(\frac{(\omega_{13} + \omega_{23}) \tau}{2} + \omega_{46} \tau \right) - 2C_{13} \cos \left(\frac{(\omega_{13} + \omega_{23}) \tau}{2} - \omega_{46} \tau \right) \\
 \chi_{13} &= 2C_5 \cos \frac{\omega_{13} \tau}{2} + C_{14} \cos \left(\frac{\omega_{13} \tau}{2} - \omega_{23} \tau \right) - C_{19} \cos \left(\frac{\omega_{13} \tau}{2} + \omega_{45} \tau \right) - C_{20} \cos \left(\frac{\omega_{13} \tau}{2} - \omega_{45} \tau \right) \\
 &- C_{19} \cos \left(\frac{\omega_{13} \tau}{2} + \omega_{56} \tau \right) - C_{20} \cos \left(\frac{\omega_{13} \tau}{2} - \omega_{56} \tau \right) - 2C_{12} \cos \left(\frac{\omega_{13} \tau}{2} + \omega_{46} \tau \right) + 2C_{13} \cos \left(\frac{\omega_{13} \tau}{2} - \omega_{46} \tau \right) \\
 &- 2C_{21} \cos \left(\frac{(\omega_{12} - \omega_{23}) \tau}{2} + \omega_{45} \tau \right) - C_{22} \cos \left(\frac{(\omega_{12} - \omega_{23}) \tau}{2} - \omega_{45} \tau \right) - C_{22} \cos \left(\frac{(\omega_{12} - \omega_{23}) \tau}{2} + \omega_{56} \tau \right) \\
 &- 2C_{21} \cos \left(\frac{(\omega_{12} - \omega_{23}) \tau}{2} - \omega_{56} \tau \right) + C_{21} \cos \left(\frac{(\omega_{12} - \omega_{23}) \tau}{2} + \omega_{46} \tau \right) + C_{21} \cos \left(\frac{(\omega_{12} - \omega_{23}) \tau}{2} - \omega_{46} \tau \right) \\
 \chi_{12,45}^+ &= 2C_7 \cos \left(\frac{(\omega_{12} - \omega_{45}) \tau}{2} \right) - C_{16} \cos \left(\frac{(\omega_{12} + \omega_{45}) \tau}{2} \right) - C_{22} \cos \left(\frac{(\omega_{13} + \omega_{23} + \omega_{45}) \tau}{2} \right) \\
 &+ C_{15} \cos \left(\frac{(\omega_{13} + \omega_{23} - \omega_{45}) \tau}{2} \right) - C_{22} \cos \left(\frac{(\omega_{12} + \omega_{46} + \omega_{56}) \tau}{2} \right) + C_{15} \cos \left(\frac{(\omega_{12} - \omega_{46} - \omega_{56}) \tau}{2} \right) \\
 &+ C_{18} \cos \left(\frac{(\omega_{13} + \omega_{23} + \omega_{46} + \omega_{56}) \tau}{2} \right)
 \end{aligned}$$

$$\begin{aligned}
 \chi_{12,45}^- &= 2C_6 \cos\left(\frac{(\omega_{12} + \omega_{45})\tau}{2}\right) - 4C_{15} \cos\left(\frac{(\omega_{12} - \omega_{45})\tau}{2}\right) - 2C_{18} \cos\left(\frac{(\omega_{13} + \omega_{23} + \omega_{45})\tau}{2}\right) \\
 &\quad - 2C_{21} \cos\left(\frac{(\omega_{13} + \omega_{23} - \omega_{45})\tau}{2}\right) - 2C_{18} \cos\left(\frac{(\omega_{12} + \omega_{46} + \omega_{56})\tau}{2}\right) - 2C_{21} \cos\left(\frac{(\omega_{12} - \omega_{46} - \omega_{56})\tau}{2}\right) \\
 &\quad + 4C_{12} \cos\left(\frac{(\omega_{13} + \omega_{23} + \omega_{46} + \omega_{56})\tau}{2}\right) \\
 \chi_{12,56}^+ &= 2C_9 \cos\left(\frac{(\omega_{12} - \omega_{56})\tau}{2}\right) - 4C_{18} \cos\left(\frac{(\omega_{12} + \omega_{56})\tau}{2}\right) - 2C_{21} \cos\left(\frac{(\omega_{12} + \omega_{46} + \omega_{45})\tau}{2}\right) \\
 &\quad - 2C_{15} \cos\left(\frac{(\omega_{12} - \omega_{46} - \omega_{45})\tau}{2}\right) - 2C_{21} \cos\left(\frac{(\omega_{13} + \omega_{23} + \omega_{56})\tau}{2}\right) - 2C_{15} \cos\left(\frac{(\omega_{13} + \omega_{23} - \omega_{56})\tau}{2}\right) \\
 &\quad + 4C_{13} \cos\left(\frac{(\omega_{13} + \omega_{23} - \omega_{45} - \omega_{46})\tau}{2}\right) \\
 \chi_{12,56}^- &= 2C_8 \cos\left(\frac{(\omega_{12} + \omega_{56})\tau}{2}\right) - C_{17} \cos\left(\frac{(\omega_{12} - \omega_{56})\tau}{2}\right) + C_{18} \cos\left(\frac{(\omega_{12} + \omega_{46} + \omega_{45})\tau}{2}\right) \\
 &\quad - C_{22} \cos\left(\frac{(\omega_{12} - \omega_{46} - \omega_{45})\tau}{2}\right) + C_{18} \cos\left(\frac{(\omega_{13} + \omega_{23} + \omega_{56})\tau}{2}\right) - C_{22} \cos\left(\frac{(\omega_{13} + \omega_{23} - \omega_{56})\tau}{2}\right) \\
 &\quad + C_{15} \cos\left(\frac{(\omega_{13} + \omega_{23} - \omega_{45} - \omega_{46})\tau}{2}\right) \\
 \chi_{12,46}^+ &= 2C_{11} \cos\left(\frac{(\omega_{12} - \omega_{46})\tau}{2}\right) - C_{20} \cos\left(\frac{(\omega_{12} + \omega_{46})\tau}{2}\right) + C_{21} \cos\left(\frac{(\omega_{13} + \omega_{23} + \omega_{46})\tau}{2}\right) \\
 &\quad - 2C_{13} \cos\left(\frac{(\omega_{13} + \omega_{23} - \omega_{46})\tau}{2}\right) + C_{15} \cos\left(\frac{(\omega_{12} - \omega_{45} + \omega_{56})\tau}{2}\right) - 2C_{15} \cos\left(\frac{(\omega_{12} + \omega_{45} - \omega_{56})\tau}{2}\right) \\
 &\quad + C_{15} \cos\left(\frac{(\omega_{13} + \omega_{23} + \omega_{45} - \omega_{56})\tau}{2}\right) \\
 \chi_{12,46}^- &= 2C_{10} \cos\left(\frac{(\omega_{12} + \omega_{46})\tau}{2}\right) - C_{19} \cos\left(\frac{(\omega_{12} - \omega_{46})\tau}{2}\right) - 2C_{12} \cos\left(\frac{(\omega_{13} + \omega_{23} + \omega_{46})\tau}{2}\right) \\
 &\quad + C_{21} \cos\left(\frac{(\omega_{13} + \omega_{23} - \omega_{46})\tau}{2}\right) + C_{18} \cos\left(\frac{(\omega_{12} - \omega_{45} + \omega_{56})\tau}{2}\right) - 2C_{18} \cos\left(\frac{(\omega_{12} + \omega_{45} - \omega_{56})\tau}{2}\right) \\
 &\quad + C_{18} \cos\left(\frac{(\omega_{13} + \omega_{23} + \omega_{45} - \omega_{56})\tau}{2}\right) \\
 \chi_{13,46}^+ &= 2C_{13} \cos\left(\frac{(\omega_{13} + \omega_{46})\tau}{2}\right) + 2C_{13} \cos\left(\frac{(\omega_{13} - \omega_{46})\tau}{2}\right) - 2C_{13} \cos\left(\frac{(\omega_{12} - \omega_{23} + \omega_{46})\tau}{2}\right) \\
 &\quad - 2C_{13} \cos\left(\frac{(\omega_{12} - \omega_{23} - \omega_{46})\tau}{2}\right) - 2C_{13} \cos\left(\frac{(\omega_{13} + \omega_{45} - \omega_{56})\tau}{2}\right) - 2C_{13} \cos\left(\frac{(\omega_{13} - \omega_{45} + \omega_{56})\tau}{2}\right) \\
 &\quad + 4C_{13} \cos\left(\frac{(\omega_{12} - \omega_{23} + \omega_{45} - \omega_{56})\tau}{2}\right) \\
 \chi_{13,46}^- &= 2C_{12} \cos\left(\frac{(\omega_{13} + \omega_{46})\tau}{2}\right) + 2C_{12} \cos\left(\frac{(\omega_{13} - \omega_{46})\tau}{2}\right) - 2C_{12} \cos\left(\frac{(\omega_{12} - \omega_{23} + \omega_{46})\tau}{2}\right) \\
 &\quad - 2C_{12} \cos\left(\frac{(\omega_{12} - \omega_{23} - \omega_{46})\tau}{2}\right) - 2C_{12} \cos\left(\frac{(\omega_{13} + \omega_{45} - \omega_{56})\tau}{2}\right) - 2C_{12} \cos\left(\frac{(\omega_{13} - \omega_{45} + \omega_{56})\tau}{2}\right) \\
 &\quad + 4C_{12} \cos\left(\frac{(\omega_{12} - \omega_{23} + \omega_{45} - \omega_{56})\tau}{2}\right)
 \end{aligned}$$

$$\begin{aligned}
 C_0 &= k \left(\frac{2}{3} - \frac{3}{8}k \right) & C_{13} &= \frac{k^2}{192} (1 + \sqrt{1-k})^2 \\
 C_1 &= k \left(1 - \frac{11}{16}k + \frac{3}{32}k^2 \right) & C_{14} &= \frac{k^2}{2} \left(\frac{1}{3} - \frac{1}{4}k \right) \\
 C_2 &= \frac{k}{2} \left(\frac{1}{3} - \frac{1}{4}k \right) & C_{15} &= \frac{k^2}{48} (1 + \sqrt{1-k} - k) \\
 C_3 &= \frac{k}{2} \left(\frac{1}{3} - \frac{1}{3}k + \frac{1}{16}k^2 \right) & C_{16} &= \frac{k}{6} \left(1 + \sqrt{1-k} - \frac{13}{8}k - \frac{7}{8}k\sqrt{1-k} + \frac{5}{8}k^2 \right) \\
 C_4 &= \frac{1}{48}k^2 & C_{17} &= \frac{k}{6} \left(1 - \sqrt{1-k} - \frac{13}{8}k + \frac{7}{8}k\sqrt{1-k} + \frac{5}{8}k^2 \right) \\
 C_5 &= \frac{k^2}{16} \left(\frac{1}{3} + \frac{1}{2}k \right) & C_{18} &= \frac{k^2}{48} (1 - \sqrt{1-k} - k) \\
 C_6 &= \frac{k^2}{16} \left(1 + \frac{1}{3}\sqrt{1-k} - \frac{5}{6}k \right) & C_{19} &= \frac{k^2}{96} (2 - 2\sqrt{1-k} + k) \\
 C_7 &= \frac{k}{24} (1 + \sqrt{1-k} - k)^2 & C_{20} &= \frac{k^2}{96} (2 + 2\sqrt{1-k} + k) \\
 C_8 &= \frac{k}{24} (1 - \sqrt{1-k} - k)^2 & C_{21} &= \frac{1}{96}k^3 \\
 C_9 &= \frac{k^2}{16} \left(1 - \frac{1}{3}\sqrt{1-k} - \frac{5}{6}k \right) & C_{22} &= \frac{k^2}{24} (1-k) \\
 C_{10} &= \frac{k^2}{48} \left(1 - \sqrt{1-k} - \frac{1}{4}k \right) & C_{23} &= \frac{k}{12} (1 + \sqrt{1-k} - k) \\
 C_{11} &= \frac{k^2}{48} \left(1 + \sqrt{1-k} - \frac{1}{4}k \right) & C_{24} &= \frac{k}{12} (1 - \sqrt{1-k} - k) \\
 C_{12} &= \frac{k^2}{192} (1 - \sqrt{1-k})^2 & &
 \end{aligned}$$

The remaining coefficients χ can be derived from the ones given above by substitution of the frequency indices according to the following table:

COEFFICIENT	INITIAL COEFFICIENT	SUBSTITUTION OF FREQUENCY INDICES
χ_{23}	χ_{12}	$12 \leftrightarrow 23, 45 \leftrightarrow 56$
χ_{45}	χ_{12}	$12 \leftrightarrow 45, 23 \leftrightarrow 56, 13 \leftrightarrow 46$
χ_{56}	χ_{12}	$12 \leftrightarrow 56, 23 \leftrightarrow 45, 13 \leftrightarrow 46$
χ_{46}	χ_{13}	$12 \leftrightarrow 45, 23 \leftrightarrow 56, 13 \leftrightarrow 46$
$\chi_{23,45}^+$	$\chi_{12,56}^+$	$12 \leftrightarrow 23, 45 \leftrightarrow 56$
$\chi_{23,45}^-$	$\chi_{12,56}^-$	$12 \leftrightarrow 23, 45 \leftrightarrow 56$
$\chi_{23,56}^+$	$\chi_{12,45}^+$	$12 \leftrightarrow 23, 45 \leftrightarrow 56$
$\chi_{23,56}^-$	$\chi_{12,45}^-$	$12 \leftrightarrow 23, 45 \leftrightarrow 56$
$\chi_{23,46}^+$	$\chi_{12,46}^+$	$12 \leftrightarrow 23, 45 \leftrightarrow 56$
$\chi_{23,46}^-$	$\chi_{12,46}^-$	$12 \leftrightarrow 23, 45 \leftrightarrow 56$
$\chi_{13,45}^+$	$\chi_{12,46}^+$	$12 \leftrightarrow 45, 23 \leftrightarrow 56, 13 \leftrightarrow 46$
$\chi_{13,45}^-$	$\chi_{12,46}^-$	$12 \leftrightarrow 45, 23 \leftrightarrow 56, 13 \leftrightarrow 46$
$\chi_{13,56}^+$	$\chi_{12,46}^+$	$12 \leftrightarrow 56, 23 \leftrightarrow 45, 13 \leftrightarrow 46$
$\chi_{13,56}^-$	$\chi_{12,46}^-$	$12 \leftrightarrow 56, 23 \leftrightarrow 45, 13 \leftrightarrow 46$

Assuming ideal pulses, the expression for one manifold of the $S = 1$, $I = 1$ system becomes equal to the expression for a $S = \frac{1}{2}$, $I = 1$ system.

In the expression for the echo envelope modulation, different contributions to the spectrum can be discerned:

- an un-modulated part (χ_0),
- a part modulated by the same frequency in both time dimensions, giving diagonal peaks in the spectrum, which however vanishes for ideal pulses (χ_d),
- a part modulated along one time dimension giving rise to axial peaks in the spectrum, with terms of the form:

$$\chi_{ij} \cos\left(\omega_{ij} t_{1/2} + \frac{\omega_{ij} \tau}{2}\right)$$

- a part modulated along both time dimensions giving rise to cross peaks in the spectrum, with terms of the form:

$$\chi_{ij,lm}^{+/-} \left(\cos \omega_{ij} t_1 + \omega_{lm} t_2 + \frac{(\omega_{ij} + \omega_{lm}) \tau}{2} \right)$$

An inspection of the HYSORE formula reveals the presence of 16 cross peak terms from $\Delta m_l = \pm 1$ nuclear transitions and of 20 cross peaks from $\Delta m_l = \pm 2$ nuclear transitions. However, the intensities of most of these cross peaks are too low to be detected experimentally and the experimental HYSORE spectra turn out to be much simplified. In the limit of weak hyperfine interaction, encountered in most of the ESEEM experiments, only cross peaks in the first quadrant of the HYSORE spectrum are observed. Furthermore, as in this case $k \ll 1$, only terms with amplitude factors linear in k have to be considered, while terms depending on higher powers of k can usually be neglected [40].

A comparison of the modulation factors $\chi_{ij,lm}$ of different cross peaks allowed the individuation of only two ($\chi_{12,45}^+$ and $\chi_{23,56}^+$), which depend linearly on the modulation depth parameter k , as observed also in the $S = \frac{1}{2}$ case [40]. Hence only four of the eight theoretically possible cross peaks arising in the first quadrant from $\Delta m_l = \pm 1$ nuclear transitions relative to a single EPR transition are experimentally observable, namely the cross peaks at $(\omega_{12}, \omega_{45})$, $(\omega_{45}, \omega_{12})$, $(\omega_{23}, \omega_{56})$ and $(\omega_{56}, \omega_{23})$ (Fig. 5.3).

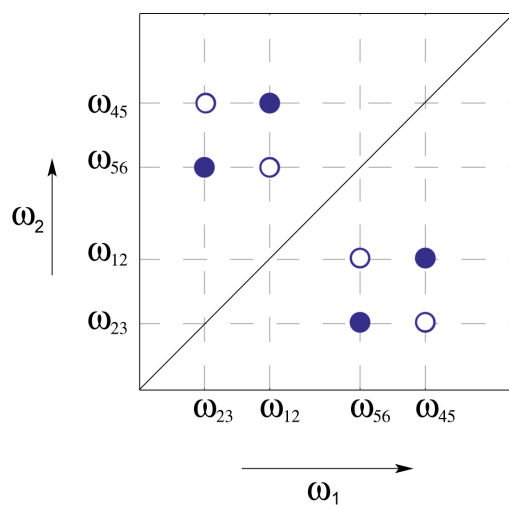


Fig. 5.3 Schematic plot for the peaks in the first quadrant of the HSCORE spectrum for a system with $l=1$. Full circles represent the cross peaks with amplitude factors proportional to k , open circles represent the cross peaks with amplitude factors proportional to higher powers of k , and thus usually too weak to be observed.

CHAPTER 6

ESEEM EXPERIMENTS ON THE PERIDININ TRIPLET STATE

ESEEM spectroscopy is applied to the characterization of the environment of the peridinin molecule identified as the principal chlorophyll triplet quencher in the photoprotection mechanism of the PCP antenna complex. The study of the interaction of the peridinin triplet state with a water molecule interposed between the pigments involved in TTET will allow gaining insights into the role of this water molecule in the photoprotection mechanism.

In order to isolate the modulation of the spin echo envelope due to the interaction with the protons of the water molecule from the contributions of other nuclei, the measurements were performed both on untreated and D₂O-exchanged protein complexes.

6.1 MATERIALS AND METHODS

6.1.1 SAMPLE PREPARATION

PCP proteins, extracted and purified according to references [49,50], were kindly supplied by R. G. Hiller. The sample concentration was ~1.4 mg/ml.

H/D exchange was achieved through dialysis with a deuterated buffer (50 mM tricine, 20 mM KCl, pD~7.5) at 4 °C in N₂ atmosphere. A volume of about 1 ml of protein in protonated buffer was inserted in dialysis tubing (>12kDa cut-off), which was then immersed into 40 ml of deuterated buffer. The deuterated buffer was exchanged twice. A part of the D₂O-exchanged protein solution was removed after 1.5 h of dialysis and the rest was left in the deuterated buffer up to an overall exchange time of about 20 h.

The same volumes of untreated and D₂O-exchanged protein were used for the preparation of the

EPR samples. Oxygen was removed from the samples by flushing argon in the EPR tube before sealing and freezing in liquid N₂, the residual oxygen was removed by adding glucose, glucose oxidase and catalase [51].

6.1.2 ESEEM EXPERIMENTS

The ESEEM experiments were performed on a Bruker Elexsys E580 pulse EPR spectrometer with a dielectric ring resonator (EN4118X-MD4). The samples were excited with an Nd:YAG laser (Quantel Brilliant) at 532 nm with about 10 mJ per pulse and a repetition rate of 10 Hz. The measurements were performed at 20 K and the temperature was controlled with a helium cryostat (Oxford CF935) driven by a temperature controller (Oxford ITC503).

The ESEEM was measured at four different magnetic field values, corresponding to the following canonical transitions of the triplet state: Z⁻ (300 mT), X⁺ (328 mT), X⁻ (362 mT) and Y⁻ (375 mT). The measurements were performed with DAF (Delay-after-flash) times of 50 ns or 13 μs between the laser pulse and the pulse sequence.

Two-pulse ESEEM experiments were performed by measuring the integrated intensity of the electron spin echo as a function of the pulse delay time τ in the two-pulse echo sequence: $\frac{\pi}{2} - \tau - \pi - \tau - \text{echo}$. The duration of the $\frac{\pi}{2}$ and π pulses was 16 and 32 ns respectively. The initial delay time τ in the two-pulse experiments was chosen to be 100 ns and incremented in steps of 8 ns. The data set lengths were of 375 points. In the two-pulse ESEEM experiments data were accumulated for 6-16 hours, depending on the magnetic field position.

Three-pulse ESEEM experiments were performed with the three-pulse echo sequence $\frac{\pi}{2} - \tau - \frac{\pi}{2} - T - \frac{\pi}{2} - \tau - \text{echo}$ and by incrementing T. The delay time τ between the first two pulses in the three-pulse ESEEM experiment was selected in order to suppress the proton contribution and maximize the deuterium contribution according to:

$$\tau_{\text{suppress}} = \frac{n}{\nu_H} \quad \tau_{\text{max}} = \frac{(2n+1)}{2\nu_D}$$

The initial value of T was chosen to be 20 ns and varied in 12 ns increments. A total of 512 data points was recorded. Data were accumulated for 4-14 hours, depending on the magnetic field position.

All measurements were performed at a microwave frequency of 9.7 GHz. Two-step and four-step phase cycles were used for the two-pulse and three-pulse ESEEM, respectively. The final 10 points of each time domain data set were acquired with the integration window positioned 400 ns off the echo to define the background.

The measurements were performed on the untreated and D₂O-exchanged samples with the same experimental parameters.

6.1.3 DATA ANALYSIS

The primary output of the ESEEM experiments is a time domain signal starting at some time $\tau_0 \geq t_d$, where t_d is the spectrometer dead time. The data were processed for analysis and interpretation both in the time and in the frequency domain.

The data analysis was performed with a home-written program in Matlab®. The experimental two- or three-pulse ESEEM time domain data acquired on both normal and D₂O-exchanged samples in the same conditions are processed following the ratio method proposed by Mims *et al.* [52]. The envelope obtained for the D₂O-exchanged sample was divided by the envelope obtained for the untreated sample after normalization of both envelopes. The envelope division partly removes the decay of the time trace due to relaxation processes and enhances the modulations due to the deuterium nuclei, allowing the identification of exchangeable protons in the environment of the paramagnetic system, in this case the peridinin triplet state. The motivation behind the ratio method is based on the product rule, which states that the envelope modulation due to several nuclei is the product of the modulations caused by each individual nucleus. Hence in theory the division should yield a trace containing only the modulations due to the deuterium nuclei and the exchanged protons:

$$\frac{E_{\text{mod}}(I_1, I_2, \dots, I_D, \dots, I_N)}{E_{\text{mod}}(I_1, I_2, \dots, I_H, \dots, I_N)} = \frac{E_{\text{mod}}(I_D)}{E_{\text{mod}}(I_H)}$$

The quotient time trace was then dead-time reconstructed following a procedure proposed by Mims [53]. The instrumental dead-time prevents the observation of the initial part of the envelope and introduces artifacts in the spectrum obtained by Fourier transform of the time domain data. The procedure proposed by Mims reduces the artifacts by reconstruction of the dead-time portion of the experimental time trace. The dead-time reconstruction procedure can be outlined as follows: the initial intensity of the modulation is estimated from the experimental time trace and the dead-time portion is provisionally corrected with a sine segment. Then the spectrum is computed by Fourier transform and the peaks are selected in an interactive windowing procedure. The spectrum is then multiplied by the determined window function and the inverse Fourier transform yields modulations with appropriate amplitudes of the frequencies detected in the spectrum. The first segment of these modulations is joined to the experimental time trace.

The dead-time reconstructed time traces were then apodized with a Hamming window, zero-

filled to 2048 data points and the spectra were computed by Fourier transform.

6.2 RESULTS AND DISCUSSION

6.2.1 ESEEM EXPERIMENTS

In Fig. 6.1 C the field-swept echo-detected EPR spectrum of the PCP complex of *Amphidinium carterae* recorded at 20 K is shown and the canonical transitions are highlighted. An identical spectrum is obtained for the deuterated PCP complex.

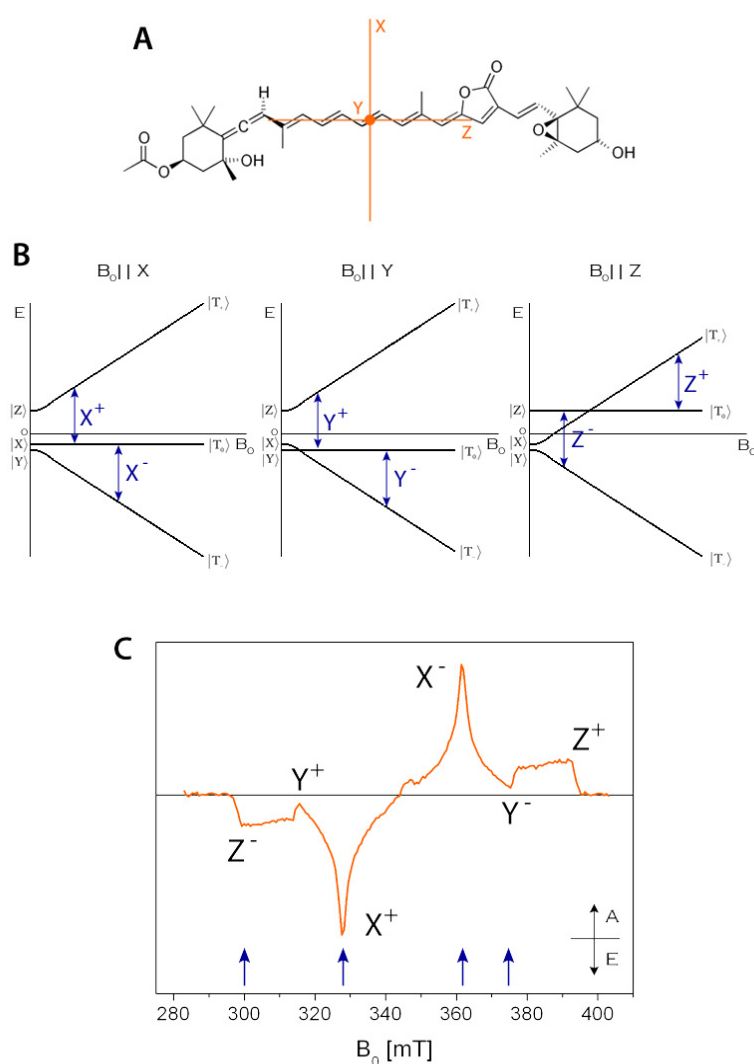


Fig. 6.1 (A) Molecular structure of peridinin with the direction of the ZFS principal axes as defined in reference [13]. (B) Diagrams of the triplet energy levels of peridinin in a magnetic field parallel to each of the ZFS axes with the canonical transitions. (C) Two-pulse field-swept echo-detected EPR spectrum of PCP from *A. carterae* at 20 K with ZFS tensor canonical orientations. The blue arrows indicate the field positions at which the ESEEM experiments were performed. Order of energy for zero-field triplet sublevels: $|Z\rangle > |Y\rangle > |X\rangle$. Spin polarization: *eaeaea*. (A=absorption, E=emission).

The EPR spectrum of the peridinin triplet state is significantly wider than the microwave pulse excitation bandwidth and hence orientation selection applies for pulse EPR experiments. ESEEM experiments performed at different magnetic fields selectively excite only spin systems with certain orientations with respect to those fields. ESEEM data were collected at four field positions, corresponding to the following canonical transitions of the triplet state: Z^- , Y^- , X^- and X^+ (Fig. 6.1).

The spin polarization of the field-swept echo-detected EPR spectrum of peridinin is reflected also in the ESEEM time traces, which can be either emissive or absorptive, depending on the spin polarization at the considered magnetic field position. The emissive time traces were inverted for further analysis.

The echo intensity varies greatly with the magnetic field position, thus influencing the signal-to-noise ratio of the corresponding ESEEM time trace. The echo has its maximum intensity at the X^- and X^+ field positions, and the corresponding echo envelopes will be characterized by a high signal-to-noise ratio. On the other hand, the echo intensity at the $Z^{+/-}$ and especially at the $Y^{+/-}$ field positions is low, leading to a low signal-to-noise ratio or, as in the case of the $Y^{+/-}$ field positions, preventing the ESEEM measurement altogether. However, kinetic studies of the triplet state evolution in PCP have shown that a spin polarization inversion accompanied by an increase in signal intensity occurs for the Y transitions for increasing delay-after-flash (DAF) times, due to the strongly anisotropic decay of the three triplet state spin sublevels [13] (Fig. 6.2). This allows the detection of ESEEM at delay times corresponding to the maximum spin polarization inversion.

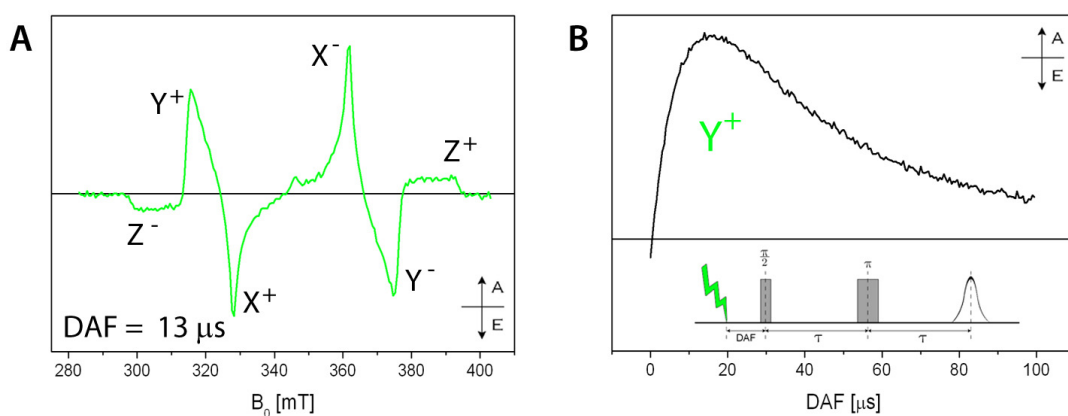


Fig. 6.2 (A) Field-swept echo-detected EPR spectrum of PCP from *A. carterae* at 20K and for a DAF of 13 μ s. (B) Echo-detected kinetics at the Y^+ canonical field. The inset shows the pulse scheme for echo-detected EPR with laser excitation. A=absorption, E=emission. (Adapted from reference [13]).

6.2.1.1 H/D EXCHANGE

In order to specifically study the interaction between the water molecule and the peridinin triplet state, the ESEEM experiments were performed both on untreated and D₂O-exchanged protein samples. The electron spin echo envelope obtained for the D₂O-exchanged sample was then divided by that obtained for the untreated sample, yielding an echo envelope with modulations primarily due to the exchangeable deuterons coupled with the peridinin triplet state.

The rate of exchange can vary greatly for different protons in different environments in proteins. The protein sample was exposed to D₂O for two different times for a qualitative evaluation of the extent of H/D exchange.

The ESEEM time traces recorded for the samples with exchange times of 1.5 and 20 h are identical after division by the time trace of the untreated sample (Fig. 6.3). The presence of a greater number of deuterons in the environment of Per614 in the sample with the longer exchange time would cause an increase of the modulation depth, which however is not observed. It can thus be concluded that all the exchangeable protons in the environment of the paramagnetic species are exchanged within a short time. In the following only the 1.5 h-exchanged data are considered.

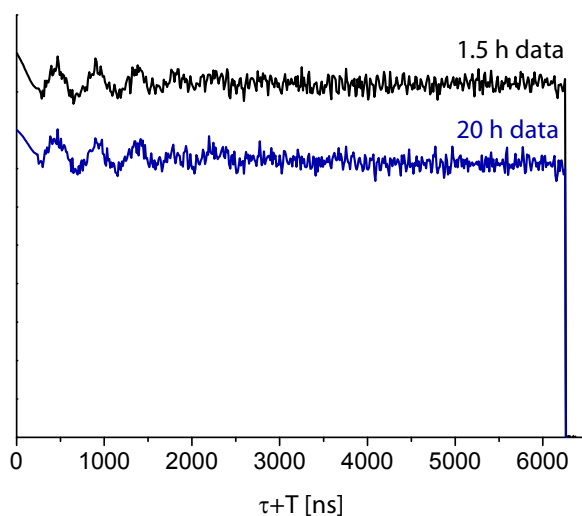


Fig. 6.3 Ratio of experimental three-pulse ESEEM time traces recorded on the 1.5 h and the 20 h D₂O-exchanged protein samples at the X⁺ field position (328 mT).

6.2.1.2 TWO-PULSE ESEEM

The electron spin echo envelopes obtained for the untreated and D₂O-exchanged samples in the two-pulse ESEEM experiment and the envelopes resulting from the division are reported in Fig. 6.4 and 6.5.

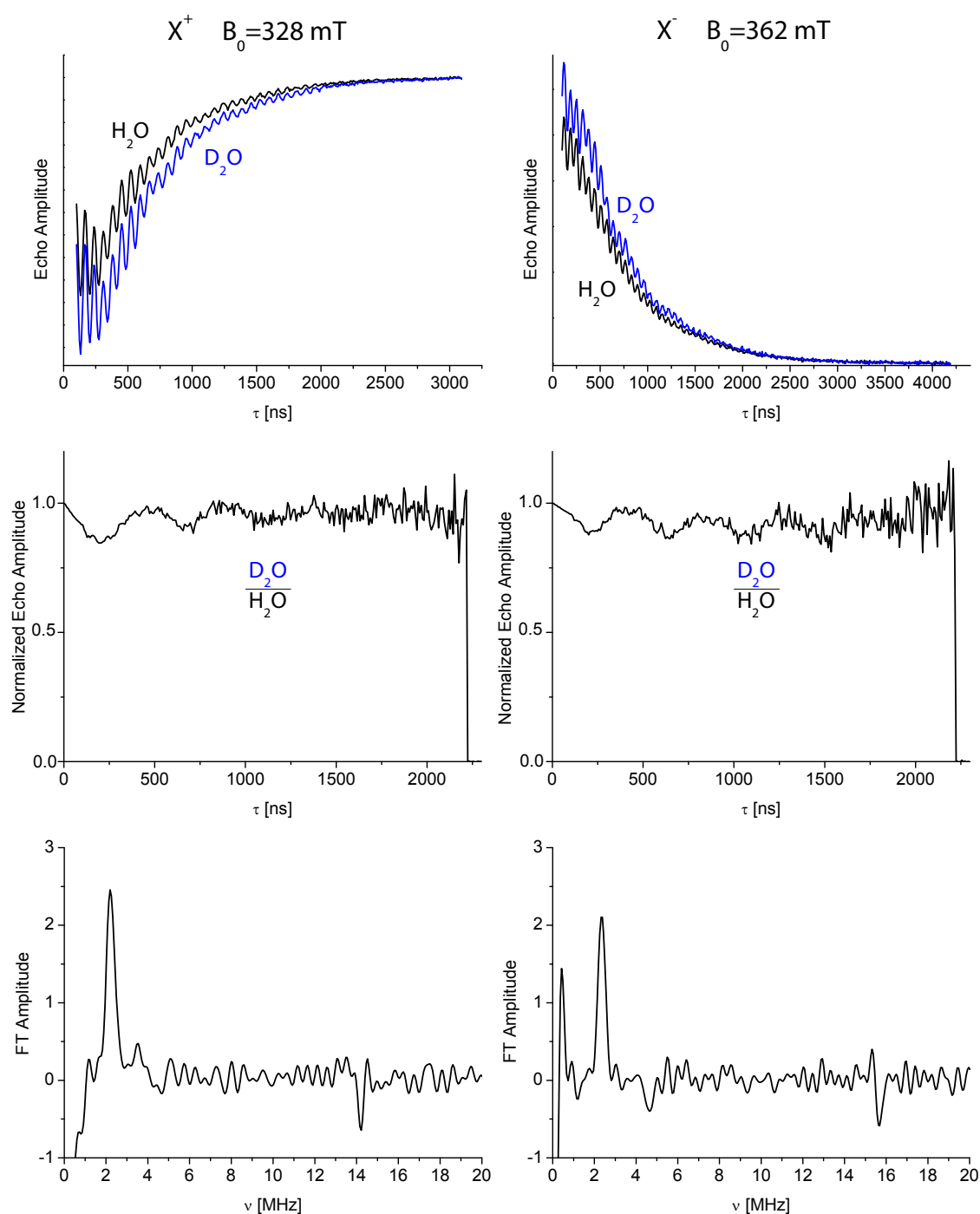


Fig. 6.4 Experimental two-pulse ESEEM time traces collected at the X^- and X^+ field positions, normalized dead-time reconstructed quotient traces obtained by envelope division and corresponding ESEEM spectra obtained by Fourier transform of the quotient trace.

The ESEEM data reported in Fig. 6.4 was recorded at two field positions corresponding to the low-field and high-field transitions for spin systems with the ZFS axis X directed along the magnetic field direction. The two-pulse echo envelopes collected for the untreated and D_2O -exchanged

samples both show a high frequency modulation due to the hydrogen atoms coupled to the peridinin triplet state. The envelope of the D₂O-exchanged sample shows additional modulations at a slower frequency, due to deuterium nuclei. The latter modulations are enhanced by the division of the envelopes of the D₂O-exchanged and the untreated sample. The quotient traces resulting from the envelope division procedure are characterized by a shallow modulation pattern with a frequency close to the deuterium Larmor frequency.

The Fourier transform of the quotient traces yields spectra characterized by a peak with positive amplitude at 2.20 and 2.32 MHz for the ESEEM at the X⁺ and the X⁻ field position respectively. Additionally a peak with negative amplitude at about twice those frequencies is present in both spectra. A signal with a derivative shape close to the proton Larmor frequency (about 14 and 15.5 MHz) is also present in both spectra due to the incomplete elimination of the proton contribution by the envelope division procedure.

In Fig. 6.5 the ESEEM time traces relative to field positions corresponding to the other two transitions of the lower triplet state manifold for the canonical orientations, Y⁻ and Z⁻, are represented. Again the echo envelopes are characterized by fast modulations due to coupled hydrogen nuclei. The ESEEM of the D₂O-exchanged sample at the Y⁻ field position shows weak additional modulations due to coupled deuterium nuclei. These slower modulations are clearly visible in the quotient trace obtained by envelope division. The spectrum obtained by Fourier transform contains a peak with positive amplitude at 2.50 MHz and a very weak peak with negative amplitude can be discerned at twice that frequency.

The quotient trace obtained for the Z⁻ field position is characterized by relatively deep modulations at the proton Larmor frequency, while no modulations at the deuterium Larmor frequency are visible. The spectrum of the quotient trace displays a peak of very low intensity at 1.95 MHz, the Larmor frequency of deuterium nuclei at the Z⁻ magnetic field value, and a peak with negative amplitude at twice that frequency. Due to the extremely low intensity of these peaks, contributions of deuterium nuclei to the echo envelope modulation can be considered negligible. The signal at the proton Larmor frequency in the FT spectrum is due to the exchanged protons, the derivative shape arises from the dead-time reconstruction and envelope division procedures.

The experimental ESEEM traces depicted in Fig. 6.4 and 6.5 clearly show that the echo intensity decays to zero in the course of the experiment, hence in the quotient trace modulations are visible only at short inter-pulse delays τ , while the lower signal-to-noise ratio for long inter-pulse delays produces significant noise in the later part of the traces.

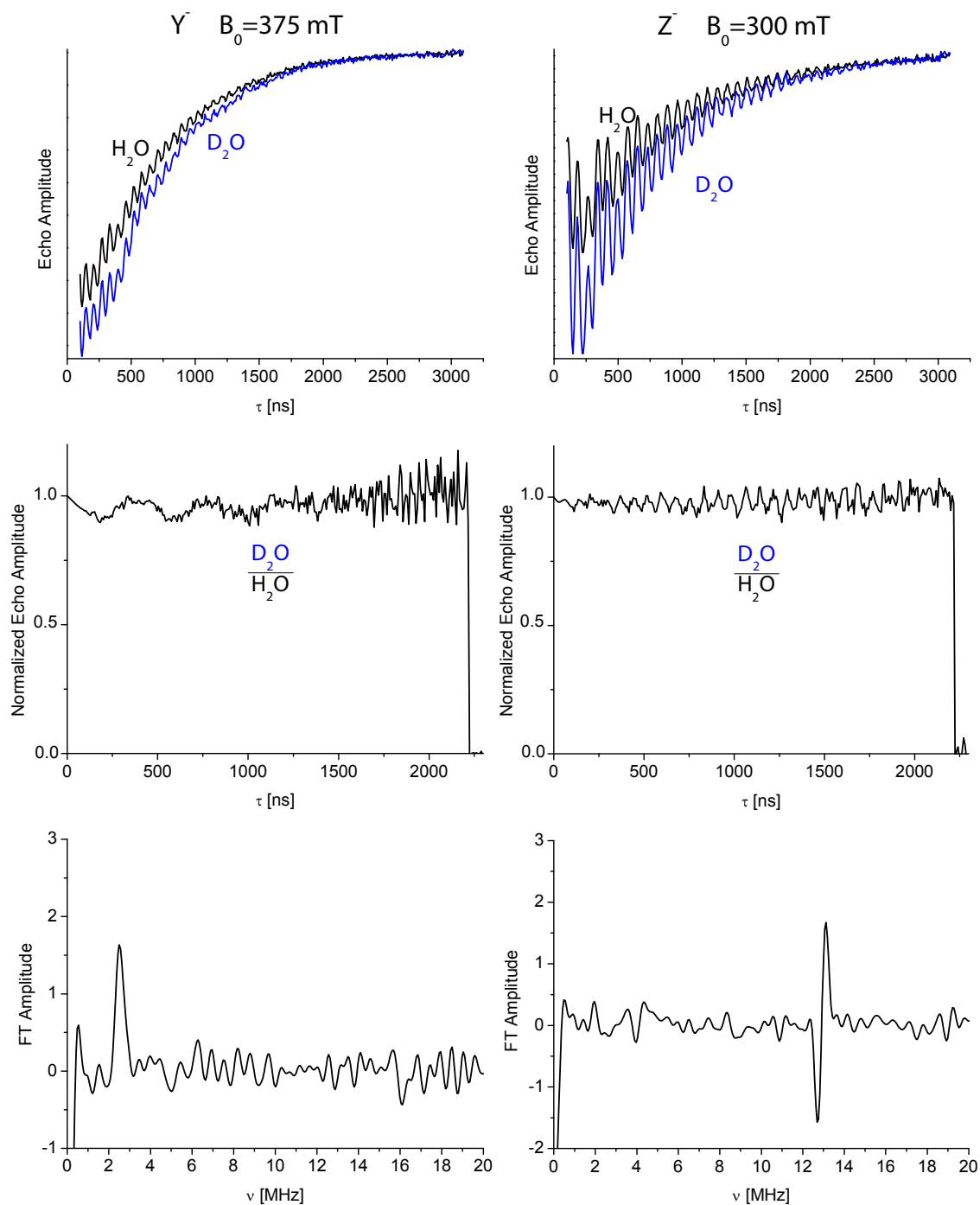


Fig. 6.5 Experimental two-pulse ESEEM time traces collected at the Y⁻ and Z⁻ field positions, normalized dead-time reconstructed quotient trace obtained by envelope division and corresponding Fourier transforms.

6.2.1.3 THREE-PULSE ESEEM

The electron spin echo envelopes obtained for the untreated and D₂O-exchanged sample in the three-pulse ESEEM experiment and the envelopes obtained by the ratio method are reported in Fig. 6.6 and 6.7.

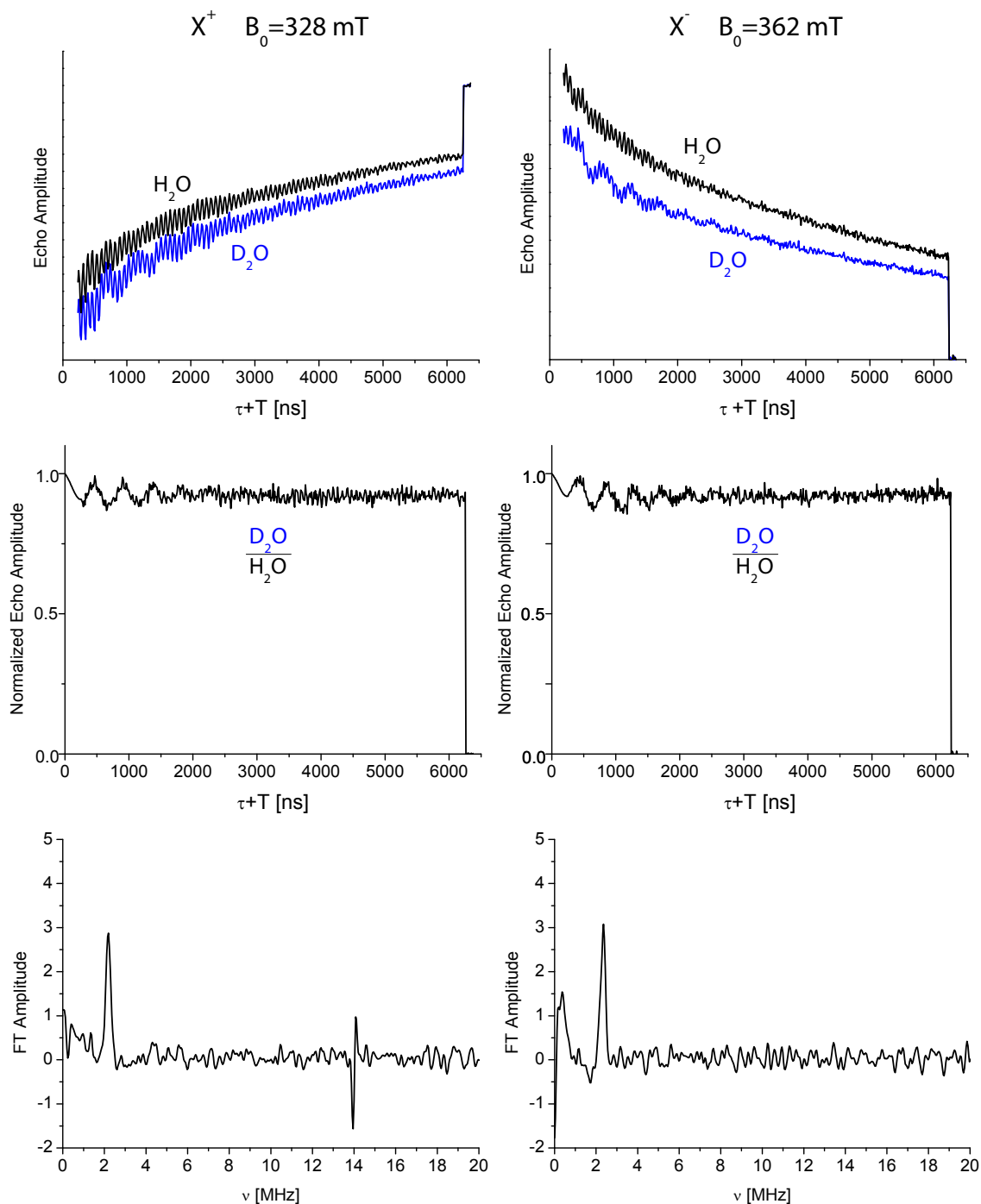


Fig. 6.6 Experimental three-pulse ESEEM time traces collected at the X^- and X^+ field positions with $\tau = 196$ and 216 ns respectively, normalized dead-time reconstructed quotient traces obtained by envelope division and Fourier transform of the quotient trace.

The ESEEM data reported in Fig. 6.6 is relative to the two possible transitions in the triplet state manifold for magnetic fields directed along the ZFS axis X of peridinin. The three-pulse echo envelopes of the untreated and D_2O -exchanged samples again show fast modulations at the hydrogen Larmor frequency and the echo envelope of the D_2O -exchanged sample shows an

additional slow modulation at the deuterium Larmor frequency. The FT spectra contain a single peak at a frequency close to the Larmor frequency of deuterium nuclei for both the X^+ and the X^- field position, at 2.20 and 2.36 MHz respectively.

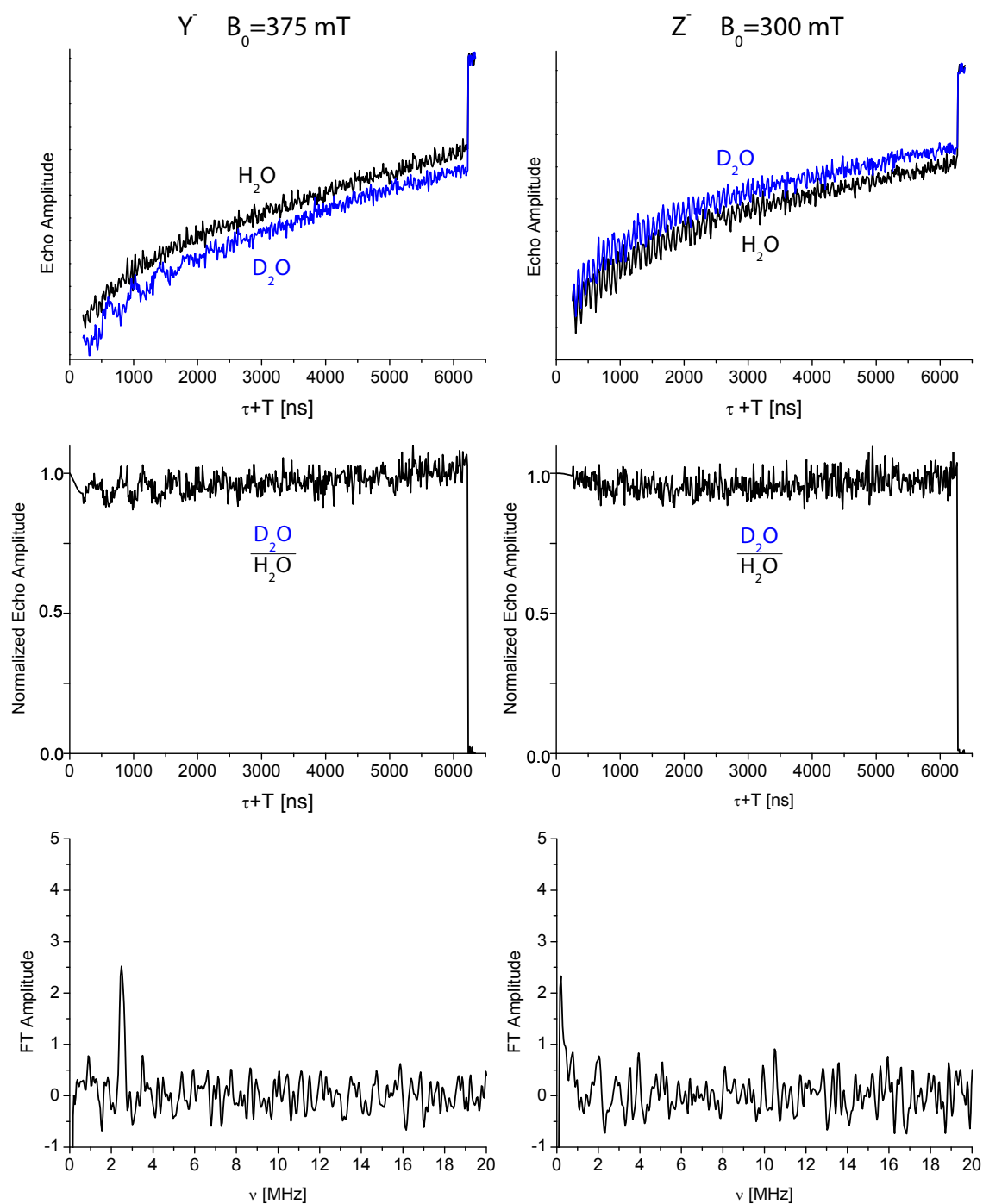


Fig. 6.7 Experimental three-pulse ESEEM time traces collected at the Y and Z field positions with $\tau = 188$ and 236 ns respectively, normalized dead-time reconstructed quotient trace obtained by envelope division and Fourier transform of the quotient trace.

In Fig. 6.7 the ESEEM time traces relative to the Y- and Z- field positions are represented. In the echo envelope collected at the Y- field position for the D₂O-exchanged sample slow modulations due to coupled deuterium nuclei can be discerned next to the fast modulations of coupled hydrogen nuclei. The Fourier transform of the quotient trace obtained by envelope division gives a spectrum with a peak at 2.48 MHz, close to the deuterium Larmor frequency at that magnetic field value. However, as far as the data collected at the Z- field position is concerned, neither the experimental echo envelope for the D₂O-exchanged sample, nor the quotient trace obtained by envelope division display modulations at the deuterium frequency.

6.2.2 DISCUSSION OF THE ESEEM DATA

In the present work the ESEEM experiment coupled with H/D isotope exchange has been applied for the first time to a triplet state system in order to identify and characterize water molecules in its close environment.

The interpretation of the ESEEM results is accomplished mainly by simulations of both the time traces obtained by envelope division and of the corresponding Fourier transformed spectra, as will be extensively discussed in the following chapter. However some qualitative considerations are already possible from the inspection of the experimental data represented above.

The presence of slow modulations in the D₂O-exchanged sample confirms that an efficient H/D exchange was achieved with the dialysis procedure. The comparison of experimental data collected for protein samples with different exchange times lead to the conclusion that the exchangeable protons in the environment of the peridinin triplet state were all exchanged with deuterium nuclei within the first 1.5 h of dialysis in deuterated buffer.

The ESEEM traces obtained with the envelope division procedure display shallow modulations, indicating the presence of super-hyperfine interactions. The marked attenuation of the modulations with time points to the fact that they are due to a small number of nuclei, since many weakly coupled nuclei would cause slow modulation damping.

The comparison of the experimental ESEEM traces of the two-pulse and three-pulse experiment shows that the echo decay is much more pronounced in the two-pulse experiment. As already explained in chapter 3, the time constant determining the decay of the echo amplitude due to relaxation processes depends on the phase memory time of the electron spin in the two-pulse echo experiment, while in the three-pulse echo experiment it depends on the much longer phase memory time of the nuclear spins. The slower decay in the three-pulse experiment allows acquisition on a longer time scale, while the echo intensity in the two-pulse experiment soon decays to zero, preventing the detection of envelope modulations at longer inter-pulse delays.

The damping of the deuterium modulation in the quotient trace, containing information on the number and distance of the coupled nuclei, can thus be better observed in the three-pulse experiment.

Triplet state systems are generally characterized by orientation selection; hence the ESEEM traces were collected at different magnetic field positions, corresponding to canonical transitions of the peridinin triplet state. It can be noted that the echo envelopes collected at different fields are characterized by different modulation frequencies and modulation depths. The absence of deuterium modulation in the echo envelopes collected at the Z' field position in both the two-pulse and the three-pulse ESEEM experiments points to the fact that the hyperfine interaction tensor of the nuclei causing the modulations observed at the other field positions is directed with one axis approximately parallel to the ZFS axis Z of the peridinin triplet state. As explained in chapter 4, due to the dependence of the modulation depth parameter k on the non-diagonal elements of the hyperfine tensor through B , the modulation vanishes if the external magnetic field is parallel to one of the principal axes of the hyperfine interaction tensor. Since an analogous orientation of the hyperfine interaction tensors of a large number of deuterium nuclei in different positions with respect to the peridinin triplet state is highly unlikely, the absence of modulations at the Z' field position confirms that the modulations observed at the other field positions are due to a small number of selected nuclei characterized by a particular position and orientation with respect to Per614.

The expression for the echo envelope modulation for a particular transition in a triplet state contains two modulation frequencies, the nuclear Larmor frequency and a frequency shifted from the nuclear Larmor frequency by the hyperfine interaction of the nucleus with the triplet state. In the case of a triplet state coupled to a nucleus with $I=1$, each of those frequencies is split into two different frequencies by the nuclear quadrupole interaction (see chapter 5). In addition to that, sum and difference combination frequencies are present in two-pulse ESEEM experiments. The two-pulse ESEEM spectra show a single peak with positive amplitude at a frequency close to the deuterium Larmor frequency at the considered magnetic field and a weak peak with negative amplitude at about twice the deuterium Larmor frequency. This sum combination line is characteristic of the two-pulse experiment; the difference combination peak is not visible, since it would fall close to the zero frequency where the spectrum is distorted by artifacts due to the Fourier transformation. The three-pulse ESEEM spectra show just a single peak with positive amplitude close to the deuterium Larmor frequency. The fact that the lines collapse into a single peak leads to the conclusion that the nuclei interacting with the peridinin triplet state are characterized by weak hyperfine and nuclear quadrupole interactions.

The ESEEM was recorded both at the X^- and at the X^+ field positions in order to compare data corresponding to the two different transitions of the triplet state manifold for a particular orientation of the magnetic field with respect to the ZFS tensor frame, namely for a magnetic field directed along the X axis. According to the formulae describing the modulation of the echo envelope for a triplet state reported in chapter 5, low- and high-field transitions are characterized by different modulation frequencies and modulation depths. The peaks in the FT spectra for the X^- and X^+ field positions should be shifted from the nuclear Larmor frequency in opposite directions due to the hyperfine interaction with coupled nuclei. Due to the presence of only very weak hyperfine interactions in the present case, the shift of the peak maxima in the ESEEM spectra with respect to the deuterium Larmor frequency at the corresponding magnetic field value is too small to allow direct considerations on the magnitude of the hyperfine interaction.

In the following chapter the spectroscopic parameters characterizing the studied system will be extracted from the experimental data by simulation of the time and frequency domain, and conclusions on the local structure of the photoprotective site in the PCP antenna complex will be drawn.

CHAPTER 7

SIMULATION AND INTERPRETATION OF ESEEM DATA

The ESEEM experiments give insights into the geometry and electronic structure of the surroundings of the paramagnetic species, in this case the peridinin triplet state, through the modulation of the spin echo envelope by the frequencies of nuclei interacting with it. The information is extracted from the two- and three-pulse ESEEM experimental data by simulations in the time and frequency domain.

The time and frequency domain data of two- and three-pulse ESEEM are analyzed in parallel, as some information can be extracted more easily by considering the time domain, other by considering the frequency domain. Specifically, the time trace allows a more exact determination of the modulation depth and of the damping of the modulations, depending on the number and distance of the interacting nuclei. On the other hand, the nuclear frequencies are more readily determined from the frequency domain spectrum. The analysis of the time domain data is particularly important in the case of weak hyperfine interaction, where the nuclear frequencies do not differ considerably from the Larmor frequency of the nucleus and the main information on the spin system can be derived from the modulation depth and the decay of the modulations.

The simulation and interpretation of the experimental data is combined with quantum mechanical computations, providing both a guess of the geometry of the region of interest in the protein and starting values for the simulations. In the following the results of the geometry optimizations are first presented, and then the simulation of the experimental data is described.

7.1 METHODS

7.1.1 COMPUTATIONAL DETAILS

The geometry of the pigment pair involved in the photoprotective mechanism in PCP was

optimized using the ORCA program package [54] and the ONIOM method in Gaussian09 [55].

A DFT ground state optimization with no constraints of a system constituted by Per614, Chl601 without phytol chain, the sidechain of His66 and the water molecule H₂O 701 coordinated to the Mg ion of Chl601 according to X-ray nomenclature [7] was performed with the two hybrid functionals B3LYP (defined as in the Gaussian program system) and PBE0 and the 6-31G(d) basis set [56] in ORCA. The input coordinates were taken from the X-ray structure (PDB entry 1PPR) and the hydrogen atoms were added with AutoDockTools. Further optimizations with constraints and including also other residues were performed using only the PBE0 functional.

Additionally two-layer ONIOM B3LYP/6-31G(d):UFF calculations were performed with Gaussian09. The inner layer, treated at B3LYP level, was defined by the same molecules as in the ORCA geometry optimizations and the outer layer, treated at molecular mechanics level, was defined by various portions of the protein surroundings. The hydrogen atoms were added and minimized prior to the ONIOM calculation with the PM3 method in Gaussian09.

The spin density of the triplet state of the peridinin molecule was computed in a single-point unrestricted calculation in ORCA on selected optimized geometries with the B3LYP functional and the EPRII basis set for the H, C, N and O nuclei [57,58] and with the 6-31G(d) basis set for the Mg ion of chlorophyll.

The hyperfine coupling parameters of the hydrogen atoms of the water molecule were calculated with the purposely tailored EPRII basis set [57-59] for selected optimized geometries.

7.1.2 SIMULATION OF ECHO-DETECTED EPR SPECTRA

The validity of the computed geometries was evaluated through comparison of experimental field-swept echo-detected EPR spectra with EPR spectra calculated for that specific structure exploiting the spin conservation of the TTET mechanism (see section 2.3.3).

Echo-detected EPR spectra of the peridinin triplet state in PCP were simulated using the *Easyspin* routine (version 3.1.7) [60] in Matlab®. Powder EPR spectra are simulated by the function *pepper* of *Easyspin* based on the full diagonalization of the triplet state spin Hamiltonian, comprehensive of the Zeeman and the ZFS interactions. The line-shape of the EPR spectrum is calculated assuming a powder-like distribution of molecular orientations with respect to the magnetic field direction. The spectra are simulated based on the ZFS parameters D and E and the relative zero-field population probabilities.

The ZFS parameters D and E of the peridinin triplet state in PCP were taken from results of previous studies ($D = -1348$ MHz, $E = -131.6$ MHz) [13]. The ordering of the triplet state sublevels is

$|Z\rangle|Y\rangle|X\rangle$.

The relative population probabilities were calculated with a home-written program in Matlab®, developed previously in the research group [23] and based on the concept of spin conservation during triplet-triplet energy transfer, as explained in section 2.3.3, according to:

$$P_k^A = \sum_h \cos^2 \theta_{hk} P_h^D$$

The population probabilities depend on the donor's sublevel populations P_h^D , determined by simulation of the donor's *in vitro* EPR spectrum (Chl *a* in Me-THF glass [1]), and on the relative orientations of the ZFS axes of the pigments through the factor $\cos^2 \theta_{hk}$.

The ZFS axes of chlorophyll were taken as defined in the literature [61,62] and the ZFS axes of peridinin were determined by applying the procedure of principal components analysis using the Matlab® function *princomp* to the spatial coordinates of the peridinin molecules taken from the optimized geometry. The method is based on the solution of the covariance matrix of the data, in which the eigenvalues represent the amount of variance attributed to each eigenvector. The resulting eigenvectors are a good approximation of the ZFS axes as determined in previous EPR investigations on a single crystal of β -carotene [63] and on deuterododecapentaenal in polyethylene film [64]. The solution vector with the greatest eigenvalue lies along the main axis (Z) of the peridinin molecule, the vector with the intermediate eigenvalue lies along the C-H bonds (X) and the vector with the smallest eigenvalue is perpendicular to the molecular plane.

7.1.3 SIMULATION OF ESEEM DATA

The interpretation of the ESEEM experiments was achieved through simulation of both the time and frequency domain data. The simulations were performed with home-written programs in Matlab® based on the *EasySpin* routine (version 3.1.7) [60]. The simulation of ESEEM spectra is implemented in the *saffron* function of *EasySpin* [48]. The method is based on a numerical implementation of the density matrix formalism of Mims [27], described in detail in chapter 4, it computes the modulation frequencies, calculates the amplitudes of the corresponding peaks and constructs a spectrum histogram. The time domain signal is obtained by inverse Fourier transform.

ESEEM data of powder samples are simulated by computing and summing the signals over all relevant orientations of the spin system with respect to the external magnetic field. Orientation and transition selection in systems with anisotropic electron spin Hamiltonians, as in the case of triplet states, is performed by pre-computing the orientations contributing to the ESEEM spectrum for a certain microwave field and pulse excitation width based on the parameters of the

spin Hamiltonian, e.g. the ZFS tensor in triplet state systems. The ESEEM signal is then computed only for these orientations and summed with the appropriate weights.

The input parameters needed for the simulations are the experimental parameters and the following parameters defining the spin system:

- type of spin system (S)
- number and type of interacting nuclei (I)
- the parameters D and E , defining the ZFS interaction
- the principal values of the dipolar hyperfine interaction tensor T_{xx} , T_{yy} and T_{zz} and the isotropic hyperfine interaction constant a_{iso}
- the parameters $e^2qQ\hbar^{-1}$ and η defining the nuclear quadrupole interaction
- Euler angles defining the orientation of the above mentioned interaction tensors with respect to the molecular frame

The ZFS parameters D and E were taken from literature [13] and the orientation of the ZFS tensor was determined by principal components analysis as described in the previous section.

Initial simulation parameters for the hyperfine interaction were obtained from quantum mechanical calculations (see section 7.1.1), consisting of both the isotropic and the dipolar contribution to the hyperfine interaction. Alternatively the dipolar hyperfine interaction tensors were derived from a certain input structure of the peridinin and water molecule and a calculated spin density distribution with a variant of the point-dipole approximation. In the peridinin triplet state the spin density is not concentrated on a single point, but distributed over the atoms of the peridinin chain, hence the simple point-dipole approximation breaks down. The dipolar interaction can be approximated as a weighted sum of point-dipolar interactions between the nucleus and the various atoms over which the spin density is distributed:

$$T_{total} = \sum_i \rho_i T_i$$

where T_i is the dipolar tensor calculated for the interaction of the nucleus with the normalized spin density ρ_i on the atom i . The hyperfine tensor resulting from an interaction with a distributed spin density is usually orthorhombic.

The hyperfine interaction tensors for the hydrogen/deuterium atoms of the water molecule were computed in a home-written subroutine of the ESEEM simulation program based on a numerical approach developed for multi-nuclear metal clusters [65,66]. The hyperfine interaction matrices T_i for each atom of the peridinin chain were calculated and summed in a common axis system,

defined by the coordinate system of the input geometry. In this axis system each individual dipolar hyperfine interaction matrix is given by:

$$T_i = -\frac{\mu_0}{4\pi\hbar} \frac{g_e g_n \beta_e \beta_n}{r_i^5} \begin{bmatrix} r_i^2 - 3x^2 & -3xy & -3xz \\ -3xy & r_i^2 - 3y^2 & -3yz \\ -3xz & -3yz & r_i^2 - 3z^2 \end{bmatrix}$$

where x , y and z are the coordinates of the considered nucleus and r_i is the distance from the atom i of the peridinin chain to the nucleus. The individual hyperfine interaction matrices were then summed with weights defined by the normalized spin density on each individual atom of the peridinin chain calculated with ORCA [54]. The resulting total hyperfine interaction matrix was diagonalized in order to find the principal values and the principal axis system. The Euler angles defining the orientation of the hyperfine interaction tensor with respect to the molecular frame, chosen as the coordinates of the optimized geometry, were then computed. This procedure was implemented for the water molecule H₂O 701 in PCP in the Matlab® program HFITensor.m reported in the appendix.

A similar approach was employed for the evaluation of the contribution of matrix protons to the observed echo envelope modulation. In order to estimate the contribution of protons positioned at various distances from the peridinin chain, a series of “test protons” evenly distributed in the space around Per614 was considered. The components of the dipolar hyperfine interaction of these “test protons” at specified points in space were evaluated and hyperfine isosurfaces were calculated with a numerical method proposed in reference [66]. A three-dimensional grid was created in the space surrounding the peridinin molecule and the dipolar hyperfine interaction for a “test proton” positioned at each intersection point of this grid was calculated as explained above for the water protons. Three principal dipolar hyperfine interaction values were associated with each grid point. In previous works, the intermediate component of the dipolar hyperfine interaction tensor, T_{mid} , was found to have the main influence on the ESEEM spectrum, regardless of the degree of rhombicity of the hyperfine tensor [65,66]. Hence this parameter was chosen to compute hyperfine isosurfaces in order to evaluate the magnitude of the hyperfine interaction for matrix protons at different distances from the peridinin molecule. Additionally, for each grid point the rhombicity of the corresponding hyperfine interaction tensor was calculated. The rhombicity of the dipolar hyperfine interaction tensor is defined as:

$$\chi = \frac{|(T_{min} - T_{mid})|}{T_{max}}$$

where T_{min} is the smallest component of the dipolar hyperfine interaction and T_{max} is the largest component. This procedure was implemented for the peridinin molecule 614 in PCP in the

Matlab® program HFIsocontourPer614.m reported in Appendix (A1).

The nuclear quadrupole interaction parameters of e^2qQ and η of the deuterium nuclei of deuterated water used in the simulations were those reported in a nuclear quadrupole resonance study on isotopically enriched Ice II [67]. The principal axis of the nuclear quadrupole tensor of ^2D in deuterated water was assumed to be directed along the O-D bond and the Euler angles with respect to the molecular frame were calculated accordingly.

7.2 RESULTS

7.2.1 GEOMETRY OPTIMIZATIONS

7.2.1.1 DFT GEOMETRY OPTIMIZATIONS

Density functional theory (DFT) geometry optimizations were performed on the molecules of the protein-pigment cluster relevant to the object of the present study, this included the peridinin molecule, whose triplet state is detected in the EPR experiments, the chlorophyll molecule, its partner in the triplet-triplet energy transfer, the water molecule, which is interposed between these two molecules and the histidine residue hydrogen-bonded to the water molecule.

The compatibility of the optimized geometries with experimental echo-detected EPR data of the antenna complex was tested by simulation of the triplet state EPR spectra of Per614 on the basis of the optimized structure as explained in Materials and Methods. In the framework of spin angular momentum conservation, the triplet state sublevel populations, determining the polarization of the calculated spectrum, depend on the squared cosines of the angles between the Per614 and Chl601 ZFS axes. This method is thus highly sensitive to the relative orientation of the peridinin and chlorophyll molecules and therefore useful for the validation of the geometry optimized structures.

Initially the geometry optimization was performed with no constraints using two different hybrid functionals, B3LYP and PBE0. The results obtained with the two functionals are similar, proving that they are both adequate for the description of the system.

The structures obtained in the full optimizations are represented in Fig. 7.1 in comparison with the X-ray structure, together with EPR spectra of the peridinin triplet state calculated based on these structures. The comparison of the structures reveals a variation of the relative orientation between the chlorophyll ring and the peridinin molecule and a pronounced curvature of the peridinin chain, furthermore the unconstrained histidine residue has moved away from chlorophyll, changing the position of the hydrogen-bonded water molecule accordingly. The RMSD (Root Mean Square Deviation) values calculated for the non-hydrogen atoms are reported

beneath the structures in Fig. 7.1. The change of the relative orientation of the two molecules leads to a different orientation of their ZFS axes and the curvature of the conjugated chain of peridinin causes a change in its ZFS axes directions, which both determine a variation of the relative triplet sublevel populations and thus of the triplet state EPR spectrum.

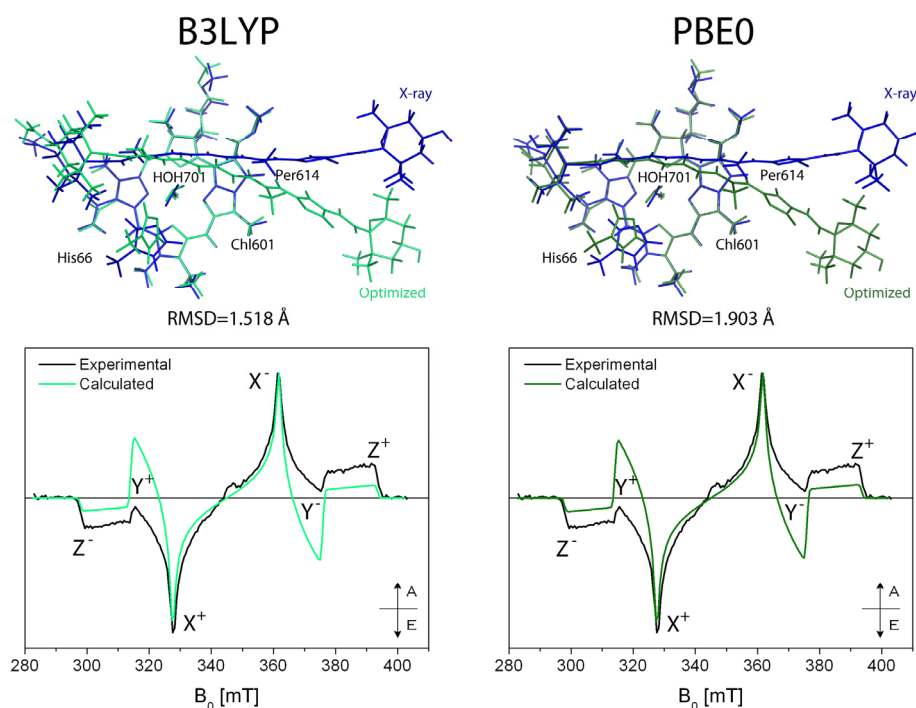


Fig. 7.1 Comparison between the X-ray structure and the structures obtained from full optimizations with the B3LYP and PBE0 functionals with superimposed chlorophyll rings and comparison of the experimental two-pulse echo-detected EPR spectra of the PCP complex ($T=20\text{K}$, $\nu=9.72\text{ GHz}$) and the triplet state EPR spectra calculated based on the two structures. (A=absorption, E=emission).

In an attempt to improve the agreement with the spectroscopic and structural data, constraints were introduced in the geometry optimizations. A first constrained optimization was performed by fixing the atoms of the histidine residue, based on the consideration that being part of an α -helix its movement would be restrained, and four dihedral angles in order to retain the orientation of the chlorophyll ring of the X-ray structure. The addition of these constraints lead only to a slight improvement of the correspondence between calculated and experimental data, but the peridinin molecule still showed a curvature as in the previous optimizations (Fig. 7.2 A).

In view of this result the X-ray structure was analyzed in detail in order to identify amino acids that would constrain the peridinin molecule to assume an extended conformation. Two residues, Gly78 and Glu101, that could form hydrogen bonds with atoms of the polar head groups of the peridinin molecule, and two residues, Ile96 and Gln150, that would prevent a change of conformation as obtained in the previous calculations by steric hindrance, were chosen to be

considered in the geometry optimization. A geometry optimization with fixed dihedral angles and with His66 and four additional amino acids with fixed coordinates was performed. The resulting optimized structure and the calculated triplet state spectrum are reported in Fig. 7.2 B.

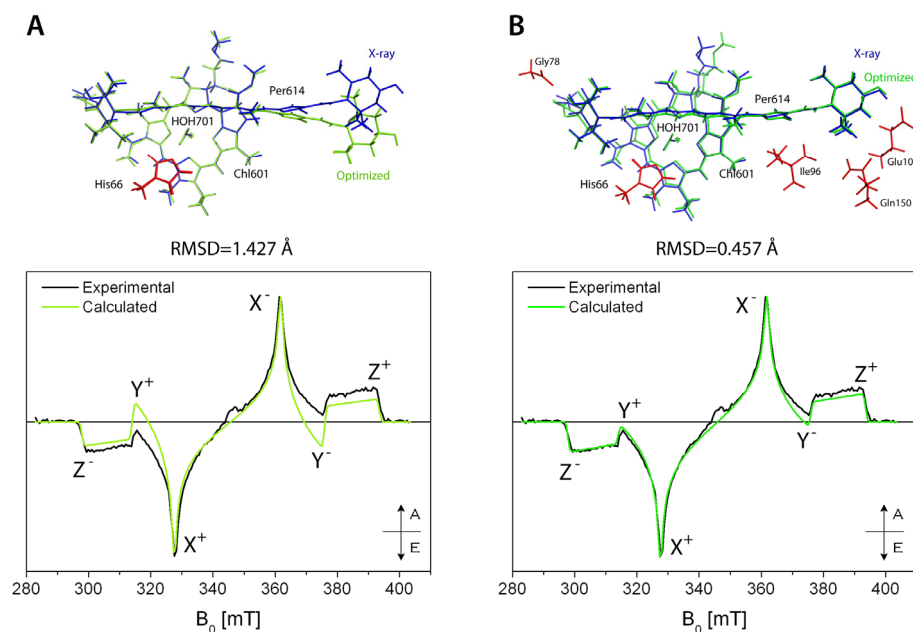


Fig. 7.2 Comparison between the X-ray structures and the structures optimized with PBE0 for fixed amino acids (depicted in red) and fixed dihedral angles and comparison of the experimental echo-detected EPR spectra of the PCP complex and the triplet state EPR spectra calculated based on the two structures. (A=absorption, E=emission).

The structure resulting from the geometry optimization with the additional amino acids is very close to the X-ray structure and the triplet state EPR spectrum calculated for this structure is in excellent agreement with the experimental spectrum, as shown in Fig. 7.2 B. This last geometry optimization thus allowed the determination of the position and orientation of the protons of the water molecule H₂O 701, not defined in the X-ray structure, in an overall optimized structure obtained with a limited number of artificial constraints and in agreement with experimental X-ray diffraction and EPR data.

7.2.1.2 ONIOM GEOMETRY OPTIMIZATIONS

Additional ONIOM calculations were performed in order to consider the structural effects of the protein environment without the introduction of artificial constraints. ONIOM is a hybrid method that allows considering different layers of a large molecular system at different levels of accuracy. The inner layer is optimized with high precision at DFT level, while the outer layer is considered at molecular mechanics level. The core layer in the ONIOM calculations on the system under study

was defined like in the previous geometry optimizations as the peridinin, chlorophyll, histidine and water molecule. The outer layer was defined in different calculations by the following portions of the surrounding protein structure:

- amino acids and pigments up to a distance of 4 Å from the peridinin and chlorophyll molecules (Fig. 7.3 A);
- amino acids and pigments up to a distance of 4 Å from the peridinin and chlorophyll molecules and amino acids of the α -helix containing the histidine residue (Fig. 7.3 B);
- complete NH_2 -terminal half of the PCP monomer (Fig. 7.3 C).

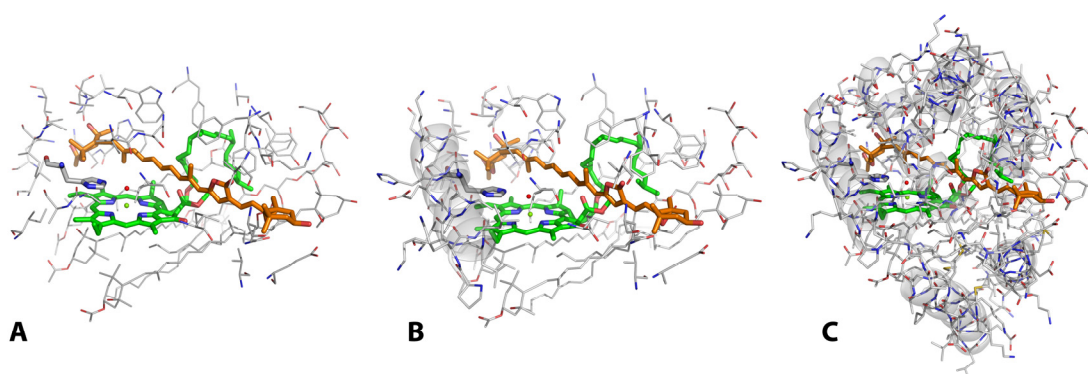


Fig. 7.3 Input structures for the ONIOM calculations with different portions of the protein included: (A) molecules up to a distance of 4 Å from the peridinin and chlorophyll molecules, (B) molecules up to a distance of 4 Å and α -helix containing His66, (C) whole NH_2 -terminal domain of the monomer. The molecules of the core layer are represented as sticks; the outer layer is represented as grey lines.

The first calculation considered all molecules up to a distance of 4 Å from the chlorophyll and peridinin molecule in the outer layer (A) and the triplet state EPR spectrum calculated on the basis of the resulting structure agreed well with the experimental data (Fig. 7.4 A). The relative orientation of the peridinin and chlorophyll molecule in the optimized geometry is thus in agreement with the experiment, even though the peridinin molecule is at a slightly greater distance from the chlorophyll ring with respect to the X-ray structure. However, it was observed that the unconstrained histidine residue moved considerably, thus changing the orientation of the water molecule.

In an attempt to limit the movement of the histidine residue in the optimizations, while still retaining the relative orientation between the peridinin and chlorophyll molecules obtained in the previous ONIOM optimization, an optimization including the complete α -helix containing His66, in addition to the molecules of the first optimization was performed (B). In this computed geometry the relative orientation of peridinin and chlorophyll remained practically unchanged

with respect to the X-ray structure, as in the optimization considering the amino acids up to a distance of 4 Å, leading to a good correspondence with the experimental EPR data (Fig. 7.4 B). The histidine residue did not move significantly with respect to the X-ray structure, especially the position of the N_{ϵ} coordinated to the water molecule remained nearly unchanged. In this optimized structure, a slight movement of the peridinin molecule away from the chlorophyll ring, though maintaining the relative orientation, was observed as in the previous optimization with the amino acids up to a distance of 4 Å (A).

In a subsequent ONIOM calculation the whole NH_2 -domain of the monomer was considered in the outer layer (C). Surprisingly, the agreement between the calculated and experimental spectra did not improve (Fig. 7.4 C), since the peridinin molecule moved away considerably from the chlorophyll ring, thereby changing its orientation with respect to the chlorophyll ring.

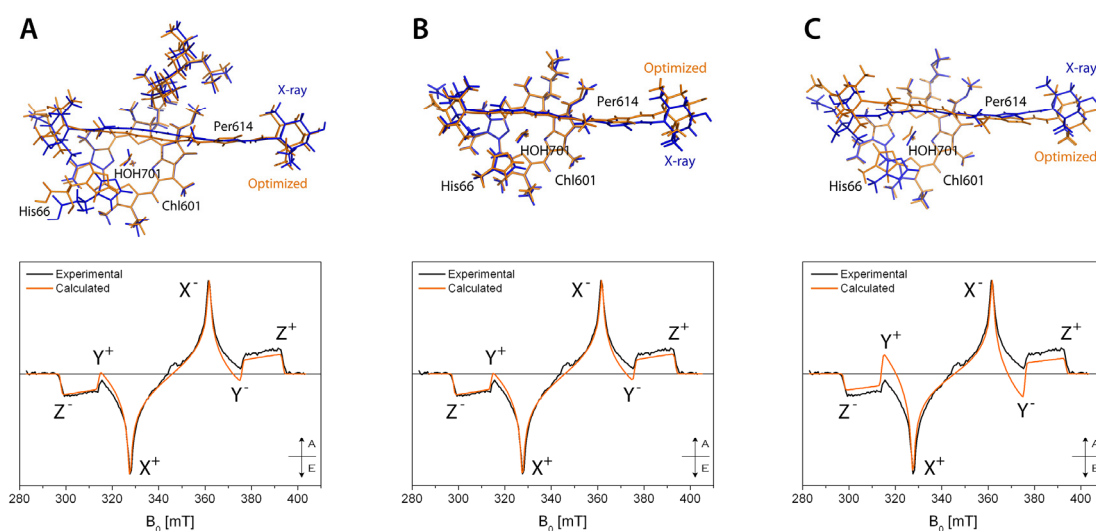


Fig. 7.4 Comparison between the X-ray structures and the structures optimized with ONIOM (B3LYP/6-31G(d):UFF) considering the molecules up to a distance of 4 Å from the pigments (A), the molecules up to a distance of 4 Å and the α -helix containing His66 (B) and the whole NH_2 -terminal domain of the monomer (C) in the outer layer and comparison of the experimental echo-detected EPR spectra of the PCP complex and the triplet state EPR spectra calculated based on the three structures. The chlorophyll rings of the X-ray and optimized structures are aligned for better comparison. (A=absorption, E=emission).

In all the geometry optimizations the water molecule H_2O 701 was coordinated to the Mg ion of Chl601 and one hydrogen atom was coordinated to the N_{ϵ} -atom of histidine, while the other hydrogen atom pointed towards the peridinin chain. The exact orientation and position of the water molecule H_2O 701 with respect to the peridinin chain differed slightly in the different optimized structures, but always maintained the same structural motif described above.

7.2.2 CALCULATION OF HYPERFINE INTERACTION PARAMETERS

The hyperfine interaction parameters can be determined computationally, in which case both the isotropic and the dipolar part of the hyperfine interaction of a nucleus with the paramagnetic system are obtained, or calculated based on the point-dipole approximation. The multi-nuclear point-dipole approximation, described in Materials and Methods, allows the determination of the dipolar hyperfine interaction parameters on the basis of a certain structural arrangement of the coupled nucleus with respect to the peridinin molecule and requires the knowledge of the spin density distribution of the triplet state of Per614.

Based on the geometry optimization results reported in the previous sections, the following three computed geometries were chosen as model structures for the interpretation of the ESEEM data due to their excellent agreement with experimental EPR data:

- structure calculated at PBE0 level with four additional fixed amino acids (AA) in the following referred to as “Fixed AA PBE0 structure”;
- ONIOM structure with amino acids and pigments up to a distance of 4 Å from Per614 and Chl601 in the following referred to as “4 Å ONIOM structure”;
- ONIOM structure with amino acids and pigments up to a distance of 4 Å and with the complete α -helix containing His66 in the following referred to as “4 Å + helix ONIOM structure”.

The spin densities and hyperfine parameters were calculated for these geometries and used for the simulation of the experimental ESEEM data.

7.2.2.1 SPIN DENSITY

The spin density corresponding to the peridinin triplet state was calculated for the three above-mentioned geometries and was found to be consistent among them. The spin density of the peridinin triplet state is drawn in Fig. 7.5 for the “Fixed AA PBE0 structure”.

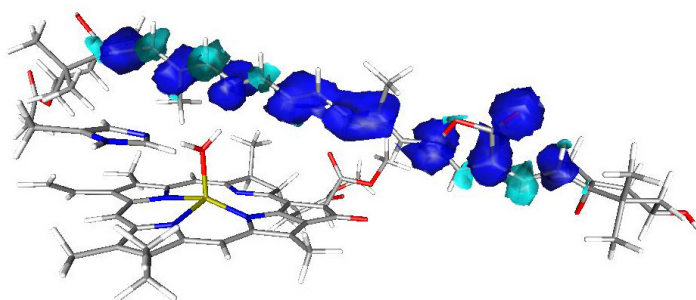


Fig. 7.5 Computed spin density (B3LYP/EPRII) for the triplet localized on Per614 for the “Fixed AA PBE0 structure”.

The DFT calculations show that the spin density is delocalized over the whole conjugated chain of the peridinin molecule, with positive spin densities alternating with smaller negative spin densities (Fig. 7.6). The odd-alternant pattern is lost in the central region of the conjugated chain, where positive spin densities prevail. This result is in accordance both with previous calculations on the peridinin and lutein triplet states in antenna complexes [13,68,69] and with the results of DFT studies on several carotenoid radical cations [70,71].

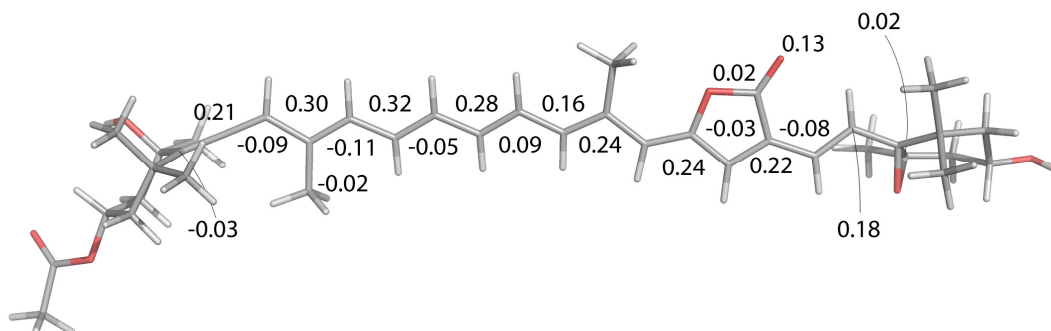


Fig.7.6 Spin densities computed at the B3LYP/EPRII level for the peridinin molecule in the “Fixed AA PBE0 structure”. Only spin densities with absolute values larger than 0.02 are represented. Similar values are obtained for the other two considered geometries.

The spin density calculations on the whole photoprotective site revealed a small but significant spin density on the oxygen atom of the water molecule. The spin density on this atom amounted to about $2 \cdot 10^{-3}$, depending on the considered model structure.

7.2.2.2 HYPERFINE INTERACTION PARAMETERS

The hyperfine coupling parameters for the hydrogen atoms of the water molecule were calculated using the B3LYP functional with the EPRII basis set in ORCA [54]. The EPRII basis set is specifically dedicated to the calculation of hyperfine couplings [57-59] and has proven to be generally accurate in EPR parameter calculations [72,73]. The hyperfine tensor is calculated in ORCA as a sum of three terms: the isotropic Fermi contact term, the electron spin-nuclear spin dipolar interaction and a second-order spin-orbit coupling term, which however is negligible for light nuclei.

In addition to that, the dipolar hyperfine interaction parameters were also calculated with the multi-nuclear point-dipole approximation as described in Materials and Methods.

The hyperfine parameters for the two protons of the water molecule obtained from the different sources are reported for comparison in Tables 7.1 and 7.2; the corresponding deuterium

hyperfine parameters can be derived considering the ratio of nuclear g values:

$$\frac{g_n(^1\text{H})}{g_n(^2\text{H})} = 6.51$$

The hyperfine interaction parameters calculated for the different structures are different on account of minor variations of the position and of the orientation of the water molecule with respect to the peridinin molecule, as depicted in Fig. 7.7.

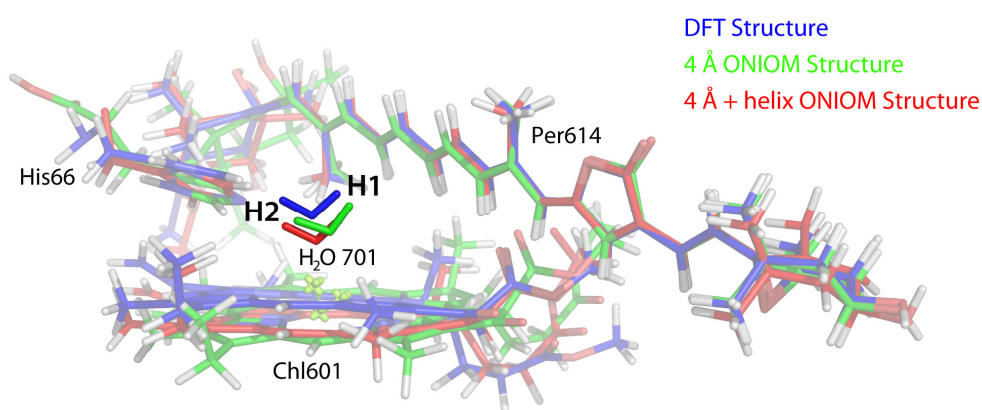


Fig. 7.7 Superposition of the three optimized geometries considered in the hyperfine interaction calculations with aligned Per614 chains. The water molecule assumes a different position and orientation with respect to the peridinin molecule in the three structures.

Table 7.1 – Hyperfine parameters for the water proton closest to Per614: H1 in Fig. 7.7

	"FIXED AA PBE0"		"4 Å ONIOM"		"4 Å+HELIX ONIOM"	
	point-dipole ^a	B3LYP/EPRII	point-dipole ^a	B3LYP/EPRII	point-dipole ^a	B3LYP/EPRII
T _{xx} (MHz)	-1.46	-1.88	-1.57	-1.85	-0.98	-1.08
T _{yy} (MHz)	1.67	2.30	1.57	1.78	1.10	1.14
T _{zz} (MHz)	-0.21	-0.42	-0.01	0.07	-0.12	-0.06
a _{iso} (MHz)		-0.56		-0.43		-0.13
χ ^b	0.75	0.64	0.99	0.93	0.79	0.89
α (°) ^c	-4	9	22	-152	49	54
β (°) ^c	54	57	93	85	99	98
γ (°) ^c	90	91	32	-29	-42	-43

^a Dipolar hyperfine tensor calculated by applying the multi-nuclear point-dipole approximation as explained in Materials and Methods.

^b Rhombicity calculated as $\chi = |(T_{\min} - T_{\text{mid}})| / T_{\max}$.

^c Euler angles defining the orientation of the HFI tensor with respect to the coordinate system of the computed geometry. The orientation of the ZFS tensor is defined by the following Euler angles: (-13°, 53°, 87°) for the "Fixed AA PBE0 structure"; (170°, 89°, -25°) for the "4 Å ONIOM structure"; (11°, 93° -36°) for the "4 Å +helix ONIOM structure".

Table 7.2 – Hyperfine parameters for the water proton coordinated to His66: H2 in Fig. 7.7

	"FIXED AA PBE0"		"4 Å ONIOM"		"4 Å+HELIX ONIOM"	
	Point-dipole ^a	B3LYP/EPRII	point-dipole ^a	B3LYP/EPRII	point-dipole ^a	B3LYP/EPRII
T _{xx} (MHz)	-0.53	-0.50	-0.58	-0.61	-0.47	-0.46
T _{yy} (MHz)	0.61	0.64	0.68	0.70	0.55	0.56
T _{zz} (MHz)	-0.08	-0.14	-0.10	-0.10	-0.08	-0.10
a _{iso} (MHz)		-0.04		-0.10		-0.05
χ ^b	0.73	0.57	0.72	0.72	0.71	0.64
α (°) ^c	-13	-19	-166	-169	39	37
β (°) ^c	56	47	90	100	103	104
γ (°) ^c	102	105	42	-42	-46	-44

^a Dipolar hyperfine tensor calculated by applying the multi-nuclear point-dipole approximation as explained in Materials and Methods.

^b Rhombicity calculated as $\chi = |(T_{\min} - T_{\text{mid}})| / T_{\max}$.

^c Euler angles defining the orientation of the HFI tensor with respect to the coordinate system of the computed geometry. The orientation of the ZFS tensor is defined by the following Euler angles: (-13°, 53°, 87°) for the "Fixed AA PBE0 structure"; (170°, 89°, -25°) for the "4 Å ONIOM structure"; (11°, 93° -36°) for the "4 Å +helix ONIOM structure".

The comparison of the hyperfine interaction parameters for the two water protons shows that the water proton closer to the conjugated chain of peridinin (H1 in Fig. 7.7) is much more strongly coupled to the peridinin triplet state than the more distant water proton (H2 in Fig. 7.7).

The hyperfine interaction parameters calculated with the point-dipole approximation are close to the computationally determined values, confirming that the point-dipole approximation is valid for the considered distances. Minor differences can be attributed to the fact that the computations take into account also the spin density on the oxygen atom, which was neglected in the calculations with the multi-nuclear point-dipole approximation since the O-H bond distance is too small to apply the point-dipole approximation.

The dipolar hyperfine interaction parameters depend strongly on the distance between the coupled nucleus and the conjugated chain of Per614; they decrease slightly on going from the "Fixed AA PBE0" to the "4Å ONIOM structure" and are considerably smaller for the "4Å + helix ONIOM structure". The isotropic hyperfine interaction constants calculated for the three structures show the same trend.

The orientations of the hyperfine interaction tensors calculated with the two methods are in excellent agreement. By comparing the Euler angles describing the orientation of the hyperfine interaction tensor in the molecular frame with the Euler angles describing the orientation of the ZFS tensor it becomes clear that the Z axes are approximately collinear.

7.2.3 ESEEM SIMULATIONS

All the exchanged protons in the surroundings of the peridinin molecule contribute to the modulation depth. The exchangeable protons in the environment of the peridinin molecule Per614 responsible for photoprotection through TTET in the PCP antenna complex can be divided into four classes:

- exchangeable protons of the protein structure;
- exchangeable water molecules;
- exchangeable protons on the other pigment molecules of the protein complex;
- exchangeable protons on the peridinin molecule Per614 itself;
- exchangeable protons of the water molecule H₂O 701 at the interface between Per614 and Chl601.

The first three classes are considered as one and are referred to in the following as exchangeable matrix protons. The contribution to the modulation depth of the different classes of exchangeable protons will be considered separately in the following sections.

7.2.3.1 MATRIX PROTON CONTRIBUTIONS

The matrix protons include the exchangeable protons of the protein structure, of the pigment molecules and of distant water molecules in the environment of Per614 in PCP. The water molecule at the interface between Per614 and Chl601 will be considered separately later on. To evaluate whether or not the matrix contributions alone could explain the observed modulations, the exchangeable protons in the surroundings of Per614 were identified in the X-ray structure and considered in simulations of the ESEEM time trace. The exact calculation of the ESEEM time trace in a disordered system with several nuclei interacting with the paramagnetic centre requires the solution of the following integral:

$$\langle V_N(\tau) \rangle_{\theta, \varphi} = \frac{1}{4\pi} \int_0^\pi \sin \theta d\theta \int_0^{2\pi} \prod_{i=1}^N V_i(\tau, \theta, \varphi) d\varphi$$

The exact calculation for disordered systems is computationally expensive since the product rule has to be applied before performing the powder average. Additionally the orientation of the hyperfine interaction tensor has to be defined for each nucleus. The evaluation of the matrix contributions is greatly simplified by employing the spherical model [74]. The spherical model is based on the assumption that the mutual orientations of the hyperfine tensors are uncorrelated; hence the powder average can be performed prior to the application of the product rule, which is

equivalent to considering an average modulation for nuclei randomly distributed on a sphere with a certain radius r . An alternative approximation consists in considering the same angle θ for all nuclei. These simplifications are justified by the observation that for $r \geq 2.5-3 \text{ \AA}$ at X-band, the ESEEM signal depends only on the number of nuclei and on the distance from the electron spin, whereas the exact geometrical arrangement does not affect it significantly [28].

The spherical model as defined above is not realistic in the present case, given the elongated spin density distribution of the peridinin triplet state, thus a slightly different approach is proposed in the present thesis work: the modulations are averaged for nuclei randomly distributed on a hyperfine isosurface rather than on a sphere. The dipolar hyperfine interaction isosurfaces were computed with a numerical method described in Materials and Methods, considering the middle-valued component of the hyperfine interaction tensor as the most significant in terms of its influence on the deuterium ESEEM patterns [65,66]. In Fig. 7.8 (A) the three-dimensional isosurfaces of T_{mid} are represented with respect to the peridinin molecule; Fig. 7.8 (B) contains a two-dimensional slice through the three-dimensional isosurfaces on the plane of the conjugated chain of Per614. All the matrix protons, belonging to amino acid residues, to water molecules or to the other pigment molecules, contained on a specific isosurface, give a contribution to the ESEEM determined by the hyperfine interaction value corresponding to that isosurface.

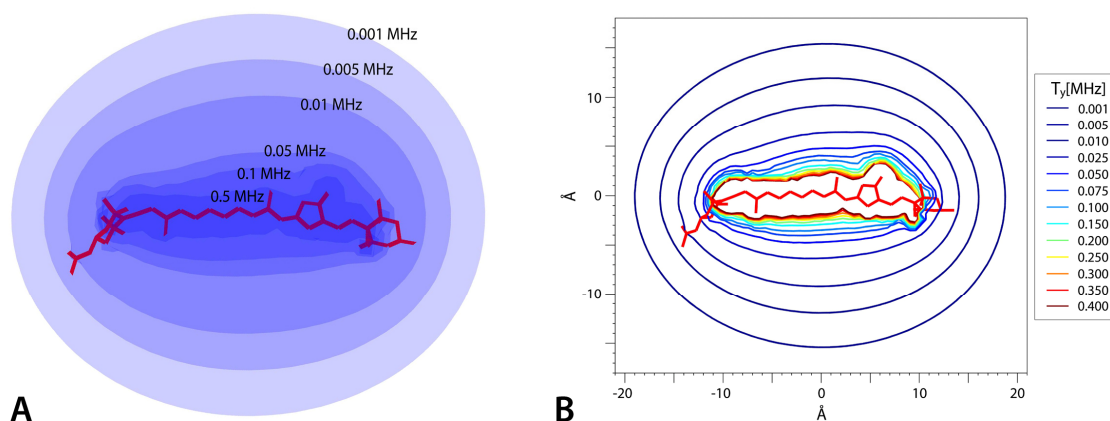


Fig. 7.8 Hyperfine isosurfaces and isosurface slice of the middle-valued hyperfine interaction component for the peridinin molecule Per614 in PCP.

The exchangeable hydrogen atoms surrounding the peridinin molecule Per614 up to a distance of 15 \AA were identified in the X-ray structure after the addition of the hydrogen atoms with AutoDockTools and were assigned to a particular isosurface. The corresponding echo envelope modulation was simulated with *Easyspin* assuming an axial hyperfine interaction with $T=T_{\text{mid}}$ and the contributions of the different nuclei were summed according to the product rule. Most of the

exchangeable protons identified in the close environment of Per614 are positioned outside the 0.01 MHz isosurface.

The hyperfine tensor rhombicities χ are displayed in the contour plot in Fig. 7.9 with respect to the peridinin molecule. According to these results, the hyperfine tensor rhombicity would be small for most of the exchangeable protons identified in the environment of Per614; hence the approximation introduced in assuming an axial hyperfine interaction is valid.

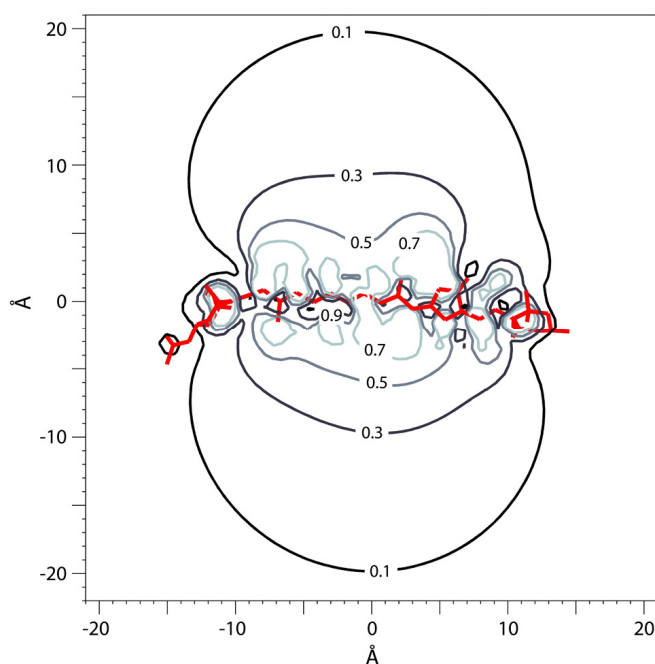


Fig.7.9 Hyperfine rhombicity isocontours on a plane containing the conjugated chain of the peridinin molecule.

The rhombicity is calculated as $\chi = |(T_{\min} - T_{\text{mid}})| / T_{\max}$.

The ESEEM simulations resulting from this modified spherical model analysis are reported in Fig. 7.10. While the exchangeable protons of the protein matrix are well accounted for with this procedure, the water molecules present in the X-ray structure are not necessarily in the same position and of the same number as in the sample used for the measurement. However, it was observed that the pigments are contained in a hydrophobic cavity and the closest possible approach for non-coordinated water molecules is of 10 Å, which corresponds to a negligible modulation depth.

The simulated modulation depths for the matrix proton contributions are too small to reproduce the experimental modulations in both the two-pulse and the three-pulse ESEEM experiment. Therefore, the matrix contributions can be excluded as the main source of the experimentally observed echo envelope modulations.

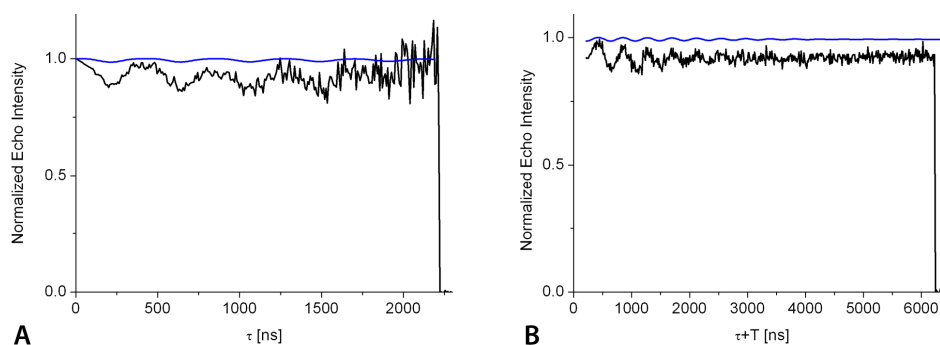


Fig. 7.10 Two- (A) and three-pulse (B) ESEEM echo envelopes calculated for matrix protons with the modified spherical model approximation explained in the text and assuming all exchangeable matrix protons to be substituted by deuterium. The simulated data are compared with the experimental echo envelopes recorded at the X⁻ field position (362 mT).

7.2.3.2 EXCHANGEABLE PROTONS ON THE PERIDININ MOLECULE

The peridinin molecule Per614 itself has two hydroxyl groups in the external rings, which could be exchanged with deuterons and cause the observed modulation of the spin echo envelope. This has been verified by calculating the hyperfine tensor for these nuclei with the multi-nuclear point-dipole approximation as described in section 7.1.3 and by simulating the corresponding ESEEM signal. An approximately axial hyperfine tensor was obtained for both deuterium atoms with $T_1=0.05$ and $T_2=0.01$ MHz. The corresponding ESEEM simulations are reported in Fig. 7.11. The modulation depth of the simulated time trace is much smaller than the experimental modulation depth.

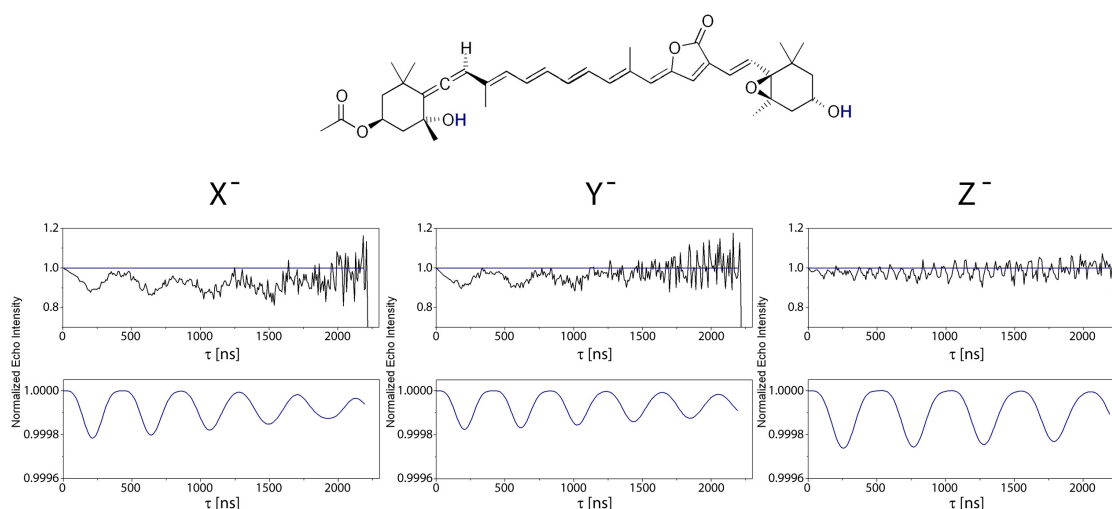


Fig. 7.11 Molecular structure of peridinin with highlighted exchangeable protons, comparison of the experimental and simulated two-pulse ESEEM time traces at the X⁻, Y⁻ and Z⁻ field positions and close-up of the simulated time traces.

The very weak interaction of the exchangeable protons on the peridinin molecule with the spin density localized on the conjugated chain of the molecule itself could also be deduced from the isosurfaces in Fig. 7.8. The head groups of the peridinin molecules are outside the isosurfaces defining strong hyperfine interactions with the peridinin triplet state.

7.2.3.3 WATER MOLECULE H₂O 701

The results of the analysis of exchangeable protons in the environment of Per614 lead to the conclusion that the observed modulations must be due to the water molecule H₂O 701, positioned at the interface between Per614 and Chl601. In order to determine the position and orientation of this water molecule in the PCP complex, simulations with hyperfine interaction parameters calculated at B3LYP/EPRII level for different model structures were compared with the experimental ESEEM data. The hyperfine interaction parameters calculated at DFT level were also used as starting values for simulations aimed at optimizing the agreement with experimental data.

The simulated and experimental two-pulse and three-pulse ESEEM time traces are compared in terms of modulation depth and modulation damping, which are the main sources of information on the observed hyperfine interaction in the case of weakly coupled nuclei. The qualitative evaluation of the modulation depth and the modulation damping characterizing an ESEEM time trace is illustrated in Fig. 7.12.

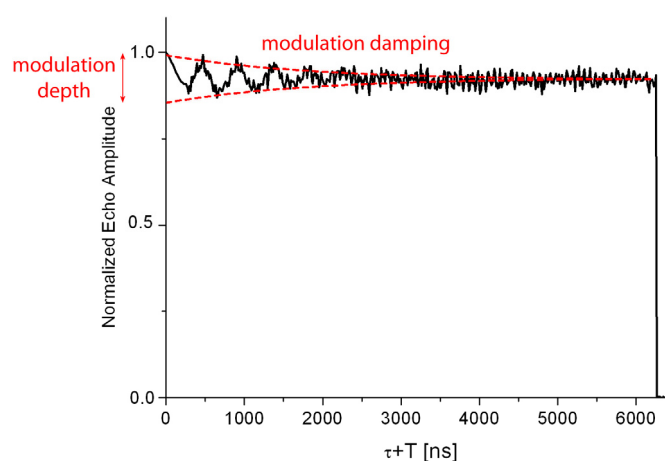


Fig. 7.12 Illustration of the concepts of modulation depth and modulation damping of an ESEEM time trace.

The modulation depth depends on the strength of the hyperfine interaction and on the number of interacting nuclei. In systems with orientation selection there is an additional dependence on the relative orientation of the hyperfine interaction tensor with respect to the ZFS tensor in the case of a triplet state system. The modulations vanish at the canonical orientations of the

hyperfine tensor, i.e. when the external magnetic field is directed along a principal axis of the hyperfine tensor. The modulation damping is the attenuation of the modulations in time, depending on the strength of the hyperfine interaction and on the number of coupled nuclei. The damping is faster for close, more strongly coupled nuclei, while the presence of several distant, weakly coupled nuclei leads to a slow damping of the modulations. In the frequency domain, the agreement between the simulations and the experiment is evaluated considering the position, intensity and line-width of the peaks.

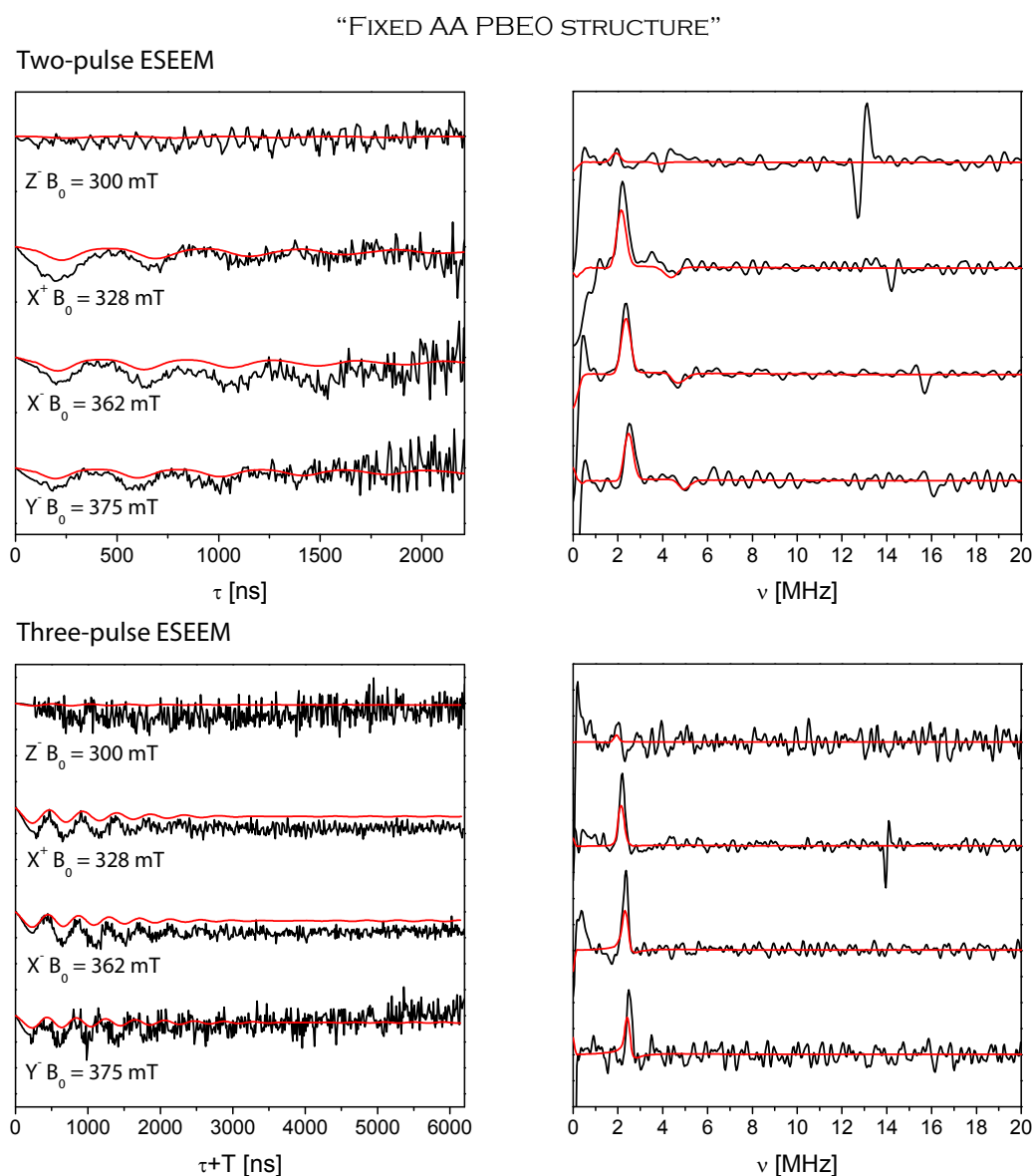


Fig. 7.13 Experimental two- and three-pulse ESEEM time traces and FFT spectra (black) and corresponding simulations (red) for the water molecule H_2O 701 at the interface between Per614 and Chl601 in the “Fixed AA PBE0 structure” at the Z^- , X^+ , X^- and Y field positions. The HFI parameters used in the simulations are calculated at the B3LYP/EPRII level and are reported in Tables 7.1 and 7.2 for hydrogen nuclei, the other simulation parameters were chosen as described in Materials and Methods (section 7.1.3). The experimental data was collected at 20K and at a microwave frequency of 9.72 GHz; additional experimental parameters are reported in chapter 6.

The first considered model is the “Fixed AA PBE0 structure” obtained in a constrained geometry optimization with the PBE0 functional; the positions of four amino acid residues, in addition to the His66 residue, were fixed, as well as four dihedral angles involving the chlorophyll ring. The ESEEM time traces and spectra simulated with the B3LYP/EPRII hyperfine parameters reported in Tables 7.1 and 7.2 for this structure are represented in Fig. 7.13. The simulations are compared with the corresponding experimental two- and three-pulse ESEEM data.

The experimental ESEEM data and the simulations show modulations at the same frequency, corresponding to the deuterium Larmor frequency at the considered magnetic field position. Both the experimental time traces and the simulations lack modulations at the magnetic field position corresponding to the Z^- canonical transition. At the other field positions the modulation depth in the simulations is shallower than experimentally observed. The modulation damping in the experimental and simulated ESEEM time traces is comparable. The agreement of the simulated and experimental spectra in the frequency domain is good as far as the positions and line-widths are concerned, the different intensity is due to the smaller modulation depth in the simulated time traces.

Another model structure is the “4 Å ONIOM structure”, obtained in an ONIOM calculation considering the molecules around Per614 and Chl601 up to a distance of 4 Å in the outer level. The inner level, defined by the peridinin, chlorophyll and water molecules and the hydrogen-bonded histidine residue, was optimized at B3LYP level without constraints. The ESEEM time traces and spectra simulated with the hyperfine parameters calculated at B3LYP/EPRII level for this structure are reported in Fig. 7.14 in comparison with the experimental two- and three-pulse ESEEM data recorded at different magnetic field positions.

The simulations with the hyperfine parameters calculated at B3LYP/EPRII level for the “4 Å ONIOM structure” agree with experiment as far as modulation frequencies are concerned. The simulated modulation depth however is smaller than experimentally observed. The simulations at the Z^- field position are characterized by the absence of modulations like the corresponding experimental ESEEM traces. The modulation damping in the simulated time traces is in agreement with experiment.

The last considered model structure is the “4 Å + helix ONIOM structure”, obtained in an ONIOM calculation with an outer layer containing the molecules up to a distance of 4 Å from the Per614 and Chl601 molecules and the complete α -helix, of which the His66 residue is part. The simulations based on the hyperfine parameters calculated at B3LYP/EPRII level are reported in Fig. 7.15 comparison with the experimental two- and three-pulse ESEEM data.

The ESEEM simulations with the hyperfine interaction parameters calculated at B3LYP/EPRII level for the “4 Å + helix ONIOM structure” show much shallower modulations than the experimental time traces; however the frequency of the modulations is in agreement with experiment. The absence of modulations at the Z⁻ field position is correctly reproduced by the simulations.

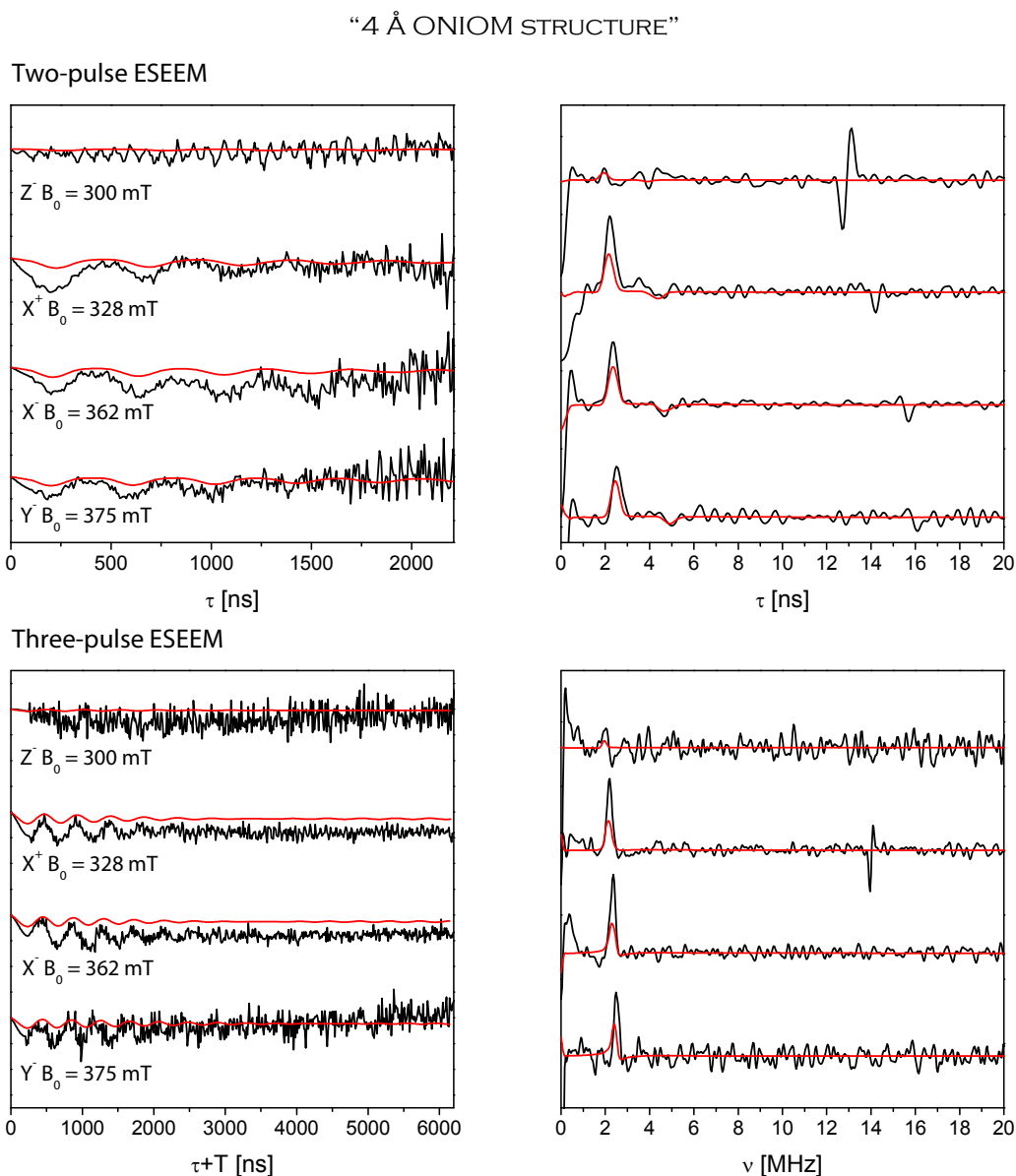


Fig. 7.14 Experimental two- and three-pulse ESEEM time traces and FFT spectra (black) and corresponding simulations (red) for the water molecule H₂O 701 at the interface between Per614 and Chl601 in the “4 Å ONIOM structure” at the Z, X⁺, X⁻ and Y field positions. The HFI parameters used in the simulations are calculated at B3LYP/EPRII level.

“4 Å + HELIX ONIOM STRUCTURE”

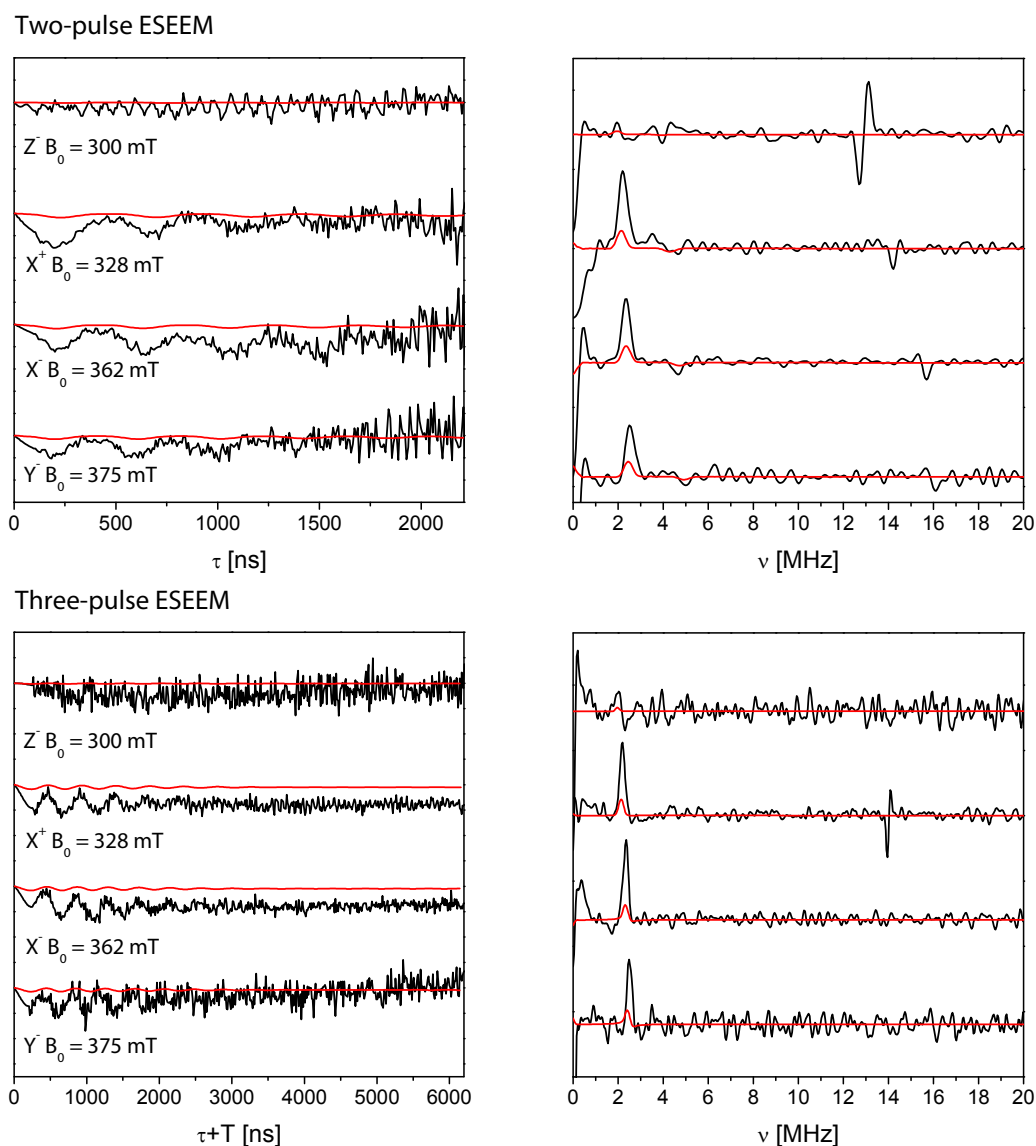


Fig. 7.15 Experimental two- and three-pulse ESEEM time traces and FFT spectra (black) and corresponding simulations (red) for the water molecule H₂O 701 at the interface between Per614 and Chl601 in the “4 Å + helix ONIOM structure” at the Z-, X⁺, X⁻ and Y- field positions. The HFI parameters used in the simulations are calculated at B3LYP/EPRII level.

The hyperfine interaction of the water proton closer to the peridinin molecule (H1 in Fig. 7.7) is considerably stronger with respect to that of the more distant water proton coordinated to His66 (H2); hence the observed modulations are mainly due to the former, while the contribution of the latter is only small.

In addition to the simulations based on a particular orientation of the water molecule as obtained from the geometry optimizations, simulations considering a distribution of different orientations [75] of the water proton closest to peridinin (H1 in Fig. 7.7) on a cone were also performed,

resulting in an even shallower modulation depth (data not shown). This result confirms that the water molecule assumes a specific orientation as indicated by the geometry optimizations rather than a distribution of different orientations.

The analysis of the exchangeable protons in the environment of the Per614 triplet state in PCP showed that these protons are not responsible for the experimentally observed modulations. However, they are expected to contribute somewhat to the modulation depth observed in the experimental spectra. For this reason, the ESEEM produced by the interaction between the protons of the water molecule and the peridinin triplet state and the ESEEM due to the matrix deuterium nuclei, calculated with the modified spherical model, were added according to the product rule and the results are reported for a single field position for the “Fixed AA PBE0 structure” in Fig. 7.16.

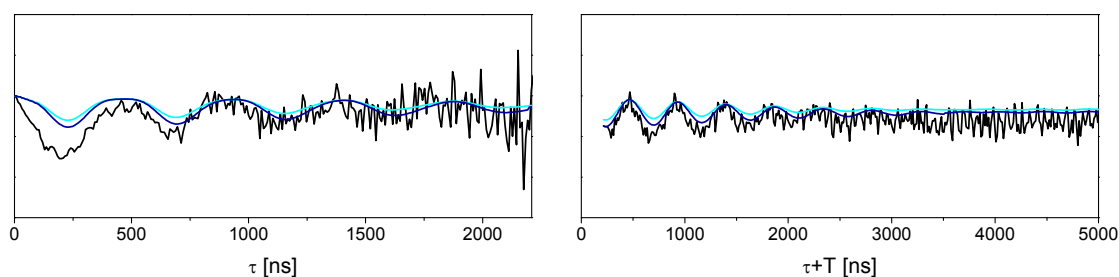


Fig.7.16 Experimental two-pulse (left) and three-pulse (right) ESEEM time traces (black) at the X^+ (328 mT) field position, corresponding simulated time traces (cyan) for the “Fixed AA PBE0 structure” and simulations taking into account also the contribution of matrix protons (blue) with the modified spherical model.

The addition of the matrix proton contribution leads to a small increase in modulation depth and to a slower damping of the modulations in time. The agreement with experimental data does not improve significantly by taking the matrix proton contributions into account. Similar results are obtained for the other two model structures.

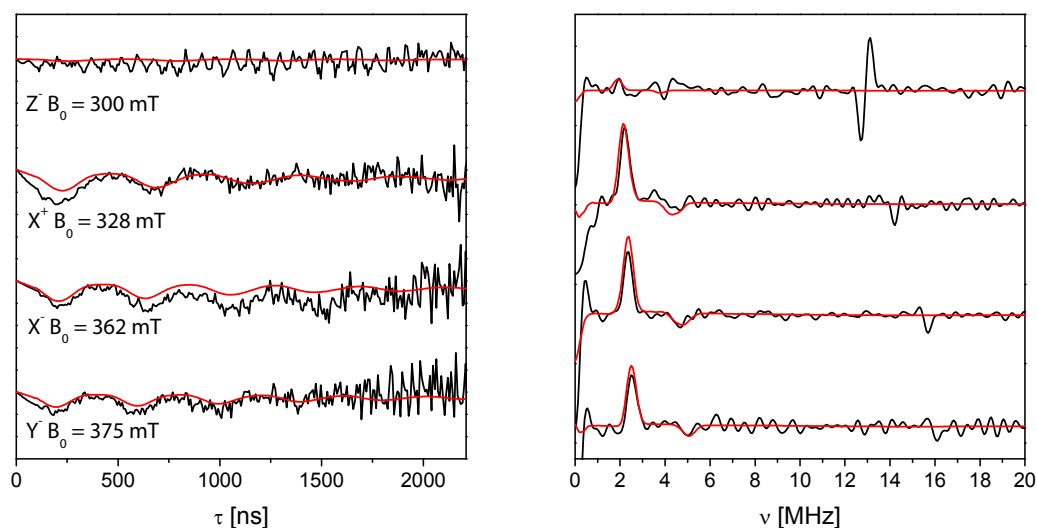
Since none of the hyperfine interactions calculated for the geometry-optimized structures are able to exactly reproduce the experimental data, simulations were also performed in order to optimize the agreement between experimental and simulated time and frequency domain data. The dipolar and isotropic hyperfine interaction parameters and the Euler angles defining the orientation of the hyperfine tensor were slightly varied from their initial values (Table 7.1 and 7.2) in order to correctly reproduce the modulation depth and modulation damping at all field positions and for both types of ESEEM experiments simultaneously. The proton hyperfine interaction parameters giving the best overall agreement with the experimental data are reported in Table 7.3. The corresponding simulations are compared with the experimental two- and three-pulse ESEEM data in Fig. 7.17.

Table 7.3 – Optimized hyperfine interaction parameters for two protons.

	SIMULATION PARAMETERS	
	H1	H2
T_{xx} (MHz)	-2.29	-0.56
T_{yy} (MHz)	2.81	0.74
T_{zz} (MHz)	-0.52	-0.18
a_{iso} (MHz)	-0.69	-0.05
α ($^\circ$) ^a	-10	-20
β ($^\circ$) ^a	53	50
γ ($^\circ$) ^a	90	100

^a Euler angles defining the orientation of the HFI tensor with respect to the coordinate system of the computed geometry. The orientation of the ZFS tensor is defined by the following Euler angles: (-13°, 53°, 87°).

Two-pulse ESEEM



Three-pulse ESEEM

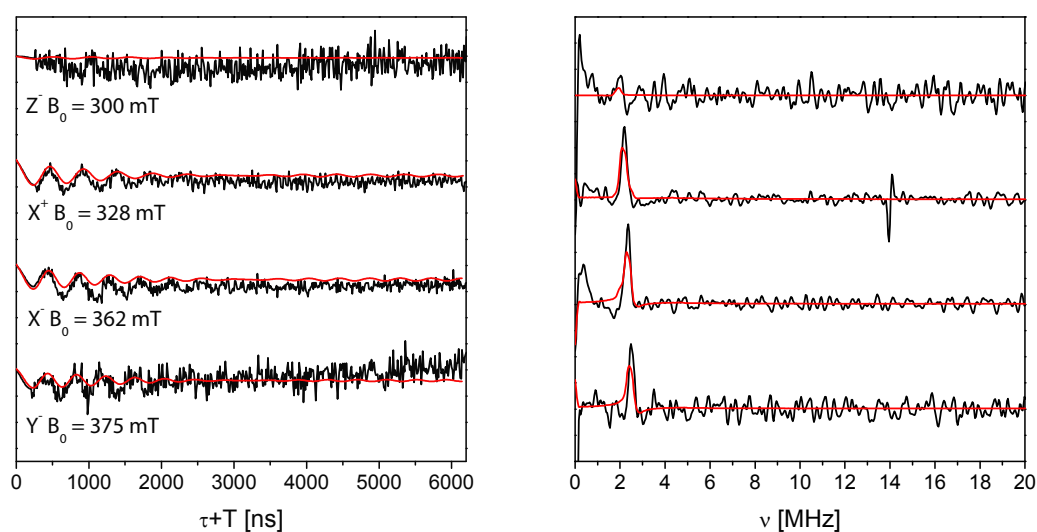


Fig. 7.17 Experimental two- and three-pulse ESEEM time traces and FFT spectra (black) and corresponding simulations (red) with the optimized hyperfine interaction parameters reported in Table 7.3 for hydrogen nuclei.

In the optimizations of the hyperfine interaction parameters, the modulation depth was slightly underestimated, since the matrix protons are expected to contribute. The addition of the matrix proton contributions calculated with the spherical model improves the agreement with experimental data, as can be seen for the X^+ field position in Fig. 7.18.

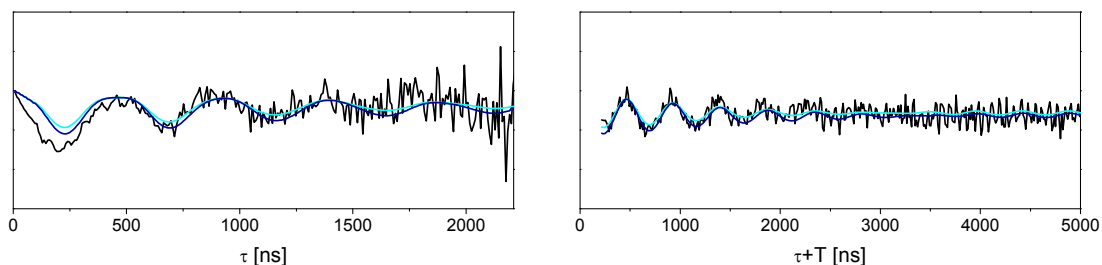


Fig.7.18 Experimental two-pulse (left) and three-pulse (right) ESEEM time traces (black) at the Y^- (375 mT) field position, corresponding simulated time traces (cyan) and simulations taking into account also the contribution of matrix protons (blue). The simulations were performed with the optimized hyperfine parameters as reported for hydrogen nuclei in Table 7.3.

7.3 DISCUSSION

7.3.1 STRUCTURE OF THE PHOTOPROTECTIVE SITE

In the present work ESEEM studies were performed with the purpose of studying the interaction of the peridinin triplet state with a water molecule (H_2O 701) positioned at the interface between Per614 and Chl601 in the PCP antenna complex. In previous studies this water molecule has been proposed acting as a bridge in the TTET occurring between chlorophyll and peridinin, since spin density calculations revealed that the oxygen atom of the water molecule is closest (~ 3.5 Å) to that atom of the conjugated peridinin chain bearing the highest spin density [13]. The ESEEM technique is applied to gather information about the geometry and electronic structure of the photoprotective site.

In order to correlate the ESEEM results with a particular structure of the photoprotective site, the simulation and interpretation of the ESEEM results was combined with DFT calculations. Quantum mechanical geometry optimizations were performed to define the probable structure of the photoprotective site in the PCP antenna complex, comprehensive of the hydrogen atoms absent in the X-ray structure. In particular, the geometry optimizations were aimed at defining the position and orientation of the water molecule. The resulting model structures were then used for a calculation of the hyperfine interaction parameters, which were compared with the experimental results.

The structures obtained with full optimizations were not satisfying models of the photoprotective site due to the excessive curvature of the peridinin molecule, the variation of the relative orientation of the Per614-Chl601 pair and the unconstrained movement of the histidine residue. The conformation of the peridinin molecule in the PCP complex has been the object of computational studies, which revealed that the approximately linear conformation of the conjugated chain, assumed by all the four peridinins in different binding sites inside a domain of the PCP protein complex, is the most stable [76,77]. The optimized structures with the pronounced curvature thus seem improbable, especially by considering that the amino acids of the protein complex would prevent it by steric hindrance. Moreover, a change in relative orientation of the peridinin and chlorophyll molecules appears unlikely, given that the protein complex has been reconstituted with several different chlorophyll molecules without significant changes of the structure of the pigment clusters [10]. This evidence points to the fact that the protein matrix has an important influence on the structure of the pigments and should be considered in the geometry optimizations in order to improve the agreement with the available structural and spectroscopic data.

The agreement improved considerably by taking into account also some selected residues of the protein environment. The structure resulting from the geometry optimization with the fixed histidine residue and four additional fixed amino acids is in excellent agreement with the echo-detected EPR spectra, which is highly sensitive to the orientation of the pigments, and is thus considered a valid model of the photoprotective site and was used in the simulation of the ESEEM data.

Since the DFT geometry optimizations showed the importance of the surrounding protein matrix in determining the conformation and relative orientation of the pigment molecules, ONIOM calculations were performed with the aim of considering the effect of the protein environment on the structure of the photoprotective site without imposing artificial constraints. Surprisingly the ONIOM optimization considering the whole monomer in the outer layer gave the worst correspondence with the experimental data, due to a significant increase of the distance between the chlorophyll and peridinin molecule accompanied by a reorientation of peridinin with respect to the chlorophyll ring. The structures obtained in the optimizations considering the residues at 4 Å, or both these residues and the complete α -helix containing the histidine residue, gave similar results as regards the relative orientation of the peridinin and chlorophyll molecules, and both structures are in good agreement with EPR data. However, in the optimization considering also the α -helix, the histidine residue, and particularly its N_ϵ atom hydrogen-bonded to the water molecule, is closer to their position as defined by the X-ray structure. The two geometries are also characterized by slightly different distances between peridinin and the water

molecule coordinated to chlorophyll. Both of these ONIOM geometries were chosen as model systems for the simulation of the ESEEM data.

The position and orientation of the water molecule were similar in all the computed geometries, demonstrating that a particular orientation is imposed by the interactions with the surrounding molecules. The determined Mg-O distances fall into the range of typical distances for water coordinated to porphyrin rings [78] and confirm the coordination of the water molecule to the Mg ion of the chlorophyll molecule. The position of one water proton is fixed by hydrogen-bond formation with the histidine residue and the second hydrogen atom was found to point towards the conjugated chain of peridinin. The different model structures are distinguished by slightly different orientations of the water molecule and by different positions of the water molecule with respect to the conjugated chain of peridinin on account of the different relative position of the chlorophyll ring and the peridinin molecule.

7.3.2 INTERPRETATION OF ESEEM RESULTS

The experimental ESEEM data indicates the presence of an interaction between the peridinin triplet state and exchangeable protons replaced by deuterium through H/D exchange. In the preceding chapter the experimental data was shown and qualitative considerations lead to the conclusion that the observed modulations were due to a small number of coupled nuclei. This is in favour of the attribution of the modulations to the water molecule at the interface between Per614 and Chl601. In order to unequivocally demonstrate that the interaction of the protons of this water molecule with the peridinin triplet state is the cause for the observed modulations, other possible sources have to be excluded first.

The ESEEM time traces obtained by envelope division of the experimental time traces collected for the deuterated and protonated sample contain modulations due to the exchangeable protons in the environment of the triplet state of peridinin. The treatment of the protein sample with deuterated water leads not only to the substitution of the protons of the water molecule with deuterium, but also of other exchangeable protons on the pigment molecules and of the protein.

Based on the results of the ESEEM simulations for exchangeable protons in the environment of Per614 in the PCP complex, it can be safely assumed that the observed modulations are not due only to matrix deuterons, since, even supposing all exchangeable protons to be substituted by deuterium nuclei, the simulated modulations are too shallow to reproduce the experimental data. A further indication of the fact that the experimentally observed modulations do not originate from distant matrix nuclei is that, while for these type of nuclei a slow damping of the

modulation amplitude is expected, the observed attenuation is quite pronounced. The absence of modulations in the ESEEM time trace collected at the Z' field position is another strong indication of the fact that the contribution to the modulations of matrix protons is small, since it is highly unlikely that all matrix protons would be characterized by a hyperfine tensor with one principal axis aligned with the ZFS Z axis of the peridinin triplet state.

The modulations arising from the hyperfine interaction of the exchangeable protons on the peridinin molecule itself are also too shallow to reproduce the experimental ESEEM time trace, hence it can be concluded that the exchangeable protons on the peridinin molecule can be excluded as the origin of the experimentally observed modulations of the spin echo envelope as well.

These results lead to the conclusion that the observed ESEEM is due to the interaction of the water molecule, H_2O 701, with the triplet state of Per614. The presence of this interaction is a confirmation of the significant role of the water molecule in the photoprotective site of the PCP antenna complex. The correlation of the hyperfine interaction parameters with an optimized structure of the photoprotective site allows the determination of the arrangement of the water molecule in the photoprotective site through comparison of simulated and experimental ESEEM data. The spectroscopic parameters further provide information on its electronic structure.

The presence of orientation selection in the case of the peridinin triplet state poses strict constraints on the simulations: one set of hyperfine interaction parameters has to correctly reproduce the ESEEM at all the considered field values. Orientation selection means that only spin systems with a particular orientation with respect to the external magnetic field are excited by a microwave pulse at a particular field position. The collection of ESEEM time and frequency domain data at different magnetic field values allows a more accurate determination of the relative orientation of the hyperfine interaction tensor of the coupled nuclei and the ZFS tensor of the peridinin triplet state. The absence of modulations in the experimental time trace at the Z' field position indicates that the hyperfine tensor of the nuclei interacting with the peridinin triplet state has one principal axis parallel to the ZFS Z axis of peridinin. This gives an important constraint on the orientation of the hyperfine tensor and a useful indication of the validity of the simulation parameters.

In addition to that, the hyperfine interaction parameters have to be in agreement both with two- and three-pulse experimental ESEEM data. Once a set of hyperfine interaction parameters correctly simulating the time and frequency domain data of two- and three-pulse ESEEM experiments at several magnetic field values has been found, it can be confidently concluded that the interaction is characterized by this set of parameters.

In the limit of weak interactions the information on the hyperfine coupling is contained almost exclusively in the modulation depth and in the modulation damping of the ESEEM time trace, since the modulation frequency is approximately equal to the nuclear Larmor frequency at the considered magnetic field. The FFT spectra are characterized by a single peak at the Larmor frequency and, in the two-pulse experiment, by an additional sum combination peak. Hence in the frequency domain the only information on the strength of the hyperfine interaction is contained in the line-width and the intensity of the peak. The information on the hyperfine interaction of the water molecule is thus extracted more easily by simulation of the time domain data.

In order to characterize the electronic structure of the photoprotective site containing the water molecule H₂O 701, simulations of the experimental ESEEM data were performed based on the three previously described model structures. The simulations with the hyperfine interaction parameters calculated at B3LYP/EPRII level are characterized by smaller modulation depths than the experimental ESEEM time traces for all three model structures. This remains true even if the matrix proton contributions are taken into account. The modulation depths are similar for the "Fixed AA PBE0" and "4 Å ONIOM structures", while they are significantly smaller for the "4 Å + helix ONIOM structure", where the water molecule is at a greater distance from the peridinin molecule (see Fig.7.7). The hyperfine interaction parameters calculated for all three structures lead to the absence of modulations at the Z' field position and are thus in agreement with experiment.

The best agreement between the simulations and the experimental data is obtained for the hyperfine parameters calculated for the "Fixed AA PBE0 structure". It can thus be concluded that the geometry and electronic structure of the photoprotective site in PCP is described quite well already at this level of theory. The results of the optimizations with the more sophisticated ONIOM method are more reliable due to the absence of artificial constraints and they confirm the results of the optimization at PBE0 level. The constraints imposed on the system in this geometry optimization might in principle induce the water molecule to assume a position and an orientation differing from those corresponding to the actual energy minimum for the system without constraints. The ONIOM results confirm both position and orientation of the water molecule and thus permit to unequivocally define the geometric arrangement of the water molecule in the photoprotective site. The electronic structure of the photoprotective site derived for the "Fixed AA PBE0 structure" can thus be considered accurate.

Even though the simulations with the hyperfine parameters calculated for the "Fixed AA PBE0 structure" agreed with the experimental data reasonably well, the modulation depths were still shallower than experimentally observed. Therefore the calculated hyperfine interaction

parameters were also used as starting values for an optimization of the hyperfine interaction parameters.

The dipolar and isotropic hyperfine interaction parameters were optimized starting from the calculated ones in order to correctly reproduce the modulation depths and the attenuation of the modulations at all four field positions and for both the two- and the three-pulse ESEEM experiment. The Euler angles describing the orientation of the hyperfine tensor with respect to the molecular frame were not changed significantly, since they were almost identical for the two methods employed for the determination of the hyperfine tensor. A further reason for maintaining the calculated orientation was that the absence of modulations at the Z field position, arising from the collinearity of one principal axis of the hyperfine tensor with the Z axis of the ZFS tensor, was correctly reproduced with the calculated Euler angles. The hyperfine interaction parameters resulting from the optimization procedure are about 20% greater than the initial parameters calculated at DFT level.

The performance of DFT calculations in the prediction of hyperfine interactions is variable, depending in particular on the type of considered system, i.e. whether the paramagnetic system is an organic radical, a metal centre or, as in the present case, a triplet state. In addition to that, the accuracy of the computed hyperfine interaction parameters depends also on the characteristics of the nucleus coupled to the paramagnetic system. Especially the calculation of hyperfine interaction parameters of weakly coupled nuclei, which are not directly part of the paramagnetic system, for example ligand nuclei, may be affected by errors. The B3LYP functional and the EPRII basis set used for the hyperfine calculation have proven to be among the most adequate in the calculation of hyperfine interaction parameters for most systems [72,73,79]. In several EPR investigations in the literature the agreement between hyperfine interaction parameters obtained from DFT calculations and experimental ESEEM and ENDOR data was found to be satisfactory [80-84], generally the trends in hyperfine interaction parameters agree well with experiment, although the absolute values often do not. The hyperfine interaction parameters, particularly the isotropic hyperfine interaction constant, are highly susceptible to small changes in spin populations that are within the error of the spin density calculation. The accuracy with which the hyperfine interaction parameters can be determined is thus limited by the accuracy of the calculation of the spin populations [79,83]. Usually the hyperfine coupling parameters obtained from DFT calculations are used only as guidelines or starting values in the simulation of experimental data.

The hyperfine interaction parameters derived by optimization of the agreement between experimental and simulated data do not differ significantly from the values calculated at EPRII level for the "Fixed AA PBE0 structure". The orientation of the hyperfine interaction tensors are

preserved, as well as the relative magnitude of the principal values of the dipolar hyperfine interaction tensor and of the hyperfine interactions of the two water protons. It can hence be concluded that the model structure is compatible with experimental ESEEM data and that it is a reliable model for the photoprotective site of the PCP antenna complex. In particular, the orientation of the water molecule with respect to the chlorophyll and peridinin molecules, not defined in the X-ray structure, has been identified by the geometry optimizations and is in agreement with the ESEEM results. The geometry of the photoprotective site resulting from the constrained geometry optimization at PBE0 level, confirmed by the ONIOM calculations and compatible with the experimental ESEEM data places the water molecule between peridinin and chlorophyll with one proton coordinated to the His66 residue and the other pointing towards the peridinin chain. The experimental data confirms the presence of a single orientation of the water molecule rather than a distribution of different orientations. The position and orientation of the water molecule is favourable for extending the overlap between the chlorophyll and peridinin triplet state wavefunctions.

The geometry and electronic structure of the photoprotective site determined in this ESEEM study are essential for future calculations aimed at gaining insights into the role of the water molecule in the triplet-triplet energy transfer by comparing the rates of TTET in the presence and in the absence of the water molecule. The long distance triplet-triplet energy transfer, like the electron transfer, is a non-adiabatic process with a rate constant defined by the golden rule:

$$k = \frac{2\pi}{\hbar} |V_{\text{TT}}|^2 \text{FCWDS}$$

where FCWDS stands for the Frank-Condon weighted density of states and V_{TT} is the TTET coupling, defined as:

$$V_{\text{TT}} = \left\langle \Psi_{\text{LUMO}}^{\text{D}}(1) \Psi_{\text{HOMO}}^{\text{A}}(2) \left| \frac{e^2}{r_{12}} \right| \Psi_{\text{LUMO}}^{\text{A}}(1) \Psi_{\text{HOMO}}^{\text{D}}(2) \right\rangle$$

The distance dependence of this term parallels the distance dependence of the corresponding overlap integrals. While in electron transfer the rate is dependent on a single overlap integral, in triplet-triplet energy transfer the rate depends on the product of two overlap integrals, and therefore the exponential decay of the TTET rate with the distance r_{12} is twice that of electron transfer [85]. This process is thus characterized by stricter distance requirements, favouring the hypothesis of the presence of a bridge molecule extending the overlap between the donor's and acceptor's wavefunctions for efficient energy transfer. An accurate determination of the TTET rate requires a detailed knowledge of the wavefunctions of the donor and the acceptor. The information on the electronic structure derived from the ESEEM results can be used in order to include the contribution of the water molecule into the wavefunctions of the acceptor.

Recently, a theoretical study on the TTET in PCP and in another light-harvesting complex has been published, where the effect of the water molecule coordinated to chlorophyll on the TTET coupling has also been considered [86]. A method previously developed by the same authors was employed for the calculation of the TTET coupling [87]. The calculations were performed on the X-ray structure with optimized hydrogen atoms. The molecule Per614 gave the largest coupling among the four peridinin contained in one pigment cluster, in agreement with EPR results [1], but the bridging water molecule was found to give a negative contribution to the coupling, which was attributed to an opposite phase of the water-mediated coupling with respect to the through-space coupling. In addition to that, the same water molecule was surprisingly found to increase the coupling for another peridinin molecule, Per613, positioned on the other side of the chlorophyll ring and previously ruled out as quencher of the chlorophyll triplet state [1]. The results were obtained based on un-optimized structures and were entirely detached from spectroscopic evidence on the electronic structure of the peridinin and chlorophyll molecules. The adopted computational approach may therefore not describe the electronic coupling in the PCP complex accurately. In fact, a previous theoretical study on PCP reported that the water molecule between peridinin and chlorophyll gives a significant contribution to the intermolecular interaction energy between the two pigments [3], in agreement with the EPR spectroscopic evidence.

The results of the ESEEM experiments clearly demonstrate the presence of an interaction between the peridinin molecule Per614 and the water molecule H₂O 701, which is interposed between the peridinin molecule Per614 and Chl601, its partner in the TTET at the basis of the photoprotection mechanism in the PCP antenna complex. Both the computed and optimized hyperfine interaction parameters comprehend a non-zero isotropic hyperfine interaction constant a_{iso} , indicating that part of the spin density of the peridinin triplet state is delocalized onto the water molecule, as is confirmed also by the spin density calculations on the molecules of the photoprotective site. The presence of spin density of the peridinin triplet state on the water molecule is evidence of the fact that the triplet state wavefunction of the peridinin molecule is extended to the water molecule H₂O 701, which may therefore favour the TTET by extending the overlap between the wavefunctions of chlorophyll and peridinin.

In conclusion, the ESEEM studies combined with quantum mechanical calculations have not only allowed the characterization of the geometric and electronic structure of the photoprotective site in the PCP antenna complex, but have also provided evidence pointing to an involvement of the water molecule in the TTET from chlorophyll to peridinin.

The information on the geometry and electronic structure of the photoprotective site in the PCP antenna complex defined in this work will be used for the calculation of the TTET coupling with a

different procedure from the one adopted in the previously mentioned TTET study. The role of the water bridge will be investigated by considering its influence on the wavefunction of the donor and of the acceptor and by calculating the corresponding TTET exchange integral.

CHAPTER 8

HYSCORE EXPERIMENTS ON THE PERIDININ TRIPLET STATE

HYSCORE experiments can provide further information on the studied system with respect to the two- and three-pulse ESEEM experiments. The higher resolution of this 2D experiment allows a better determination of the parameters describing the interactions of the spin system. Additionally, in this type of experiment the contributions of distinct nuclei are also more easily distinguished. In systems with orientation selection the HYSCORE experiment is also more sensitive to the relative orientation of the hyperfine and nuclear quadrupole interaction tensor with respect to the molecular frame.

The HYSCORE spectra of disordered samples of paramagnetic systems with orientation selection are similar to single crystal spectra, since the microwave pulse selects only specific orientations with respect to the external magnetic field [25,88,89]. Therefore, the spectra do not contain the correlation patterns characteristic of HYSCORE spectra of disordered samples, but display more or less defined cross peaks.

In chapter 5 the formula describing the electron spin echo envelope modulation for a triplet state system coupled to an $I = \frac{1}{2}$ nucleus in the HYSCORE experiment was derived, and it was shown that the corresponding spectrum is characterized by cross peaks at $(\nu_{\pm 1}, \nu_0)$ and $(\nu_0, \nu_{\pm 1})$, where ν_0 is equal to the nuclear Larmor frequency. Hence in the HYSCORE spectra of the peridinin triplet state cross peaks are expected along $\nu_1 = \nu_0$ and $\nu_2 = \nu_0$. The distance of the cross peaks from the frequency diagonal is a measure of the strength of the hyperfine interaction of the coupled nucleus with the peridinin triplet state. Distant nuclei, which are very weakly coupled to the triplet state, give rise to peaks on the frequency diagonal.

Preliminary HYSCORE experiments were performed in order to investigate whether this

experiment could provide further information on the interaction between the water molecule H₂O 701 and the peridinin triplet state.

8.1 MATERIALS AND METHODS

The untreated and D₂O-exchanged PCP samples used for the HYSCORE experiments were prepared as described in section 6.1.1.

The HYSCORE experiments were performed on a Bruker Eleksys E580 pulse EPR spectrometer with the same experimental setup as for the two- and three-pulse experiments.

The HYSCORE experiments on the PCP complex were carried out by using the pulse sequence $\frac{\pi}{2} - \tau - \frac{\pi}{2} - t_1 - \pi - t_2 - \frac{\pi}{2} - \tau - \text{echo}$ and by measuring the integrated echo intensity as a function of t_1 and t_2 . The duration of both the $\frac{\pi}{2}$ and π pulses was 16 ns, the π pulse was programmed on a separate channel with a higher microwave power and adjusted in order to obtain the maximum inversion. The time τ between the first two pulses was 216 ns. The initial value for t_1 and t_2 was 32 ns, which was incremented in 16 or 28 ns time steps. The data sets contained 64x64 or 128x128 points. A four-step phase cycle suggested by Gemperle *et al.* [38] was applied in order to avoid interference with unwanted echoes. Data were accumulated for 18-35 h.

The experimental HYSCORE time domain data were processed with a home-written program in Matlab®. The 2D time domain data are corrected for the unmodulated relaxation decay in t_1 and t_2 by a third-order polynomial background correction in both dimensions, which also eliminates all the signals modulated only in a single time dimension and thus removes all axial peaks in the frequency domain. The baseline-corrected data are then apodized with a Hamming window and zero-filled to 512 points in both dimensions. 2D FT magnitude spectra are calculated and presented as contour plots.

The simulation of HYSCORE spectra was performed in Matlab® with the *saffron* function of the *Easypin* routine analogously to the simulation of ESEEM data (section 7.1.3).

8.2 RESULTS

The HYSCORE results obtained in the course of this thesis work are preliminary. The HYSCORE experiment is very time-consuming, particularly when applied to photo-excited systems due to the limit on the repetition rate imposed by the external laser excitation. The data shown in the following was collected with parameters allowing a reasonable signal-to-noise ratio in a comparatively short time.

The HYSORE experiment was performed only at the X^+ field position, which is characterized by the highest echo intensity. The experiments were performed with different parameters, depending on the region of interest in the spectrum. The time-step and the data set dimensions were adjusted in order to focus on the contributions of the hydrogen or of the deuterium nuclei coupled to the paramagnetic system.

8.2.1 DEUTERIUM HYSORE

The HYSORE spectrum collected at the X^+ field position on the D_2O -exchanged PCP sample is reported in Fig. 8.1.

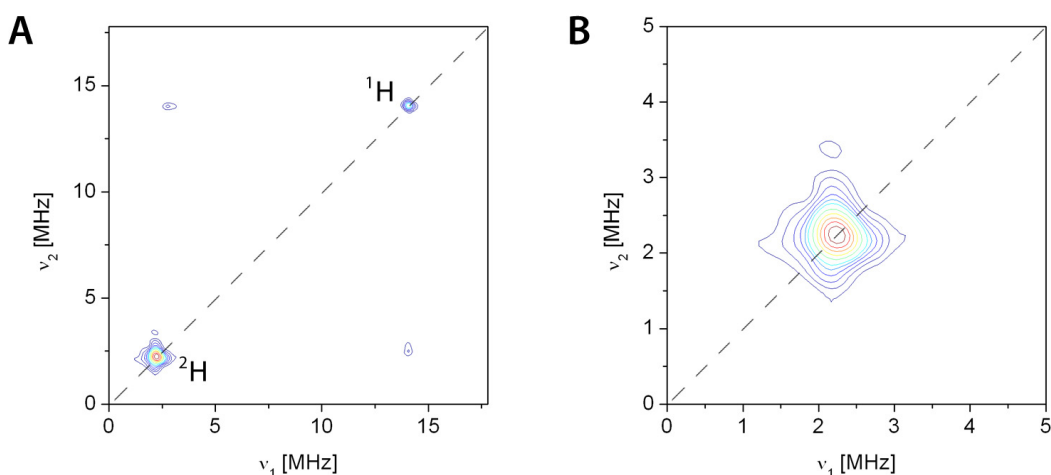


Fig. 8.1 Experimental HYSORE spectrum of the D_2O -exchanged PCP sample at the X^+ (328 mT) field position recorded at $T=20K$ and with $\nu=9.72$ GHz, $\tau=216$ ns, $t_1=t_2=32$ ns, $dt=28$ ns. (A) upper right quadrant of the HYSORE spectrum; (B) close-up of the deuterium region of the HYSORE spectrum.

The HYSORE signals are limited to the upper right quadrant of the HYSORE spectrum, indicating the presence of weak interactions between deuterium nuclei and the peridinin triplet state. The HYSORE spectrum contains two intense signals on the frequency diagonal, one at the deuterium Larmor frequency and one at the proton Larmor frequency. The proton signal on the diagonal can again be attributed to protons weakly coupled to the peridinin triplet state. The cross peaks at (2.8,14) MHz and (14, 2.8) MHz can be attributed to the protons of one methyl group on the peridinin molecule with hyperfine interaction parameters identified in previous pulsed ENDOR and DFT studies on peridinin in the PCP antenna complex ($A_x=11.5$ MHz, $A_y=9.8$ MHz, $A_z=10.8$ MHz) [13,68].

The peak at the deuterium Larmor frequency lacks a well-defined hyperfine structure. This is due to the fact that the hyperfine interaction of the water protons with the peridinin triplet state is very weak, as indicated by the results of the ESEEM experiments. Therefore its signal would be covered by the signal on the frequency diagonal due exchangeable matrix protons substituted by deuterium nuclei. The simulation of the HYSOCORE spectrum with the hyperfine interaction parameters giving the best agreement with the two- and three-pulse ESEEM data is reported in Fig. 8.2. Due to the weakness of the hyperfine and nuclear quadrupole interactions, the signal has no well defined hyperfine structure and falls very close to the intense peak on the frequency diagonal in the experimental spectrum. Hence in the present case the HYSOCORE experiment, even though being characterized by a higher resolution than the two-pulse and three-pulse ESEEM experiments, is not able to resolve the signals due to the water protons. Longer accumulation times may lead to a better signal-to-noise ratio, which could allow distinguishing the contribution of the water molecule from that of the matrix deuterium nuclei.

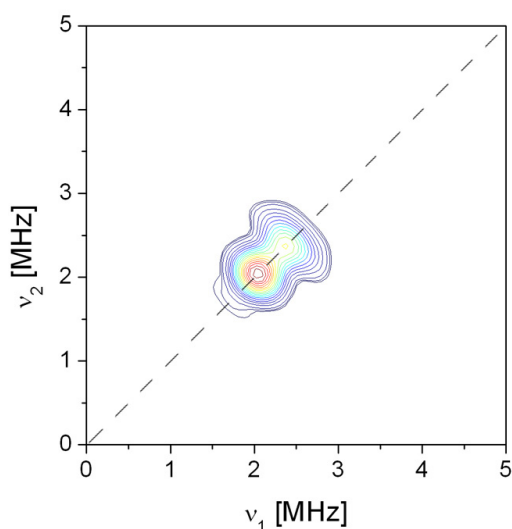


Fig. 8.2 Simulations of the deuterium HYSOCORE spectrum at the X^+ field position (328 mT) with the optimized hyperfine interaction parameters (Table 7.3): $A_x=-0.46$ MHz, $A_y=0.32$ MHz, $A_z=-0.19$ MHz, $\alpha=-10^\circ$, $\beta=53^\circ$, $\gamma=90^\circ$ for H1; $A_x=-0.09$ MHz, $A_y=0.11$ MHz, $A_z=-0.04$ MHz, $\alpha=-20^\circ$, $\beta=50^\circ$, $\gamma=100^\circ$ for H2; $Q=0.25$ MHz, $\eta=0$.

8.2.2 PROTON HYSOCORE

The HYSOCORE experiment was repeated both on the untreated and D_2O -exchanged PCP sample with different experimental parameters aimed at highlighting the 1H region of the spectrum; the corresponding spectra are reported in Fig. 8.3.

The HYSOCORE spectrum of the untreated PCP sample shows an intense peak on the frequency diagonal at the proton Larmor frequency due to all the protons weakly coupled to the peridinin

triplet state. The intense cross peaks at (2.8,14) MHz and (14, 2.8) MHz can again be assigned to the protons of the methyl group of the peridinin molecule mentioned before. In these spectra additional cross peaks at about (7,14) MHz and (14, 7) MHz are visible which are in agreement with the hyperfine parameters identified in previous works for the protons of the other methyl group of peridinin ($A_x=7.7$ MHz, $A_y=6.1$ MHz, $A_z=7$ MHz) [13,68]. The signal-to-noise ratio of the experimental spectrum is not high enough for an unambiguous assignment of other weak cross peaks to further protons of the peridinin molecule with known hyperfine interaction parameters. The cross-shape of the peak on the frequency diagonal at the proton Larmor frequency is probably due to several weakly coupled hydrogen atoms with cross peaks close to the frequency diagonal, they remain however unresolved.

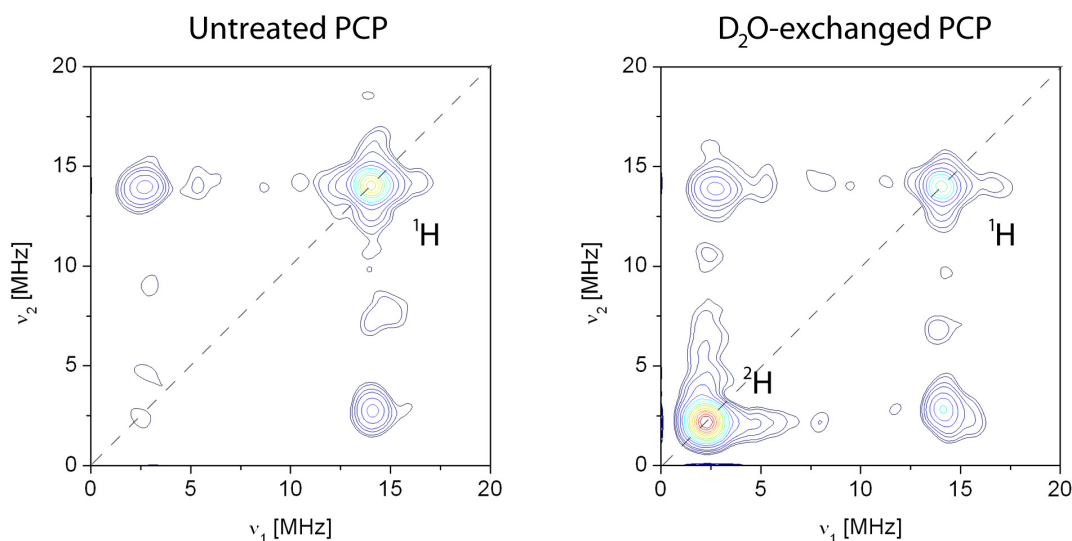


Fig. 8.3 Experimental HYSORE spectra of the untreated and D_2O -exchanged PCP complex at the X^+ (328 mT) field position. Experimental parameters: $T=20$ K, $\nu=9.7$ GHz, $t_1=t_2=32$ ns, $\tau=216$ ns, $dt=16$ ns. The HYSORE spectra are normalized on the maximum of the peak at (2.8,14) MHz for comparison.

By comparing the HYSORE spectra of the untreated and D_2O -exchanged samples it can be noted that the intensity of the peak at the proton Larmor frequency is reduced and that an intense peak appears on the frequency diagonal at the deuterium Larmor frequency. These changes are due to the substitution of the exchangeable protons coupled to the peridinin triplet state by deuterium nuclei. The cross peaks due to protons that are not exchanged by the dialysis procedure are present in both spectra, for example the cross peak due to the methyl protons on peridinin can be seen both in the spectrum of the untreated and D_2O -exchanged sample. The low-frequency region of the spectra in Fig. 8.3 is not well defined due to the chosen experimental parameters; hence nothing can be inferred from the deuterium peak.

In Fig. 8.4 the simulation of the HYSCORE spectrum at the X^+ field position for the two protons of the water molecule H_2O 701 with the hyperfine parameters giving the best agreement with the experimental ESEEM data, reported in Table 7.3, is shown. The hyperfine simulation parameters are the same used for the simulation in Fig. 8.2 but rescaled for hydrogen nuclei. The visible hyperfine structure is due exclusively to the water proton closer to peridinin, the signal of the other water proton falls on the frequency diagonal.

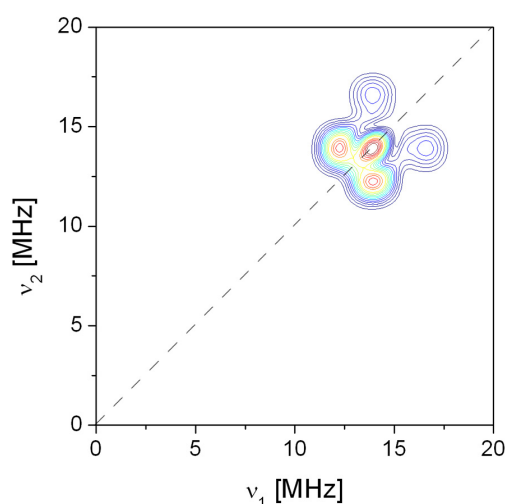


Fig. 8.4 Simulations of the proton HYSCORE spectrum at the X^+ field position (328 mT) with the optimized hyperfine interaction parameters (Table 7.3): $A_x=-2.98$ MHz, $A_y=2.12$ MHz, $A_z=-1.21$ MHz, $\alpha=-10^\circ$, $\beta=53^\circ$, $\gamma=90^\circ$ for H1; $A_x=-0.62$ MHz, $A_y=0.69$ MHz, $A_z=-0.23$ MHz, $\alpha=-20^\circ$, $\beta=50^\circ$, $\gamma=100^\circ$ for H2.

The water proton would thus contribute to the cross-shape of the diagonal peak at the proton Larmor frequency, more prominent in the HYSCORE spectrum of the untreated sample. Unfortunately, the hyperfine structure due to the weakly coupled water protons is not well resolved in the experimental HYSCORE spectra; hence no definite conclusions are possible due to the rather poor signal-to-noise ratio of the spectra.

8.3 DISCUSSION

The present work is, to the best of our knowledge, the first example of the HYSCORE experiment applied to a photo-excited triplet state. The analytical expressions describing the HYSCORE experiment for a triplet state were not present in the literature and were derived in the present work with the density matrix formalism, as reported in chapter 5.

The preliminary HYSCORE experiments described above were performed on the PCP antenna complex with the hope of resolving the hyperfine structure due to the protons on the water

molecule interposed between peridinin and chlorophyll in the photoprotective site of PCP and thus confirming the results of the two-pulse and three-pulse ESEEM experiments and providing more accurate information on the orientation and principal values of the hyperfine interaction tensors of the water protons.

The peridinin triplet state interacts with several hydrogen nuclei, both on the molecule itself and in its close environment. In previous pulse ENDOR and DFT studies on peridinin in PCP the hyperfine interaction parameters of the hydrogen nuclei on the peridinin molecule have been determined [13,68]. In order to distinguish the signals due to the water molecule coupled to the peridinin triplet state from the signals of these nuclei, two types of experiments are possible.

First, the HYSCORE experiment was performed on the D₂O-exchanged PCP sample and the signals in the region of the deuterium Larmor frequency were analyzed. The agreement between simulations with different hyperfine interaction parameters and the experimental spectrum would confirm the validity of the principal values and orientations of the interaction tensors. A drawback of this type of experiment is that the hyperfine and nuclear quadrupole interactions in this case are very weak, leading to peaks close to the diagonal, where they are covered by the signals of distant matrix nuclei, as seen in the experiments.

Second, the HYSCORE experiment was performed both on the untreated and D₂O-exchanged sample and the proton region was analyzed in order to identify peaks present in the spectrum of the untreated, but absent in the spectrum of the D₂O-exchanged sample. In principle, these peaks could be attributed to the exchangeable protons interacting with the peridinin triplet state and the spectrum could be compared with simulations performed with the proton hyperfine interaction parameters. The advantage of this method is that, since the hyperfine interaction parameters for proton and deuterium nuclei scale with the ratio of the nuclear g values, the proton hyperfine interactions are about 6.5 times larger than the corresponding deuterium hyperfine interactions, and thus are farther away from the frequency diagonal [90]. However, since several non-exchangeable protons are weakly coupled to the peridinin triplet state, the region of interest in the spectrum is crowded by signals and an excellent signal-to-noise ratio would be required in order to distinguish the different signals.

From the results presented above it can be concluded that with considerably longer accumulation times the signal-to-noise ratio of the experimental HYSCORE spectrum might be improved sufficiently to be able to distinguish the contribution of the weakly coupled nuclei on the water molecule from the intense broad signal on the frequency diagonal due to several distant matrix nuclei. By repeating the HYSCORE experiment also at other magnetic field positions, additional information might be obtained.

The HYSCORE experiment, being a two-dimensional experiment is characterized by a higher resolution than the two- and three-pulse ESEEM experiments. However, due to the need of acquiring electron spin echo envelopes in two dimensions, the data accumulation times required in order to obtain a comparable signal-to-noise ratio with respect to the ESEEM experiments are considerably longer. In the preliminary HYSCORE experiments performed in the course of this work the accumulation times were quite short and hence the potential of the HYSCORE experiment could not be fully exploited. More accurate information on both the isotropic hyperfine coupling constant and the dipolar hyperfine interaction parameters, and especially on the relative orientation of the hyperfine tensor with respect to the ZFS tensor of peridinin, could be obtained by repeating the HYSCORE experiments with accumulation times leading to signal-to-noise ratios comparable to those of the ESEEM experiments. This would provide further evidence on the orientation of the water molecule and the electronic structure of the photoprotective site in the PCP antenna complex.

CHAPTER 9

CONCLUSIONS

The peridinin-chlorophyll *a*-protein antenna complex can in many ways be considered as a model system for the study of energy transfer pathways in photosynthetic antenna complexes. It is eligible as such due to its high symmetry and simplicity and due to the availability of its X-ray structure at high resolution. A wealth of information on both singlet and triplet transfer pathways in this complex is present in the literature [1,8,9,11,91,92].

The present work is part of a research project on natural light-harvesting complexes with particular emphasis on the investigation of structure-function relationships in the photoprotection mechanism based on TTET. In previous EPR studies on the PCP antenna complex a specific peridinin molecule (Per614) has been identified as the only chlorophyll triplet state quencher [1]. The properties of this peridinin molecule are studied by means of advanced EPR techniques in order to shed light on the requirements for efficient TTET. The TTET mechanism requires an overlap of the wavefunctions of the donor and acceptor molecules and thus establishes strict distance and orientation requirements. Per614 is distinguished from the other peridinin molecules of the pigment cluster by a shorter centre-to-centre distance and by the presence of a unique water molecule (H₂O 701) at the interface between Per614 and Chl601, which has been proposed to favour TTET by extending the overlap of the donor and acceptor wavefunctions. Bridging water molecules play an important role in enhancing the rate of electron transfer [93] and since triplet-triplet energy transfer can essentially be viewed as a double electron transfer [6,85], with the more significant overlap requirements which that entails, it seems reasonable that water molecules should play a similarly important role in this type of transfer.

In the present work the interaction of the water molecule H₂O 701 with the triplet state of Per614 has been studied by ESEEM and HYSCORE spectroscopy. Additionally the position and orientation of this water molecule, which are not defined in the X-ray structure, has been

deduced by combining the results of ESEEM experiments on the D₂O-exchanged protein complex with state-of-the-art computational methods. Deuterium ESEEM and HYSCORE have been applied to a photo-excited triplet state in a protein complex for the first time. The results of this work clearly demonstrate that the observed electron spin echo envelope modulations are due to the water molecule H₂O 701.

The analytical expressions describing the ESEEM and HYSCORE experiments as applied to a triplet state system coupled with deuterium nuclei have been derived in the present work. Apart from the definition of the modulation frequency and of the modulation depth parameter, the expressions for a single triplet state transition are analogous to the expressions for $S = \frac{1}{2}$ spin systems, since the triplet state system can be approximated to two fictitious $S = \frac{1}{2}$ systems in cases where transition selection applies.

The spectroscopic parameters characterizing the Per614-H₂O 701 system have been extracted from experimental data by simulations. The constraints on the simulation parameters provided by the orientation selectivity and by the employment of different types of experiments allow an accurate determination of the interaction parameters. From these parameters the following conclusions on the geometry and electronic structure of the photoprotective site in the PCP antenna complex can be drawn:

- The experimental ESEEM data has been found to be compatible with a precise structure of the photoprotective site in which the water molecule is coordinated to the chlorophyll's Mg ion and hydrogen-bonded to the nearby histidine residue, while the other water proton points toward the conjugated chain of peridinin (Fig. 9.1).
- The presence of isotropic hyperfine coupling for the water protons indicates that the peridinin triplet state wavefunction is extended onto the water molecule thereby proving its active role in the TTET from chlorophyll to peridinin.

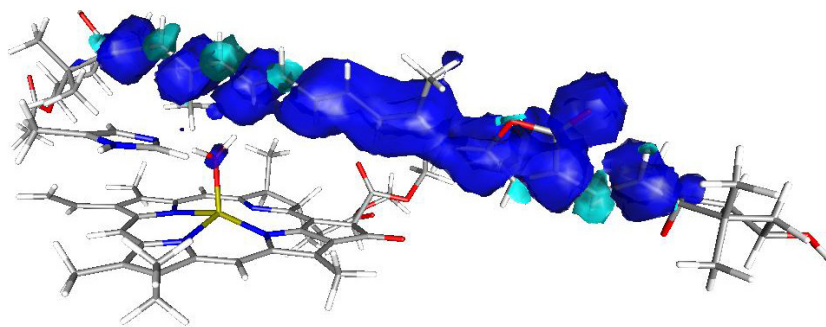


Fig. 9.1 Structure of the photoprotective site in the PCP antenna complex and calculated spin density of the peridinin triplet state.

The results of this study are at the basis of future calculations of the TTET coupling with a procedure that combines theory with spectroscopic evidence. The advantage of this method is that it employs the geometries and electronic structures validated by ESEEM experiments and which are influenced by the presence of the bridging water molecule.

The methodology, developed for the PCP antenna complex, can be extended to the study of TTET in natural antenna complexes of higher structural complexity, for which bridging molecules have already been identified [69,94], and exploited in the design and the characterization artificial biomimetic antenna complexes. The inclusion of carotenoids and appropriate bridge molecules in the architecture of these devices with spatial arrangements aimed at optimizing both the singlet-singlet energy transfer necessary for light-harvesting and the triplet-triplet energy transfer at the basis of photoprotection may improve their efficiency. In particular, photoprotection might play an important role in extending the life-time of biomimetic devices under prolonged and wide-spread illumination conditions.

REFERENCES

- [1] Di Valentin, M.; Ceola, S.; Salvadori, E.; Agostini, G.; Carbonera, D. *Biochim. Biophys. Acta-Bioenerg.* **2008**, *1777*, 186-195.
- [2] *Oxygenic Photosynthesis: The Light Reactions*; Ort, D. R.; Yocum, C. F., Eds.; Kluwer Academic Publishers: Dordrecht, 1996.
- [3] Mao, L.; Wang, Y.; Hu, X. *J. Phys. Chem. B* **2003**, *107*, 3963-3971.
- [4] Förster, T. *Ann. Phys. (Leipzig)* **1948**, *2*, 55-75.
- [5] Dexter, D. L. *J. Chem. Phys.* **1953**, *21*, 836-850.
- [6] Closs, G. L.; Johnson, M. D.; Miller, J. R.; Piotrowiak, P. *J. Am. Chem. Soc.* **1989**, *111*, 3751-3753.
- [7] Hofmann, E.; Wrench, P. M.; Sharples, F. P.; Hiller, R.; Welte, W.; Diederichs, K. *Science* **1996**, *272*, 1788-1791.
- [8] Polívka, T.; Hiller, R. G.; Frank, H. A. *Arch. Biochem. Biophys.* **2007**, *458*, 111-120.
- [9] Schulte, T.; Johanning, S.; Hofmann, E. *Eur. J. Cell Biol.* **2010**, *89*, 990-997.
- [10] Schulte, T.; Hiller, R. G.; Hofmann, E. *FEBS Lett.* **2010**, *584*, 973-978.
- [11] Bautista, J. A.; Hiller, R. G.; Sharples, F. P.; Gosztola, D.; Wasielewski, M.; Frank, H. A. *J. Phys. Chem. A* **1999**, *103*, 2267-2273.
- [12] Alexandre, M. T. A.; Lührs, D. C.; van Stokkum, I. H. M.; Hiller, R.; Groot, M.-L.; Kennis, J. T. M.; van Grondelle, R. *Biophys. J.* **2007**, *93*, 2118-2128.
- [13] Di Valentin, M.; Ceola, S.; Agostini, G.; Giacometti, G. M.; Angerhofer, A.; Crescenzi, O.; Barone, V.; Carbonera, D. *Biochim. Biophys. Acta-Bioenerg.* **2008**, *1777*, 295-307.
- [14] Di Valentin, M.; Agostini, G.; Salvadori, E.; Ceola, S.; Giacometti, G. M.; Hiller, R. G.; Carbonera, D. *Biochim. Biophys. Acta-Bioenerg.* **2009**, *1787*, 168-175.
- [15] Di Valentin, M.; Salvadori, E.; Ceola, S.; Carbonera, D. *Appl. Magn. Reson.* **2010**, *37*, 191-205.
- [16] Odom, B.; Hanneke, D.; D'Urso, B.; Gabrielse, G. *Phys. Rev. Lett.* **2006**, *97*, 030801.
- [17] El-Sayed, M. A. *J. Chem. Phys.* **1971**, *54*, 680-692.
- [18] El-Sayed, M. A.; Tinti, D. E.; Yee, E. M. *J. Chem. Phys.* **1969**, *51*, 5721-5723.
- [19] Imamura, T. O., O., Murai, H.; Obi, K. *J. Phys. Chem.* **1984**, *88*, 4028-4031.
- [20] Akiyama, K.; Terokubota, S.; Ikoma, T.; Ikegami, Y. *J. Am. Chem. Soc.* **1994**, *116*, 5324-5327.
- [21] Di Valentin, M.; Tait, C.; Salvadori, E.; Ceola, S.; Scheer, H.; Hiller, R.; Carbonera, D. **2011**, Manuscript submitted for publication.
- [22] Brenner, H. C.; Brock, J. C.; Harris, C. B. *Chem. Phys.* **1978**, *31*, 137-164.
- [23] Di Valentin, M.; Biasibetti, F.; Ceola, S.; Carbonera, D. *J. Phys. Chem. B* **2009**, *113*, 13071-13078.
- [24] Di Valentin, M.; Salvadori, E.; Agostini, G.; Biasibetti, F.; Ceola, S.; Hiller, R.; Giacometti, G. M.; Carbonera, D. *Biochim. Biophys. Acta-Bioenerg.* **2010**, *1797*, 1759-1767.
- [25] Schweiger, A.; Jeschke, G. *Principles of Pulse Electron Paramagnetic Resonance*; Oxford University Press: Oxford, 2001.
- [26] Rowan, L. G.; Hahn, E. L.; Mims, W. B. *Phys. Rev.* **1965**, *137*, A61-A71.
- [27] Mims, W. B. *Phys. Rev. B* **1972**, *5*, 2409-2419.
- [28] Dikanov, S. A.; Tsvetkov, Y. D. *Electron Spin Echo Envelope Modulation (ESEEM) Spectroscopy*; CRC Press: Boca Raton, Florida, 1992.

REFERENCES

- [29] Kevan, L. In *Time Domain Electron Spin Resonance*; Kevan, L. S., R.M., Ed.; J. Wiley & Sons, Inc.: New York, 1979.
- [30] Weil, J. A.; Bolton, J. R. *Electron Paramagnetic Resonance: Elementary Theory and Practical Applications*; John Wiley & Sons, Inc.: Hoboken, New Jersey, 2007.
- [31] Höfer, P.; Grupp, A.; Nebenführ, H.; Mehring, M. *Chem. Phys. Lett.* **1986**, *132*, 279-282.
- [32] Shane, J. J.; Höfer, P.; Reijerse, E. J.; De Boer, E. *J. Magn. Reson.* **1992**, *99*, 596-604.
- [33] Slichter, C. P. *Principles of Magnetic Resonance*; Springer Verlag: Berlin, 1980.
- [34] Shubin, A. A.; Dikanov, S. A. *J. Magn. Reson.* **1983**, *52*, 1-12.
- [35] Dikanov, S. A.; Shubin, A. A.; Parmon, V. N. *J. Magn. Reson.* **1981**, *42*, 474-487.
- [36] Sloop, D. J.; Yu, H.-L.; Lin, T. S.; Weissman, S. I. *J. Chem. Phys.* **1981**, *75*, 3746-3757.
- [37] Dikanov, S. A.; Yudanov, V. F.; Tsvetkov, Y. D. *J. Magn. Reson.* **1979**, *34*, 631-645.
- [38] Gemperle, C.; Aebli, G.; Schweiger, A.; Ernst, R. R. *J. Magn. Reson.* **1990**, *88*, 241-256.
- [39] Tyryshkin, A. M.; Dikanov, S. A.; Goldfarb, D. *J. Magn. Reson., Ser A* **1993**, *105*, 271-283.
- [40] Pöppel, A.; Böttcher, R. *Chem. Phys.* **1997**, *221*, 53-66.
- [41] Höfer, P. *J. Magn. Reson., Ser A* **1994**, *111*, 77-86.
- [42] Pöppel, A.; Kevan, L. *J. Phys. Chem.* **1996**, *100*, 3387-3394.
- [43] Pöppel, A.; Hartmann, M.; Böhlmann, W.; Böttcher, R. *J. Phys. Chem. A* **1998**, *102*, 3599-3606.
- [44] Ponti, A. *J. Magn. Reson.* **1997**, *127*, 87-104.
- [45] Coffino, A. R.; Peisach, J. *J. Chem. Phys.* **1992**, *97*, 3072-3091.
- [46] Larsen, R. G.; Halkides, C. J.; Singel, D. J. *J. Chem. Phys.* **1993**, *98*, 6704-6721.
- [47] Benetis, N. P.; Dave, P. C.; Goldfarb, D. *J. Magn. Reson.* **2002**, *158*, 126-142.
- [48] Stoll, S.; Britt, R. D. *Phys. Chem. Chem. Phys.* **2009**, *11*, 6614-6625.
- [49] Steck, K.; Wacker, T.; Welte, W.; Sharples, F. P.; Hiller, R. G. *FEBS Lett.* **1990**, *268*, 48-50.
- [50] Sharples, F. P.; Wrench, P. M.; Ou, K.; Hiller, R. G. *Biochim. Biophys. Acta* **1996**, *1276*, 117-123
- [51] Crystall, B.; Booth, P. J.; Klug, D. R.; Barber, J.; Porter, G. *FEBS Lett.* **1989**, *249*, 75-78.
- [52] Mims, W. B.; Davis, J. L.; Peisach, J. *Biophys. J.* **1984**, *45*, 755-766.
- [53] Mims, W. B. *J. Magn. Reson.* **1984**, *59*, 291-306.
- [54] Neese, F. *ORCA - An ab initio, DFT and semiempirical SCF-MO package (2.8)* **2010**, Universität Bonn.
- [55] Frisch, M. J.; Trucks, G. W.; Schlegel, H. B.; Scuseria, G. E.; Robb, M. A.; Cheeseman, J. R.; Scalmani, G.; Barone, V.; Mennucci, B.; Petersson, G. A.; Nakatsuji, H.; Caricato, M.; Li, X.; Hratchian, H. P.; Izmaylov, A. F.; Bloino, J.; Zheng, G.; Sonnenberg, J. L.; Hada, M.; Ehara, M.; Toyota, K.; Fukuda, R.; Hasegawa, J.; Ishida, M.; Nakajima, T.; Honda, Y.; Kitao, O.; Nakai, H.; Vreven, T.; Montgomery, J. A. J.; Peralta, J. E.; Ogliaro, F.; Bearpark, M.; Heyd, J. J.; Brothers, E.; Kudin, K. N.; Staroverov, V. N.; Kobayashi, R.; Normand, J.; Raghavachari, K.; Rendell, A.; Burant, J. C.; Iyengar, S. S.; Tomasi, J.; Cossi, M.; Rega, N.; Millam, J. M.; Klene, M.; Knox, J. E.; Cross, J. B.; Bakken, V.; Adamo, C.; Jaramillo, J.; Gomperts, R.; Stratmann, R. E.; Yazyev, O.; Austin, A. J.; Cammi, R.; Pomelli, C.; Ochterski, J. W.; Martin, R. L.; Morokuma, K.; Zakrzewski, V. G.; Voth, G. A.; Salvador, P.; Dannenberg, J. J.; Dapprich, S.; Daniels, A. D.; Farkas, Ö.; Foresman, J. B.; Ortiz, J. V.; Cioslowski, J.; Fox, D. J. *Gaussian 09 (Revision A.1)* **2009**, Gaussian, Inc.
- [56] Hehre, W. J.; Ditchfield, R.; Pople, J. A. *J. Chem. Phys.* **1972**, *56*, 2257-2261.
- [57] Barone, V. *J. Chem. Phys.* **1994**, *101*, 10666-10676.

- [58] Barone, V. *J. Chem. Phys.* **1994**, *101*, 6834-6838.
- [59] Barone, V. In *Recent Advances in Density Functional Methods, Part I*; Chong, D. P., Ed.; World Scientific Publ. Co.: Singapore, 1996.
- [60] Stoll, S.; Schweiger, A. *J. Magn. Reson.* **2006**, *178*, 42-55.
- [61] Vrieze, J.; Hoff, A. J. *Chem. Phys. Lett.* **1995**, *237*, 493-501.
- [62] Lendzian, F.; Bittl, R.; Telfer, A.; Lubitz, W. *Biochim. Biophys. Acta* **2003**, *1605*, 35-46.
- [63] Frick, J.; Vonschutz, J. U.; Wolf, H. C.; Kothe, G. *Molecular Crystals and Liquid Crystals* **1990**, *183*, 269-272.
- [64] Kok, P.; Groenen, E. J. *J. Am. Chem. Soc.* **1996**, *118*, 7790-7794.
- [65] Randall, D. W.; Gelasco, A.; Caudle, M. T.; Pecoraro, V. L.; Britt, R. D. *J. Am. Chem. Soc.* **1997**, *119*, 4481-4491.
- [66] Force, D. A.; Randall, D. W.; Lorigan, G. A.; Clemens, K. L.; Britt, R. D. *J. Am. Chem. Soc.* **1998**, *120*, 13321-13333.
- [67] Edmonds, D. T.; Goren, S. D.; Mackay, A. L.; White, A. A. L.; Sherman, W. F. *J. Magn. Reson.* **1976**, *23*, 505-514.
- [68] Niklas, J.; Schulte, T.; Prakash, S.; van Gastel, M.; Hofmann, E.; Lubitz, W. *J. Am. Chem. Soc.* **2007**, *129*, 15442-15443.
- [69] Salvadori, E.; Di Valentin, M.; Kay, C. M. W.; Pedone, A.; Barone, V.; Carbonera, D. **2011**, Manuscript submitted for publication.
- [70] Himo, F. *J. Phys. Chem. A* **2001**, *105*, 7933-7937.
- [71] Guo, J.-D.; Luo, Y.; Himo, F. *Chem. Phys. Lett.* **2002**, *366*, 73-81.
- [72] Kossmann, S.; Kirchner, B.; Neese, F. *Mol. Phys.* **2007**, *105*, 2049-2071.
- [73] Neese, F. *Coord. Chem. Rev.* **2009**, *253*, 526-563.
- [74] Kevan, L.; Bowman, M. K.; Narayana, P. A.; Boeckman, R. K.; Yudanov, V. F.; D., T. Y. *J. Chem. Phys.* **1975**, *63*, 409-416.
- [75] Warncke, K.; McCracken, J. *J. Chem. Phys.* **1995**, *103*, 6829-6840.
- [76] Shima, S.; Ilagan, R. P.; Gillespie, N.; Sommer, B. J.; Hiller, R.; Sharples, F. P.; Frank, H. A.; Birge, R. R. *J. Phys. Chem. A* **2003**, *107*, 8052-8066.
- [77] Spezia, R.; Zazza, C.; Palma, A.; Amadei, A.; Aschi, M. *J. Phys. Chem. A* **2004**, *108*, 6763-6770.
- [78] Bock, C. W.; Kaufman, A.; Glusker, J. P. *Inorg. Chem.* **1994**, *33*, 419-427.
- [79] Improta, R.; Barone, V. *Chem. Rev.* **2004**, *104*, 1231-1253.
- [80] Larsen, S. C. *J. Phys. Chem. A* **2001**, *105*, 8333-8338.
- [81] Baute, D.; Goldfarb, D. *J. Phys. Chem. A* **2005**, *109*, 7865-7871.
- [82] Yazyev, O. V.; Helm, L.; Malkin, V. G.; Malkina, O. L. *J. Phys. Chem. A* **2005**, *109*, 10997-11005.
- [83] Kababya, S.; Nelson, J.; Calle, C.; Neese, F.; Goldfarb, D. *J. Am. Chem. Soc.* **2006**, *128*, 2017-2029.
- [84] Marchanka, A.; Lubitz, W.; van Gastel, M. *J. Phys. Chem. B* **2009**, *113*, 6917-6927.
- [85] Closs, G. L.; Piotrowiak, P.; MacInnis, J. M.; Fleming, G. R. *J. Am. Chem. Soc.* **1988**, *110*, 2652-2653.
- [86] You, Z.-Q.; Hsu, C.-P. *J. Phys. Chem. A* **2011**, *115*, 4092-4100.
- [87] You, Z.-Q.; Hsu, C.-P. *J. Chem. Phys.* **2010**, *133*, 074105-1-10.

REFERENCES

- [88] Dikanov, S. A.; Xun, L.; Karpel, A. B.; Tyryshkin, A. M.; Bowman, M. K. *J. Am. Chem. Soc.* **1996**, *118*, 8408-8416.
- [89] Szosenfogel, R.; Goldfarb, D. *Mol. Phys.* **1998**, *95*, 1295-1308.
- [90] Dikanov, S. A.; Samoilova, R. I.; Kolling, D. R. J.; Holland, J. T.; Crofts, A. R. *J. Biol. Chem.* **2004**, *279*, 15814-15823.
- [91] Damjanović, A.; Ritz, T.; Schulten, K. *Biophys. J.* **2000**, *79*, 1695-1705.
- [92] Schulte, T.; Niedzwiedzki, D. M.; Birge, R. R.; Hiller, R. G.; Polívka, T.; Hofmann, E.; Frank, H. A. *Proc. Natl. Acad. Sci. U.S.A.* **2009**, *106*, 20764-20769.
- [93] Lin, J.; Balabin, I. A.; Beratan, D. N. *Science* **2005**, *310*, 1311-1313.
- [94] Di Valentin, M.; Biasibetti, F.; Ceola, S.; Carbonera, D. *J. Phys. Chem. B* **2009**, *113*, 13071-13078.

APPENDIX

MATLAB® PROGRAM FOR THE CALCULATION OF THE PROTON HFI TENSOR

HFITENSOR.M

```
% Calculation of the hyperfine interaction tensor based on the geometry of
% the pigment cluster in PCP

% Method of Multinuclear dipole interactions as described in:
% D.A. Force, D.W. Randall, R.D. Britt J. Am. Chem. Soc. 1998,120,13321-13333

% clear all;
% close all;
% clc;

% Load geometry
[atm,atmn,atmtyp,mol,m,moln,x,y,z,nl]=textread('Geometry.dat','%s %s %s %s %s
%s %f %f %f %s');
xyzdata=[x';y';z'];

natoms=length(x);
c=1;p=1;w=1;h=1;
for i=1:natoms
    if strcmp(mol(i),'CLA')
        CLA601(:,c)=xyzdata(:,i);
        nCLA601(c)=atmtyp(i);
        c=c+1;
    else c=c;
    end;
    if strcmp(mol(i),'PID')
        PID614(:,p)=xyzdata(:,i);
        nPID614(p)=atmtyp(i);
        p=p+1;
    else p=p;
    end;
    if strcmp(mol(i),'HOH')
        HOH701(:,w)=xyzdata(:,i);
        nHOH701(w)=atmtyp(i);
        w=w+1;
    else w=w;
    end;
    if strcmp(mol(i),'HIS')
        HIS66(:,h)=xyzdata(:,i);
        nHIS66(h)=atmtyp(i);
        h=h+1;
    else h=h;
    end;
end

figure('numbertitle','off','name','Cluster 601');

plotmol(HOH701,'c',2,1.5,'label off');
hold on;
plotmol(CLA601,'g',2,2,'label off');
hold on;
plotmol(HIS66,'b',2,2,'label off');
hold on;

% Peridinin ZFS tensor axes
[xyz_614] = cut_lut_rings(PID614,nPID614);
[vx614,vy614,vz614,del614,excl614] = carrotaxe(xyz_614');
plot_scartati(del614,excl614,xyz_614');
plotmol(PID614,'r',2,2,'label off');
hold on;
```

APPENDIX – MATLAB® PROGRAM FOR THE CALCULATION OF THE PROTON HFI TENSOR

```

mean_614 = find(strcmp(nPID614,'C15'));
p_av614 = PID614(:,mean_614);
plot_per_axes(vx614,vy614,vz614,p_av614);
axis vis3d;

% Quadrupole Tensor Orientation (assumed along O-H bond)

% H2O quadrupole tensor axes
% H2
b1=HOH701(:,2)-HOH701(:,1);
b2=HOH701(:,3)-HOH701(:,1);
A3=b1./norm(b1);
A1=cross(b1,b2);
A1=A1./norm(A1);
A2=cross(A1,A3);
A2=A2./norm(A2);
line([0 A2(1)]+HOH701(1,2), [0 A2(2)]+HOH701(2,2), [0 A2(3)]+HOH701(3,2));
text(HOH701(1,2)+A2(1),HOH701(2,2)+A2(2),HOH701(3,2)+A2(3),'A2');
line([0 A1(1)]+HOH701(1,2), [0 A1(2)]+HOH701(2,2), [0 A1(3)]+HOH701(3,2));
text(HOH701(1,2)+A1(1),HOH701(2,2)+A1(2),HOH701(3,2)+A1(3),'A1');
line([0 A3(1)]+HOH701(1,2), [0 A3(2)]+HOH701(2,2), [0 A3(3)]+HOH701(3,2));
text(HOH701(1,2)+A3(1),HOH701(2,2)+A3(2),HOH701(3,2)+A3(3),'A3');

% H3
A23=b2./norm(b2);
A21=cross(b1,b2);
A21=A21./norm(A21);
A22=cross(A21,A23);
A22=A22./norm(A22);
line([0 A22(1)]+HOH701(1,3), [0 A22(2)]+HOH701(2,3), [0 A22(3)]+HOH701(3,3));
text(HOH701(1,3)+A22(1),HOH701(2,3)+A22(2),HOH701(3,3)+A22(3),'A2');
line([0 A21(1)]+HOH701(1,3), [0 A21(2)]+HOH701(2,3), [0 A21(3)]+HOH701(3,3));
text(HOH701(1,3)+A21(1),HOH701(2,3)+A21(2),HOH701(3,3)+A21(3),'A1');
line([0 A23(1)]+HOH701(1,3), [0 A23(2)]+HOH701(2,3), [0 A23(3)]+HOH701(3,3));
text(HOH701(1,3)+A23(1),HOH701(2,3)+A23(2),HOH701(3,3)+A23(3),'A3');

% Euler angles for H2
NQI2=[A1 -A2 A3];
[aqm2, bqm2, gqm2]=eulang(NQI2);

% Euler angles for H3
NQI3=[A21 -A22 A23];
[aqm3, bqm3, gqm3]=eulang(NQI3);

% Determination of the dipolar hyperfine interaction tensor

u0=4*pi*10^(-7);
h=planck;
ge=gfree;
gn=nucgval('2H');
be=bmagn;
bn=nmagn;
const=(u0/(4*pi*h))*((ge*gn*be*bn)*10^24;

[atmtype,cluster1]=textread('Spindensity.dat','%s %f');
atmtype=atmtype.';
natoms2=size(atmtype);
natoms=natoms2(2);
totspdens=0;
for i=1:natoms
    totspdens=totspdens+cluster1(i);
end
r2(1:natoms)=0.;
Tatom2(1:3,1:3)=0.;
if strcmp(atmtype,nPID614);
    for i=1:natoms

```

APPENDIX – MATLAB® PROGRAM FOR THE CALCULATION OF THE PROTON HFI TENSOR

```

    dist=HOH701(:,2)-PID614(:,i);
    r2(i)=sqrt(sum(dist.^2));
    x2=HOH701(1,2)-PID614(1,i);
    y2=HOH701(2,2)-PID614(2,i);
    z2=HOH701(3,2)-PID614(3,i);
    Adip2=[(r2(i)^2-3*(x2)^2) (-3*x2*y2) (-3*x2*z2);(-3*x2*y2) (r2(i)^2-
    3*(y2)^2) (-3*y2*z2); (-3*x2*z2) (-3*y2*z2) (r2(i)^2-3*(z2)^2)];
    Tatom2=Tatom2-const*( (cluster1(i)/totspdens)/r2(i)^5)*Adip2;
end
Tatom2;
r3(1:natoms)=0.;
Tatom3(1:3,1:3)=0.;
for j=1:natoms
    dist=HOH701(:,3)-PID614(:,j);
    r3(j)=sqrt(sum(dist.^2));
    x3=HOH701(1,3)-PID614(1,j);
    y3=HOH701(2,3)-PID614(2,j);
    z3=HOH701(3,3)-PID614(3,j);
    Adip3=[(r3(j)^2-3*(x3)^2) (-3*x3*y3) (-3*x3*z3);(-3*x3*y3) (r3(j)^2-
    3*(y3)^2) (-3*y3*z3); (-3*x3*z3) (-3*y3*z3) (r3(j)^2-3*(z3)^2)];
    Tatom3=Tatom3-const*( (cluster1(j)/totspdens)/r3(j)^5)*Adip3;
end;
Tatom3;
else
    error('The order of atoms in pdb file does not correspond to that in the
    spin density file.');
```

```

end

[Eigvect2c,T2]=eig(Tatom2)
[Eigvect3c,T3]=eig(Tatom3)

% H2O hyperfine tensor axes
Ax2=Eigvect2(:,1);
Ay2=Eigvect2(:,2);
Az2=Eigvect2(:,3);
text(HOH701(1,2),HOH701(2,2),HOH701(3,2),'H2');
line([0 Ax2(1)]+HOH701(1,2),[0 Ax2(2)]+HOH701(2,2),[0 Ax2(3)]+HOH701(3,2));
text(HOH701(1,2)+Ax2(1),HOH701(2,2)+Ax2(2),HOH701(3,2)+Ax2(3),'Ax');
line([0 Ay2(1)]+HOH701(1,2),[0 Ay2(2)]+HOH701(2,2),[0 Ay2(3)]+HOH701(3,2));
text(HOH701(1,2)+Ay2(1),HOH701(2,2)+Ay2(2),HOH701(3,2)+Ay2(3),'Ay');
line([0 Az2(1)]+HOH701(1,2),[0 Az2(2)]+HOH701(2,2),[0 Az2(3)]+HOH701(3,2));
text(HOH701(1,2)+Az2(1),HOH701(2,2)+Az2(2),HOH701(3,2)+Az2(3),'Az');
% H3
Ax3=Eigvect3(:,1);
Ay3=Eigvect3(:,2);
Az3=Eigvect3(:,3);
text(HOH701(1,3),HOH701(2,3),HOH701(3,3),'H3');
line([0 Ax3(1)]+HOH701(1,3),[0 Ax3(2)]+HOH701(2,3),[0 Ax3(3)]+HOH701(3,3));
text(HOH701(1,3)+Ax3(1),HOH701(2,3)+Ax3(2),HOH701(3,3)+Ax3(3),'Ax');
line([0 Ay3(1)]+HOH701(1,3),[0 Ay3(2)]+HOH701(2,3),[0 Ay3(3)]+HOH701(3,3));
text(HOH701(1,3)+Ay3(1),HOH701(2,3)+Ay3(2),HOH701(3,3)+Ay3(3),'Ay');
line([0 Az3(1)]+HOH701(1,3),[0 Az3(2)]+HOH701(2,3),[0 Az3(3)]+HOH701(3,3));
text(HOH701(1,3)+Az3(1),HOH701(2,3)+Az3(2),HOH701(3,3)+Az3(3),'Az');

% Relative orientation of the HFI tensor with respect to the ZFS tensor
rect=[9,9,19,10];
figure('numbertitle','off','name','Relative Orientation of HFI and ZFS
tensor','Units','centimeters','OuterPosition',rect);
subplot(1,2,1);
title('H2');
axis([-1 1 -1 1 -0.8 0.8]);
grid;
line([0 Ax2(1)],[0 Ax2(2)],[0 Ax2(3)],'color','c','linewidth',2);
text(Ax2(1),Ax2(2),Ax2(3),'Ax','fontSize',8,'fontweight','bold');
line([0 Ay2(1)],[0 Ay2(2)],[0 Ay2(3)],'color','c','linewidth',2);
text(Ay2(1),Ay2(2),Ay2(3),'Ay','fontSize',8,'fontweight','bold');
line([0 Az2(1)],[0 Az2(2)],[0 Az2(3)],'color','c','linewidth',2);

```

APPENDIX — MATLAB® PROGRAM FOR THE CALCULATION OF THE PROTON HFI TENSOR

```

text(Az2(1),Az2(2),Az2(3),'Az','fontsize',8,'fontweight','bold');
line([0 vx614(1)],[0 vx614(2)],[0 vx614(3)],'color','r','linewidth',2);
text(vx614(1),vx614(2),vx614(3),'X','fontsize',8,'fontweight','bold');
line([0 vy614(1)],[0 vy614(2)],[0 vy614(3)],'color','r','linewidth',2);
text(vy614(1),vy614(2),vy614(3),'Y','fontsize',8,'fontweight','bold');
line([0 vz614(1)],[0 vz614(2)],[0 vz614(3)],'color','r','linewidth',2);
text(vz614(1),vz614(2),vz614(3),'Z','fontsize',8,'fontweight','bold');
subplot(1,2,2);
title('H3');
axis([-1 1 -1 1 -0.8 0.8]);
grid;
line([0 Ax3(1)],[0 Ax3(2)],[0 Ax3(3)],'color','c','linewidth',2);
text(Ax3(1),Ax3(2),Ax3(3),'Ax','fontsize',8,'fontweight','bold');
line([0 Ay3(1)],[0 Ay3(2)],[0 Ay3(3)],'color','c','linewidth',2);
text(Ay3(1),Ay3(2),Ay3(3),'Ay','fontsize',8,'fontweight','bold');
line([0 Az3(1)],[0 Az3(2)],[0 Az3(3)],'color','c','linewidth',2);
text(Az3(1),Az3(2),Az3(3),'Az','fontsize',8,'fontweight','bold');
line([0 vx614(1)],[0 vx614(2)],[0 vx614(3)],'color','r','linewidth',2);
text(vx614(1),vx614(2),vx614(3),'X','fontsize',8,'fontweight','bold');
line([0 vy614(1)],[0 vy614(2)],[0 vy614(3)],'color','r','linewidth',2);
text(vy614(1),vy614(2),vy614(3),'Y','fontsize',8,'fontweight','bold');
line([0 vz614(1)],[0 vz614(2)],[0 vz614(3)],'color','r','linewidth',2);
text(vz614(1),vz614(2),vz614(3),'Z','fontsize',8,'fontweight','bold');

% Euler angles for H2 with respect to molecular frame
[am2, bm2, gm2]=eulang(Eigvect2);
dam2=am2/degree
dbm2=bm2/degree
dgm2=gm2/degree

% Euler angles for H3 with respect to molecular frame
[am3, bm3, gm3]=eulang(Eigvect3);
dam3=am3/degree
dbm3=bm3/degree
dgm3=gm3/degree

%Euler angles of ZFS tensor with respect to molecular frame
ZFS=[vx614 vy614 vz614];
[amzfs, bmzfs, gmzfs]=eulang(ZFS);
damzfs=amzfs/degree
dbmzfs=bmzfs/degree
dgmzfs=gmzfs/degree

HFISOCONTOURPER614.M

% Calculation of the hyperfine interaction tensor based on the geometry of
% the pigment cluster in PCP

% Method of Multinuclear dipole interactions as described in:
% D.A. Force, D.W. Randall, R.D. Britt J. Am. Chem. Soc. 1998,120,13321-13333

clear all;
close all;
clc;

% Load geometry
[Hatm,Hatmn,Hatmtyp,Hmol,Hm,Hmoln,Hx,Hy,Hz,Hn1]=textread('ExchangeableHcoordinates.dat','%s %s %s %s %s %s %s %f %f %f %s');
Hxyzdata=[Hx';Hy';Hz'];
Hnatoms=length(Hx);
o=1;
for l=1:Hnatoms
    if strcmp(Hn1(l),'H')
        Hatoms(:,o)=Hxyzdata(:,l);
        o=o+1;
    end
end

```

APPENDIX – MATLAB® PROGRAM FOR THE CALCULATION OF THE PROTON HFI TENSOR

```

else o=o;
end
end

[atm,atmn,atmtyp,mol,m,moln,x,y,z,n1]=textread('Geometry.dat','%s %s %s %s %s
%s %f %f %f %s');
xyzdata=[x';y';z'];
natoms=length(x);
p=1;
for k=1:natoms
    if strcmp(mol(k),'PID')
        PID614(:,p)=xyzdata(:,k);
        nPID614(p)=atmtyp(k);
        p=p+1;
    else p=p;
    end;
end

% Definition of the grid
x=78-30:1:78+30;
y=33-30:1:33+30;
z=20-30:1:20+30;

Axval(1:61,1:61,1:61)=0.; %smallest hyperfine component
Ayval(1:61,1:61,1:61)=0.; %intermediate hyperfine component
Azval(1:61,1:61,1:61)=0.; %largest hyperfine component
Rval(1:61,1:61,1:61)=0.; %rhombicity

% Calculation of the hyperfine tensor for each gridpoint
u0=4*pi*10^(-7);
h=planck;
ge=gfree;
gn=nucgval('2H');
be=bmagn;
bn=nmagn;
const=(u0/(4*pi*h))*(ge*gn*be*bn)*10^24;

[atmtype,cluster1]=textread('SpindensityPBEAA.dat','%s %f');
atmtype=atmtype.';
natoms2=size(atmtype);
natoms=natoms2(2);
totspdens=0;
for i=1:natoms
    totspdens=totspdens+cluster1(i);
end

for nx=1:61
    for ny=1:61
        for nz=1:61
            Point=[x(nx);y(ny);z(nz)];
            r2(1:natoms)=0.;
            Tatom2(1:3,1:3)=0.;
            if strcmp(atmtype,nPID614);
                for i=1:natoms
                    dist=Point-PID614(:,i);
                    r2(i)=sqrt(sum(dist.^2));
                    x2=Point(1)-PID614(1,i);
                    y2=Point(2)-PID614(2,i);
                    z2=Point(3)-PID614(3,i);
                    Adip2=[(r2(i)^2-3*(x2)^2) (-3*x2*y2) (-3*x2*z2);(-3*x2*y2)
                    (r2(i)^2-3*(y2)^2) (-3*y2*z2); (-3*x2*z2) (-3*y2*z2)
                    (r2(i)^2-3*(z2)^2)];
                    Tatom2=Tatom2-
                    const*((cluster1(i)/totspdens)/r2(i)^5)*Adip2;
                end
            end
        end
    end
end

```

```

        Tatom2;
        [Eigvect2,T2]=eig(Tatom2)
        T1=[T2(1,1);T2(2,2);T2(3,3)];
        Tr=sort(T1);
        Rval(ny,nx,nz)=abs(Tr(1)-Tr(2))/Tr(3);
        T=sort(abs(T1));
        Axval(ny,nx,nz)=T(1);
        Ayval(ny,nx,nz)=T(2);
        Azval(ny,nx,nz)=T(3);
    else
        error('The order of atoms in pdb file does not correspond to
that in the spin density file.');
```

end

```

    end;
end;
end;

% Plot of the hyperfine isosurface
figure('numbertitle','off','name','Hyperfine Isosurface');
axis([65 95 10 60 -10 50]) ;
plotmol(PID614,'r',2,2,'label off');
daspect([1 1 1])
axis vis3d
hold on;
p0=patch(isosurface(x,y,z,Ayval,0.5));
set(p0,'facecolor','blue','edgecolor','none');
alpha(0.1)
hold on;
p1=patch(isosurface(x,y,z,Ayval,0.1));
set(p1,'facecolor','blue','edgecolor','none');
alpha(0.1)
hold on;
p2=patch(isosurface(x,y,z,Ayval,0.05));
set(p2,'facecolor','blue','edgecolor','none');
alpha(0.1)
hold on;
p3=patch(isosurface(x,y,z,Ayval,0.01));
set(p3,'facecolor','blue','edgecolor','none');
alpha(0.1)
hold on;
p4=patch(isosurface(x,y,z,Ayval,0.005));
set(p4,'facecolor','blue','edgecolor','none');
alpha(0.1)
hold on;
p4=patch(isosurface(x,y,z,Ayval,0.005));
set(p4,'facecolor','blue','edgecolor','none');
alpha(0.1)
hold on;

% Plot of the hyperfine isosurface on a slice plane
xmin = min(x(:));
ymin = min(y(:));
zmin = min(z(:));
xmax = max(x(:));
ymax = max(y(:));
zmax = max(z(:));

p_av614=[78.3613;32.8638;20.0086];

figure('numbertitle','off','name','Hyperfine Isosurface Slice');
axis([65 85 15 50 0 40]);
plotmol(PID614,'r',2,2,'label off');
daspect([1 1 1])
axis vis3d
hslice = surf(linspace(xmin,xmax,100),linspace(ymin,ymax,100),zeros(100)+20);
rotate(hslice,[0,-1,0],90,p_av614)
rotate(hslice,[0,0,1],6,p_av614)

```

```

rotate(hslice,[1,0.25,0],40,p_av614)
xd = get(hslice,'XData');
yd = get(hslice,'YData');
zd = get(hslice,'ZData');
delete(hslice);
contourslice(x,y,z,Ayval,xd,yd,zd,[0.005 0.01 0.025 0.050 0.075 0.100 0.150
0.200 0.250 0.300 0.350 0.400]);

% Plot of the hyperfine rhombicity
xmin = min(x(:));
ymin = min(y(:));
zmin = min(z(:));
xmax = max(x(:));
ymax = max(y(:));
zmax = max(z(:));

p_av614=[78.3613;32.8638;20.0086];

figure('numbertitle','off','name','Hyperfine Rhombicity');
axis([65 85 15 50 0 40]);
plotmol(PID614,'r',2,2,'label off');
daspect([1 1 1])
axis vis3d
hslice = surf(linspace(xmin,xmax,100),linspace(ymin,ymax,100),zeros(100)+20);
rotate(hslice,[0,-1,0],90,p_av614)
rotate(hslice,[0,0,1],6,p_av614)
rotate(hslice,[1,0.25,0],40,p_av614)
xd = get(hslice,'XData');
yd = get(hslice,'YData');
zd = get(hslice,'ZData');
delete(hslice);
contourslice(x,y,z,Rval,xd,yd,zd,[0.9 0.7 0.5 0.3 0.1]);
colormap('bone')

```


ACKNOWLEDGEMENTS

First and foremost I would like to thank my supervisor, Dr. Marilena Di Valentin, for being the best supervisor a student could wish for: for having proposed a thesis work exactly suited to my interests and allowing me to learn a lot, for her guidance and assistance during all my thesis internship, for giving me the freedom to contribute with my own ideas, for the extremely helpful advice during the process of writing this thesis and for all the time dedicated to the corrections of the drafts of the thesis. I am deeply indebted to her for providing me excellent opportunities for improving my knowledge of EPR spectroscopy and for all her support.

I would also like to thank all the people who helped me in the course of my thesis work. I am especially grateful to Dr. Laura Orian for her invaluable guidance and help in the computational part of the thesis and for performing the ONIOM calculations. Further I would like to thank Dr. Enrico Salvadori for patiently teaching me how to use the EPR spectrometer and for his help and advice during all the experimental part of this work. I am grateful to Prof. Donatella Carbonera for letting me to join the biophysical research group during my internship and for following the progress of the work.